UNIVERSITÀ DI PISA

Dipartimento di Fisica

Corso di Laurea Magistrale in Fisica

TESI DI LAUREA MAGISTRALE IN FISICA

Measurement of the time dependent asymmetry in the decay $B^0 \longrightarrow K^0_S \pi^0 \gamma$ using the Silicon Vertex Detector of the Belle II experiment

---

CANDIDATO

Alberto Martini

RELATORE

Prof. Francesco Forti

Prof. Stefano Bettarini

ANNO ACCADEMICO 2015/2016

Contents

Introduction

My thesis work is in the context of the Belle II experiment, a new generation of B factories that is currently in construction in Tsukuba (Japan) at the KEK laboratory. It is placed on the e^+e^- accelerator machine SuperKEKB, which is planned to achieve the highest instant luminosity ever obtained, $\mathcal{L} = 8 \cdot 10^{35} cm^{-2} s^{-1}$, exploiting the new idea of the nano-beams scheme. Belle II expects to collect data for an integrated luminosity of 50 ab^{-1}, which is around 40 times more than its predecessor Belle. The accelerator machine operates at a center of mass energy of the $\Upsilon(4S)$, right above the production threshold of a $B\overline{B}$ event.
The primary goal of this thesis work is the study of the time dependent asymmetry in the decay $B^0 \longrightarrow K^0_S \pi^0 \gamma$. Since this measurement relies on the new Belle II Silicon Vertex Detector (SVD), a large fraction of my time has also been devoted to issues related to the construction and characterization of this challenging detector. This radiative decay, mediated by the quark transition $b \longrightarrow s\gamma$, is described at the leading order through a loop diagram, since flavour changing neutral currents are forbidden at tree level in the Standard Model, and is therefore potentially sensitive to physics effects not foreseen in the Standard Model.

The main contribution given by my analysis consists in the estimation of the resolution of the decay time difference (Δt) between the B^0 and the $\overline{B}^0$, extracted from the reconstructed vertex positions of the B mesons. Using a simulated data sample of $\Upsilon(4S) \longrightarrow B^0\overline{B}^0$ with $B^0(B^0_{sig}) \longrightarrow K^0_S \pi^0 \gamma$ and $\overline{B}^0(B^0_{tag}) \longrightarrow Generic$, the B^0_{sig} and all its daughters are reconstructed in order to obtain the information of the vertex position. Normally charged tracks are used to obtain the decay vertex position, but in the decay under study the direction extrapolation towards the interaction point of the K^0_S (which is forced to decay into $\pi^+\pi^-$) is the only usable information. For this reason, in the fit procedure an additional beam spot constraint is used, exploiting the very small size of

the beam. The B^0_{tag} vertex, needed to measure the decay time difference, as well as to determine the B flavour at the time of decay, is reconstructed using the information of the tracks belonging to the rest of event, avoiding a complete exclusive reconstruction that would imply a large drop in efficiency. Using the vertex coordinates along the beam axis z, the time difference Δt is obtained through the formula: $\Delta z = \beta \cdot \gamma \cdot c \cdot \Delta t$. The Δt resolution is improved requiring that the kaons are reconstructed by the SVD.

Another important part of my thesis work concerns the participation in the construction of the Belle II SVD, which is crucial to obtain the physics sensitivity. I worked in the INFN-Pisa Laboratory of High Technology on the assembly of the backward and forward double-sided silicon strip detector modules. The quality of the produced modules is essential to ensure the performance of the detector, and a detailed electrical test is performed before shipment. I actively participated in the module characterization work, in particular developing a detailed electrical simulation of the defects to help understand the module behaviour and improve the quality.

In chapter 1, after an introduction to the CP violation mechanism, the physics motivations for the time-dependent CP asymmetry analysis are reported, together with the experimental challenges and previous results.
Chapter 2 presents an overview of the Belle II detector, while in chapter 3 the silicon vertex detector is described in detail, with particular attention to the assembly procedures and the electrical tests. Additional measurements on the electrical behaviour of the sensors are reported at the end of the chapter.
In chapter 4 the SVD sensor simulation is described, including a final comparison with the measurements performed in the previous chapter.
Chapter 5 describes the time-dependent CP asymmetry analysis work which provides an estimation of the statistic uncertainty on the CP asymmetry parameters, obtained using Toy Monte Carlo studies.

Chapter 1

Physics motivation

The Standard Model (SM) is the particle physics theory that describes the fundamental particles and how they interact. The main goal of the Belle II experiment is to perform precision measurements in the flavour sector and to explore the physics beyond the SM using an high luminosity e^+e^- machine and a detector with excellent performances. New Physics (NP) signals can be discovered through, for example, the rare decays of heavy particles or through precision measurements of violations of the charge conjugation and parity (CP) symmetry. This chapter presents the CP violation mechanism and provides the physics motivation for the CP asymmetry study that I performed on the decay $B^0 \longrightarrow K^0_S\pi^0\gamma$.

1.1 CP violation in the Standard Model

The SM explains most of the experimental results and predicts most of the phenomena governed by the electromagnetic, weak and strong interactions. The gravitational interaction is not included in the SM. The SM describes the matter as made of elementary particles with spin $\frac{1}{2}$ (fermions). These particles are gathered into two main categories: leptons and quarks. Both leptons and quarks can be grouped into three generation of fermions, each composed by doublets of particles (fig. 1.1). Overall there are six different types of leptons and six different types of quarks. Each particle has a corresponding anti-particle that can be classified in the same way. Leptons can interact only via the electromagnetic and weak forces and are identified by the lepton number. Quarks are identified by different flavours and can interact also via the strong force. For this reason, quarks have an additional property called color charge, described by the Quantum Chromo Dynamics theory

(QCD). Quarks are combined together to form composite objects called mesons (bounded states composed by a quark and an anti-quark) and barions (bounded states composed by three quarks) in order to create colorless particles obeying the colour-confinement principle. All the ordinary matter is formed by quarks and leptons of the first generation.
In the SM, interactions are mediated by spin-1 particles (gauge bosons). The photon (γ) is the mediator for the electromagnetic interaction, the $W^{\pm}$ and Z^0 bosons are the mediators for the weak interaction, while the gluon (g) mediates the strong one.
The last fundamental particle is the Higgs boson (H), recently discovered [1] [2], that assigns masses to the elementary particles through the mechanism of spontaneous breaking of the gauge symmetry. An overall table of the SM elementary particles is shown in figure 1.1.

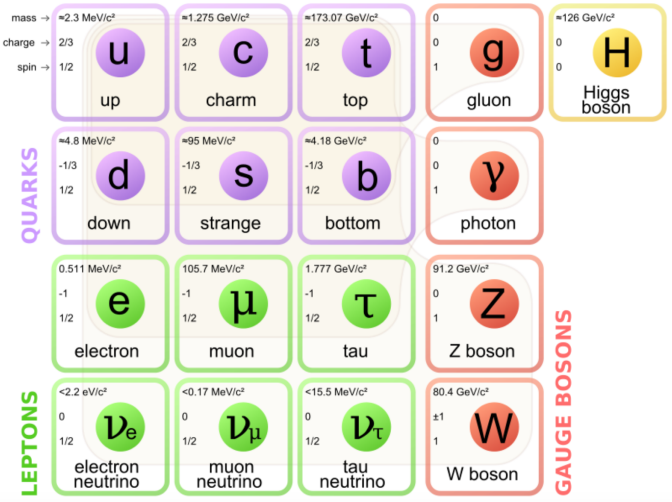

Figure 1.1: Summary table of all elementary particles included in the SM. There are the three generations of quarks and leptons, the gauge bosons that represent the mediators of electromagnetic, weak and strong forces and finally the Higgs boson that provides the masses.

The symmetry structure of the SM is described by the $SU(3)_C \otimes SU(2)_L \otimes U(1)_Y$ group, corresponding to the tensor product between the colour symmetry (QCD contribution), the weak isospin symmetry and the hypercharge symmetry (electromagnetic contribution) respectively. Each fermion has a corresponding anti-fermion, with the same mass but opposite charge and flavor. The transformation between particles and anti-particles is obtained through the CP operator, which is the combination of the charge conjugation (C) and parity (P) operators.
It was expected that nature would be symmetric under the CP transformation, i.e. that

particles and anti-particles would behave exactly in the same way. The discovery of CP symmetry violation dates back to 1964 in the neutral kaons system, and resulted in the Nobel Prize in 1980 for James Cronin and Val Fitch. In the SM, the CP violation occurs due to the presence of a complex phase in the matrix describing the quark mixing in the weak charged currents, the CKM matrix, discussed in the next section.
The third important symmetry to mention is the time symmetry, acting through the time reversal transformation T. All C, P and T symmetries can be violated separately but their simultaneous combination is not, according to the CPT theorem.

1.1.1 The Cabibbo-Kobayashi-Maskawa matrix

Transitions between quarks of different flavours are allowed in the SM and are mediated by the weak interaction. Transitions between quarks belonging to different generations are suppressed with respect to the ones between quarks belonging to the same generation. The charged current transitions of the u, c, t quarks to d, s, b are described by the Cabibbo-Kobayashi-Maskawa (CKM) matrix [3], that consists in a 3 x 3 unitary matrix defined as:

$$\hat{V}_{CKM} = \begin{pmatrix} V_{ud} & V_{us} & V_{ub} \\ V_{cd} & V_{cs} & V_{cb} \\ V_{td} & V_{ts} & V_{tb} \end{pmatrix} \tag{1.1}$$

Each element $V_{q_1 q_2}$ represents the amplitude of the quark transition $q_1 \to q_2$ between an up-type and a down-type quark. The CKM is described by 4 free parameters: 3 mixing angles and an irreducible complex phase which represents the "origin" of the CP violation. The CKM matrix can be parametrised in different ways; the standard parametrization consists in the application of three different rotations:

$$\hat{V}_{CKM} = \begin{pmatrix} c_{12}c_{13} & s_{12}s_{13} & s_{13}e^{-i\delta} \\ -s_{12}c_{23} - c_{12}s_{23}s_{13}e^{i\delta} & c_{12}c_{23} - s_{12}s_{23}s_{13}e^{i\delta} & s_{23}c_{13} \\ s_{12}s_{23} - c_{12}c_{23}s_{13}e^{i\delta} & -c_{12}s_{23} - s_{12}c_{23}s_{13}e^{i\delta} & c_{23}c_{13} \end{pmatrix}$$

where $c_{ij} = \cos\theta_{ij}$ and $s_{ij} = \sin\theta_{ij}$ while θ_{ij} are the three mixing angles and δ is the complex phase. Experimental observations establish that $s_{13} \ll s_{23} \ll s_{12} \ll 1$ where $s_{13} \sim 10^{-3}$. In order to underline this trend, it is useful to use the Wolfenstein parametriza-

tion that defines the parameters A, λ, ρ and η [4]:

$$\hat{V}_{CKM} = \begin{pmatrix} 1-\lambda^2/2 & \lambda & A\lambda^3(\rho - i\eta) \\ -\lambda & 1-\lambda^2/2 & A\lambda^2 \\ A\lambda^3(1-\rho-i\eta) & -A\lambda^2 & 1 \end{pmatrix} + O(\lambda^4)$$

$$\text{with} \quad s_{12} = \lambda = 0.22537 \pm 0.00061 \quad , \quad s_{23} = A\lambda^2 = \lambda\frac{|V_{cb}|}{|V_{us}|} \quad , \quad s_{13}e^{i\delta} = A\lambda^3(\rho + i\eta) = V_{ub}^*$$
$$\text{and} \quad A = 0.814^{+0.023}_{-0.024} \quad , \quad \overline{\rho} = 0.117 \pm 0.021 \quad , \quad \overline{\eta} = 0.353 \pm 0.013. \tag{1.2}$$

Here λ is a small parameter (the sine of the Cabibbo angle [5]), representing the mixing of quarks between different quark generations, while ρ, η contain the complex phase information representing the CP violation term. This parametrisation shows explicitly how the element on the diagonal are close to 1 while the off-diagonal elements are suppressed following the power of λ. The transitions between quarks belonging to the same generation are favoured (Cabibbo favoured) with respect to the others (Cabibbo suppressed or double-Cabibbo suppressed).

1.1.2 Unitarity triangle

From the unitarity condition of the CKM matrix $V_{CKM}V_{CKM}^\dagger = \mathbb{1}$, three off-diagonal relations $\sum_i V_{ij}V_{ik}^* = 0$ with $j \neq k$ can be derived; they are represented in the complex plane (ρ, η) by three triangles with the same area, which indicates the amount of the CP violation. The less degenerate triangle is usually called the unitarity triangle (fig. 1.2) and corresponds to the following equation:

$$V_{ud}V_{ub}^* + V_{cd}V_{cb}^* + V_{td}V_{tb}^* = 0 \tag{1.3}$$

It can be normalised with the term $V_{cb}V_{cb}^*$, becoming:

$$\frac{V_{ud}V_{ub}^*}{V_{cd}V_{cb}^*} + 1 + \frac{V_{td}V_{tb}^*}{V_{cd}V_{cb}^*} = 0 \tag{1.4}$$

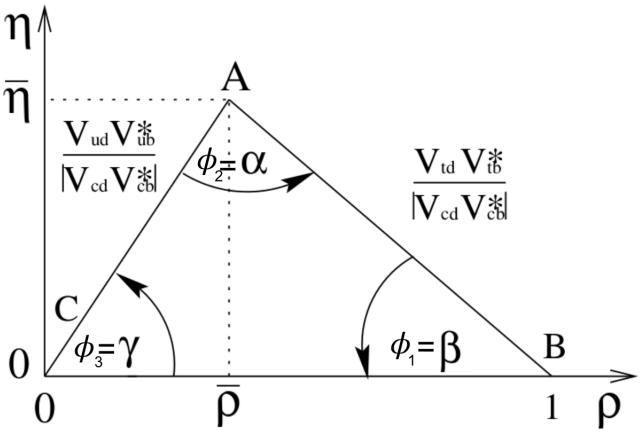

Figure 1.2: Representation of the normalized unitarity triangle in the $(\eta\rho)$ plane. It describes the magnitude of CP violation through its area.

This particular triangle has its three vertices in (0,0), (0,1) and $(\overline{\rho}, \overline{\eta})$ where $\overline{\rho} \simeq \rho(1-\lambda^2/2)$ and $\overline{\eta} \simeq \eta(1-\lambda^2/2)$. This means that if $\eta \neq 0$ the area of the triangle is non-zero, so CP results violated. Moreover the internal angles can be defined as a function of the CKM elements:

$$\phi_1 = arg\left[\frac{V_{tb}^* V_{td}}{V_{cb}^* V_{cd}}\right] \quad , \quad \phi_2 = arg\left[\frac{V_{ub}^* V_{ud}}{V_{tb}^* V_{tb}}\right] \quad , \quad \phi_3 = arg\left[\frac{V_{cb}^* V_{cd}}{V_{ub}^* V_{ud}}\right] \tag{1.5}$$

The experimental constraints on the $\overline{\rho}$ and $\overline{\eta}$ parameters are shown in figure 1.7.

1.1.3 Limitations of the Standard Model

Even thought the SM is extremely successful in explaining the large majority of experimental results, some issues still remain unsolved. Here, some of the most important limitations of the SM are reported, in order to underline the fact that there are still lots of physics phenomena to understand:

- the flavour and the generation structure of quarks and leptons, together with their symmetry structure, are not explained by the SM, but rather used as an assumption;
- mass hierarchy problem: the quark masses, are not predicted theoretically. The SM does not explain why the quark masses have these values nor why there is a mass hierarchy among the three generations;
- dark matter and dark energy: cosmological observations have determined that the

universe is composed by ∼75% of unknown dark energy, ∼20% by dark matter (Dark Matter) and the remaining 5% by baryonic matter. The SM can account only for the baryonic contribution without explaining the other 95%;

- matter-antimatter asymmetry: in the observable universe a large baryonic asymmetry matter-antimatter is present. The CP violation concept allows this kind of asymmetry but the size of the CP violation predicted by the SM is not sufficient to explain this unbalance [6].

1.2 Mixing and CP violation in neutral B meson systems

In this section the mixing within B meson systems is described, in order to understand how the CP violation process can occur, along with the main experimental results. More details can be found in [7].

1.2.1 Neutral B meson oscillations

The oscillation process occurs between a pair of neutral mesons, one the anti-particle of the other, and therefore with opposite flavour quantum numbers. During time evolution, one of these particles becomes the other and vice-versa because the mass eigenstates differ from the flavour eigenstates. This phenomenon is known as mixing and occurs in four different neutral meson system: $K^0 - \overline{K}^0$, $D^0 - \overline{D}^0$, $B_d^0 - \overline{B}_{d^0}$ and $B_s^0 - \overline{B}_{s^0}$. Mixing occurs, in the SM, through the weak interaction and it is described, for example for the B meson system, by box diagrams involving two W bosons and two up-type quarks (fig. 1.3).

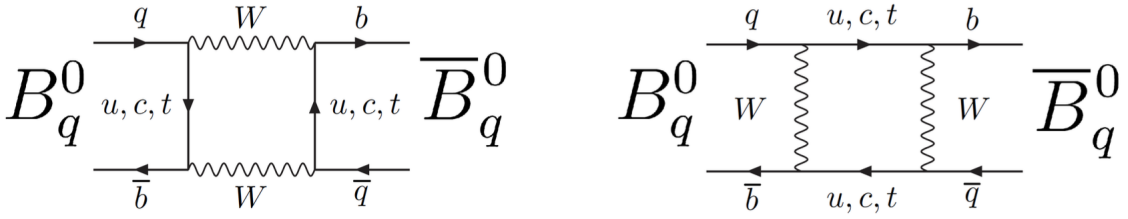

Figure 1.3: Box diagrams representing the B mesons mixing process.

Considering a generic system formed by a neutral meson and its anti-meson, a state can be described by a linear combination of the flavour eigenstates $|M^0\rangle$ and $|\overline{M}^0\rangle$, which in

general differ from the mass eigenstates $|M_L^0\rangle$ and $|M_H^0\rangle$:

$$|\psi(t=0)\rangle = a_0|M^0\rangle + b_0|\overline{M}^0\rangle \tag{1.6}$$

Introducing the time dependence, one can describe the mixing phenomenon and the decay of the mesons with

$$|\psi(t\neq 0)\rangle = a(t)|M^0\rangle + b(t)|\overline{M}^0\rangle + \sum_j c_j(t)|f_j\rangle \ , \tag{1.7}$$

where c_j is the transition amplitude to the corresponding final state $|f_j\rangle$. The time evolution can be obtained from the time-dependent Schrödinger equation:

$$i\frac{\partial\psi}{\partial t} = H_{\text{eff}}\psi \tag{1.8}$$

where H_{eff} is the effective Hamiltonian of the system that can be parametrised as:

$$H_{\text{eff}} = M - \frac{i}{2}\Gamma = \begin{pmatrix} M_{11} & M_{12} \\ M_{21} & M_{22} \end{pmatrix} - \frac{i}{2}\begin{pmatrix} \Gamma_{11} & \Gamma_{12} \\ \Gamma_{21} & \Gamma_{22} \end{pmatrix} \tag{1.9}$$

where M is the Hermitian matrix that provides the mass term while the Γ matrix represents the decay term. Assuming the CPT theorem as valid, the following relations hold:

$$M_{11} = M_{22} \quad , \quad M_{21} = M_{12}^* \quad , \quad \Gamma_{11} = \Gamma_{22} \quad , \quad \Gamma_{21} = \Gamma_{12}^* \tag{1.10}$$

meaning that the mass and the total decay width of particles and antiparticles are identical. The diagonalization of the H_{eff} matrix allows us to find the relations for the mass difference and decay width difference between the two meson states:

$$\begin{aligned} \Delta m &\equiv m_H - m_L = Re(\lambda_H - \lambda_L) \ , \\ \Delta\Gamma &\equiv \Gamma_H - \Gamma_L = -2\,\text{Im}(\lambda_H - \lambda_L) \end{aligned} \tag{1.11}$$

where λ_H and λ_L are the eigenvalues of H_{eff}.

One can also define the mass eigenstates using the q and p parameters and consequently

$|M^0\rangle$ and $|\overline{M}^0\rangle$:

$$\begin{array}{ll} |M_L\rangle = p|M^0\rangle + q|\overline{M}^0\rangle & \\ |M_H\rangle = p|M^0\rangle - q|\overline{M}^0\rangle & \end{array} \rightarrow \begin{array}{l} |M^0\rangle = 1/2p[|M_H\rangle + |M_L\rangle] \\ |\overline{M}^0\rangle = -1/2q[|M_H\rangle - |M_L\rangle] \end{array} \tag{1.12}$$

with the normalization condition $|p^2| + |q^2| = 1$.
These considerations allow us to write the relations:

$$\begin{aligned} m_H - m_L &= \frac{q}{p}(M_{12} - \frac{i}{2}\Gamma_{12}) \quad , \\ \frac{q}{p} &= \sqrt{\frac{M_{12}^* - \frac{i}{2}\Gamma_{12}^*}{M_{12} - \frac{i}{2}\Gamma_{12}}} \, . \end{aligned} \tag{1.13}$$

The time evolution of the mass eigenstates can be written using the usual time-dependent wave function form of the Schrödinger equation (with a diagonal Hamiltonian):

$$\begin{aligned} |M_H(t)\rangle &= e^{-i\lambda_H t}|M_H(0)\rangle \, , \\ |M_L(t)\rangle &= e^{-i\lambda_L t}|M_L(0)\rangle \end{aligned} \tag{1.14}$$

and, combining equations 1.12 and 1.14, one can determine the time evolution of a state generated originally as $|M^0\rangle$ or $|\overline{M}^0\rangle$

$$\begin{aligned} |M^0(t)\rangle &= g_+(t)|M^0\rangle + \frac{q}{p}g_-(t)|\overline{M}^0\rangle \\ |\overline{M}^0(t)\rangle &= g_-(t)\frac{p}{q}|M^0\rangle + g_+(t)|\overline{M}^0\rangle \end{aligned} \tag{1.15}$$

where $g_\pm$ includes the temporal dependence as shown below:

$$g_\pm(t) = \frac{1}{2}(e^{-i\lambda_H t} \pm e^{-i\lambda_L t}) \tag{1.16}$$

A pure sample of M^0 ($\overline{M}^0$) mesons at t=0 will oscillate to the opposite flavour, with a probability of having $\overline{M}^0$ (M^0) at the time t given by:

$$\begin{aligned} P(M^0 \rightarrow \overline{M}^0) &\propto |\langle M^0|\overline{M}^0(t)\rangle|^2 = \left|\frac{p}{q}\right|^2 |g_-(t)|^2 \\ P(\overline{M}^0 \rightarrow M^0) &\propto |\langle \overline{M}^0|M^0(t)\rangle|^2 = \left|\frac{q}{p}\right|^2 |g_-(t)|^2 \end{aligned} \tag{1.17}$$

where the time dependent term can be written as:

$$|g_{\pm}(t)|^2 = \frac{e^{-\Gamma t}}{4}(1 + e^{\Delta\Gamma t} \pm 2e^{\frac{\Delta\Gamma t}{2}} \cos \Delta m t) \tag{1.18}$$

with $\Gamma = \frac{\Gamma_L + \Gamma_H}{2}$ and $\Delta\Gamma = \Gamma_H - \Gamma_L$.

The oscillation probability has different values for the different neutral meson system. Based on measured parameters, this probability is shown in figure 1.4 for all the four meson systems, as a function of the product Γt (representing the number of life times elapsed). Both the $K^0 - \overline{K}^0$ and the $B^0 - \overline{B}^0$ systems exhibit relatively large oscillations with a period comparable to the lifetime. In the B_s system the oscillation is very rapid, while in the D system it remains very small. This is due to the fact that mixing in the neutral D system proceeds via second order box diagrams (see fig. 1.3) where down-type quarks are exchanged, resulting in both CKM and GIM [8] suppressions.

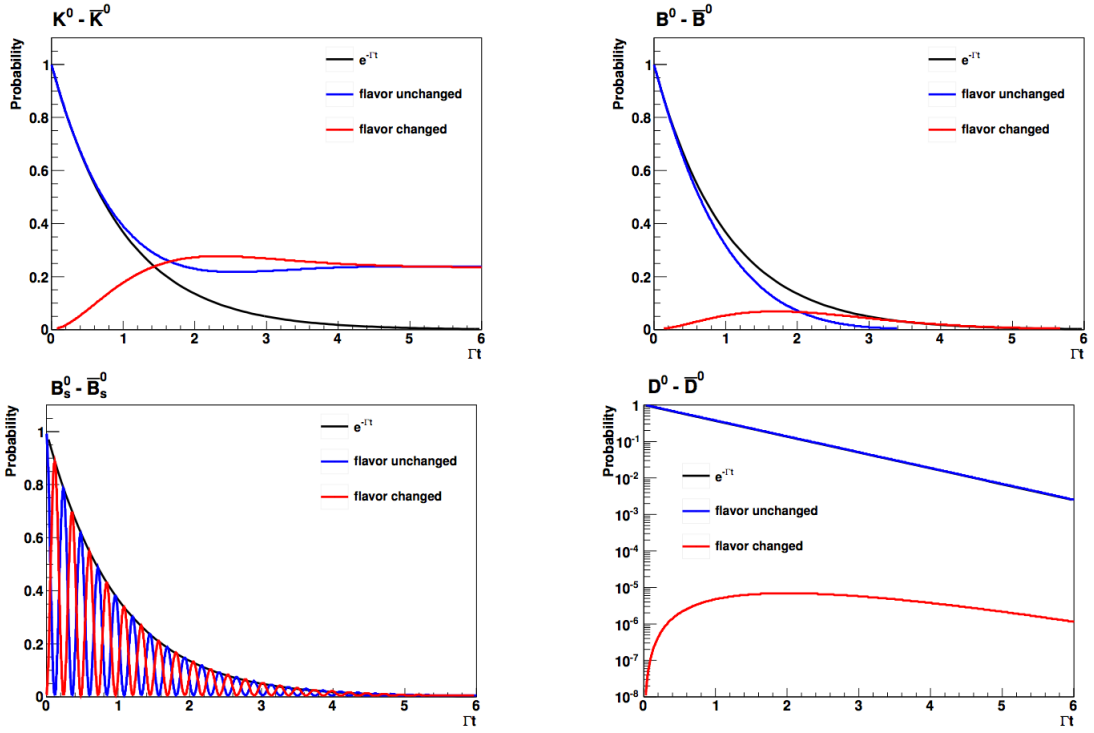

Figure 1.4: Probability to change (red lines) and not change (blue lines) flavour with respect to Γt for the K-system (top left), B_d-system (top right), B_s-system (bottom left) and D-system (bottom right). The exponential decay function $e^{-\Gamma t}$ is also reported for each meson system.

1.2.2 CP violation modes

In order to discuss the CP violation processes it is useful to define the decay amplitude of the involved mesons M^0 (A) and $\overline{M}^0$ ($\overline{A}$) into the final states f and $\overline{f}$:

$$\begin{aligned} A_f = \langle f|H|M\rangle \ , \ \overline{A}_f = \langle f|H|\overline{M}\rangle \ , \\ A_{\overline{f}} = \langle \overline{f}|H|M\rangle \ , \ \overline{A}_{\overline{f}} = \langle \overline{f}|H|\overline{M}\rangle \end{aligned} \tag{1.19}$$

The decay amplitude is related to the decay width (Γ) through

$$\Gamma(M \to f) = |A_f|^2 \phi_f \tag{1.20}$$

where ϕ_f takes into account the phase space of the decay $M \to f$.
CP violation can occurs in three different ways:

- Direct violation: it occurs when the decay rate of the M meson to a certain state f is different from that of $\overline{M}$ to the corresponding CP-conjugate state, meaning that $\Gamma(M \to f) \neq \Gamma(\overline{M} \to \overline{f})$. The observable used to detect this asymmetry is:

$$\mathcal{A}_f = \frac{\Gamma(M \to f) - \Gamma(\overline{M} \to \overline{f})}{\Gamma(M \to f) + \Gamma(\overline{M} \to \overline{f})} = \frac{1 - |A_f/\overline{A}_{\overline{f}}|^2}{1 + |A_f/\overline{A}_{\overline{f}}|^2} \tag{1.21}$$

  and CP is violated if the condition $|A_f/\overline{A}_{\overline{f}}| \neq 1$ holds. This kind of violation can occur also with charged mesons because it is not connected to the mixing phenomenon.

- Violation in the mixing: it occurs when the mixing probability is different between a neutral meson and its anti-particle, that is:

$$P(M^0 \to \overline{M}^0) \neq P(\overline{M}^0 \to M^0), \tag{1.22}$$

  which, according to eq. 1.17, requires $|q/p| \neq 1$. The observable used to measure this asymmetry is:

$$\mathcal{A}_{CP} = \frac{d\Gamma(M^0(t) \to \overline{f})/dt - d\Gamma(\overline{M}^0(t) \to f)/dt}{d\Gamma(M^0(t) \to \overline{f})/dt + d\Gamma(\overline{M}^0(t) \to f)/dt} = \frac{1 - |q/p|^4}{1 + |q/p|^4} \tag{1.23}$$

  The best experimental method used for this measurement is to select a final state that uniquely identifies the flavor of the meson at the time of decay. As an example, in a semi-leptonic decay like $B^0 \longrightarrow l^+\nu X^-$ ($\overline{B}^0 \longrightarrow l^-\overline{\nu}X^+$), the charge of the

lepton contains the information of the flavour of the decaying particle.

- Violation in the interference between mixing and decay (also known as the mixing-induced CP violation): it occurs when both M^0 and $\overline{M}^0$ can decay into the same CP eigenstate f_{CP}. In this case M^0 can decay to f_{CP} in two ways: the direct decay $M^0 \to f_{CP}$ and the oscillation $M^0 \to \overline{M}^0$ followed by the decay $\overline{M}^0 \to f_{CP}$. The interference between these two decay modes can exhibit the mixing induced CP violation (fig. 1.5).

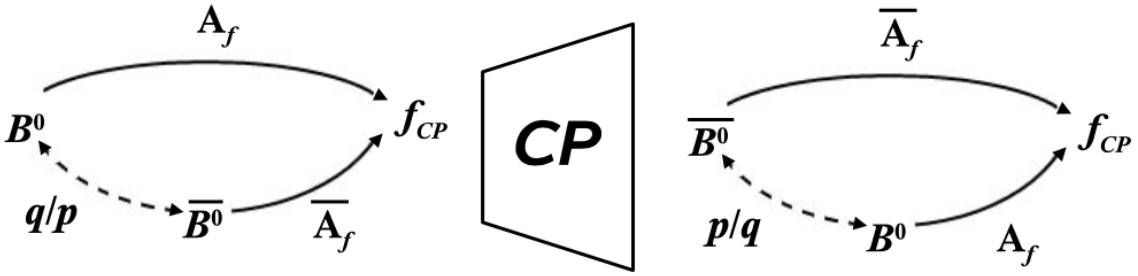

Figure 1.5: Effect of the CP symmetry on B^0 decay to a CP eigenstate f_{CP}. The CP asymmetry is due to the interference between mixing, described by parameters p and q, and the decay amplitudes A_f and $\overline{A}_f$.

In this case, the observable used to detect the time-dependent asymmetry is:

$$\mathcal{A}_{f_{CP}} = \frac{d\Gamma(\overline{M}^0(t) \to f_{CP})/dt - d\Gamma(M^0(t) \to f_{CP})/dt}{d\Gamma(\overline{M}^0(t) \to f_{CP})/dt + d\Gamma(M^0(t) \to f_{CP})/dt} \tag{1.24}$$

and defining λ_f as follows:

$$\lambda_f = \frac{q}{p}\frac{\overline{A}_f}{A_f} \ , \tag{1.25}$$

it is possible to re-write the observable $A_{f_{CP}}$,

$$\mathcal{A}_{f_{CP}} = \frac{(1 - |\lambda_f|^2)\cos(\Delta m t) - 2\,\mathrm{Im}(\lambda_f)\sin(\Delta m t)}{1 + |\lambda_f|^2} \ . \tag{1.26}$$

This asymmetry can be different from zero even if neither direct CP violation ($|A_f/\overline{A}_{\overline{f}}| = 1$) nor CP violation in the mixing ($|q/p| = 1$) are present, provided the following conditions hold:

$$\Delta m \neq 0 \ , \ \mathrm{Im}(\lambda_f) \neq 0 \tag{1.27}$$

The type of CP asymmetry studied in this thesis falls in the third category with some peculiarity and it will be explained in section 1.3.

1.2.3 Experimental results

The CP violation was discovered, in the mixing of the neutral kaon system in 1964 [9]. The direct CP violation [10] was found to be non-zero in 1999 by the KTeV experiment at Fermilab and the NA48 experiment at CERN [11]. The construction of B factories leads to the measurement of both indirect and direct CP violations in the B meson sector; a complete and detailed view of the results obtained so far can be found in [12]. The direct CP violation has been searched in flavour specific decays that occur with two different mechanisms ("penguin" and "tree"), which carry different weak and strong phases. The violation is observable as a rate asymmetry between a decay and its CP conjugate; for example, in the decay $B^0 \longrightarrow K^+\pi^-$, where the charge of the kaon identifies the flavor of the decaying B meson, $\mathcal{A} = (n_{K^-\pi^+} - n_{K^+\pi^-})/(n_{K^-\pi^+} + n_{K^+\pi^-})$. The most precise asymmetry measurement for that decay arises from the BaBar experiment [13] with $\mathcal{A} = -0.133 \pm 0.030(stat) \pm 0.009(syst)$ which correspond to 4.2 standard deviation.
The first measurements of the indirect CP violation concern the observation of ϕ_1 (see fig. 1.2) in the channel $B^0 \longrightarrow J/\Psi\ K^0_S$. The final state is a CP eigenstate, thus it can be reached from both B^0 and $\overline{B}^0$ meaning that a mixing induced time-dependent CP violation can occur. The detection of the final state is very clean because the J/Ψ decays into lepton pairs and the K^0_S into pairs of oppositely charged pions; moreover this decay is also theoretically very clean for ϕ_1 determination (the deviation due to the contribution of loop diagrams is $\sim 1\%$). The decay into $J/\Psi\ K^0_S$ is just one of the possible decays due to a $b \to c\bar{c}s$ transition. The measurement results of ϕ_1 [14] coming from these transitions are summarized in figure 1.6 (left), together with the results coming from charmless decays (right). The world average value for this parameter is $\phi_1 = (21.9 \pm 0.7)^\circ$ [14]. The 4-fold ambiguity of the determination of ϕ_1 from the $\sin 2\phi_1$ measurements is resolved by using the full set of constraints on the unitarity triangle, as shown in figure 1.7.
In the search for indirect CP violation, the decays deriving from $b \to du\overline{u}$ transitions are

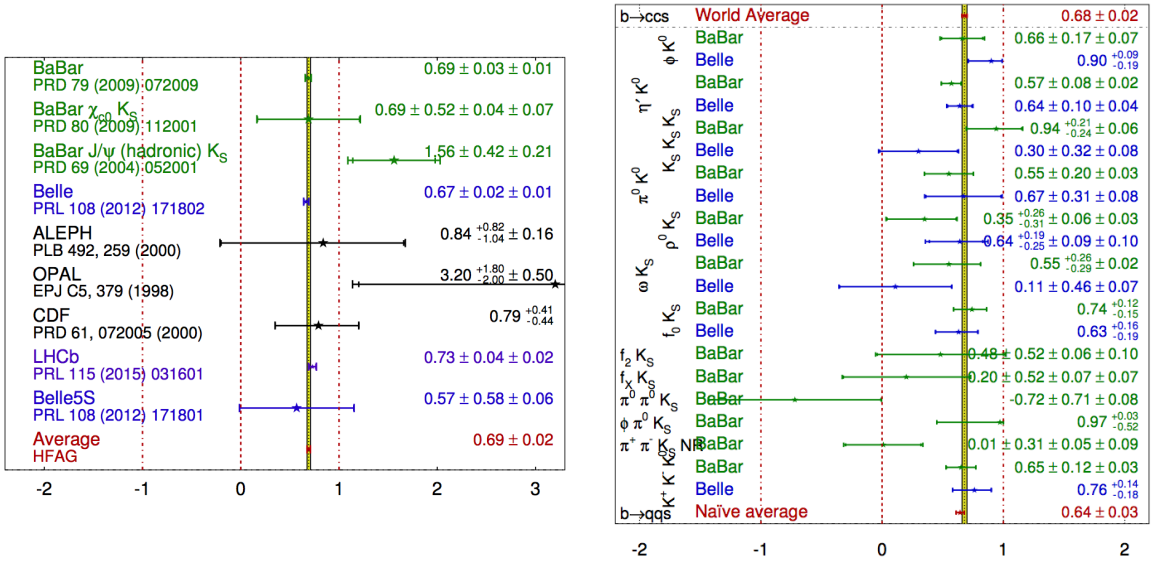

Figure 1.6: Left: summary table of $\sin 2\phi_1$ measurements in B^0 decays to charmonium and K^0 final states. Right: summary table of $\sin 2\phi_1$ measurements in charmless B^0 decays. Here the world average for $b \to ccs$ takes into account only Belle and BaBar results.

useful as they provide measurements of ϕ_2, through the interference between mixing and decay. The most promising channels are $B \longrightarrow \pi\pi$ and $B \longrightarrow \rho\rho$. Unfortunately, in these decays the theoretical uncertainties are large because of the sizable contribution of loop diagrams. This requires a complicated theoretical approach (more details can be found in [15]). The weighted average for ϕ_2 from the combination of $B \longrightarrow \pi\pi$, $\rho\rho$, $\pi^+\pi^-\pi^0$ decays provides us the value $\phi_2 = (87.6^{+3.5}_{-3.3})^\circ$ [14], which is consistent with the standard model expectations.

The world average of ϕ_3 is $(73.2^{+6.3}_{-7.0})^\circ$ [14], that is still limited by the small branching fractions of the processes used to measure this angle.

Although these measurements are consistent with the SM predictions, including the measurements of the sides of the unitarity triangle, which come mainly from branching fractions, improved precision in the measurements of the angles in the unitarity triangle could lead to NP signals, and is therefore one essential part of the Belle II physics program.

1.3 Time-Dependent CP asymmetry in $B^0 \longrightarrow K^0_S\pi^0\gamma$

The mixing induced time-dependent CP asymmetry can occur also in the decay $B^0 \longrightarrow K^0_S\pi^0\gamma$ which proceeds at first order through loop diagrams called “penguin” diagrams.

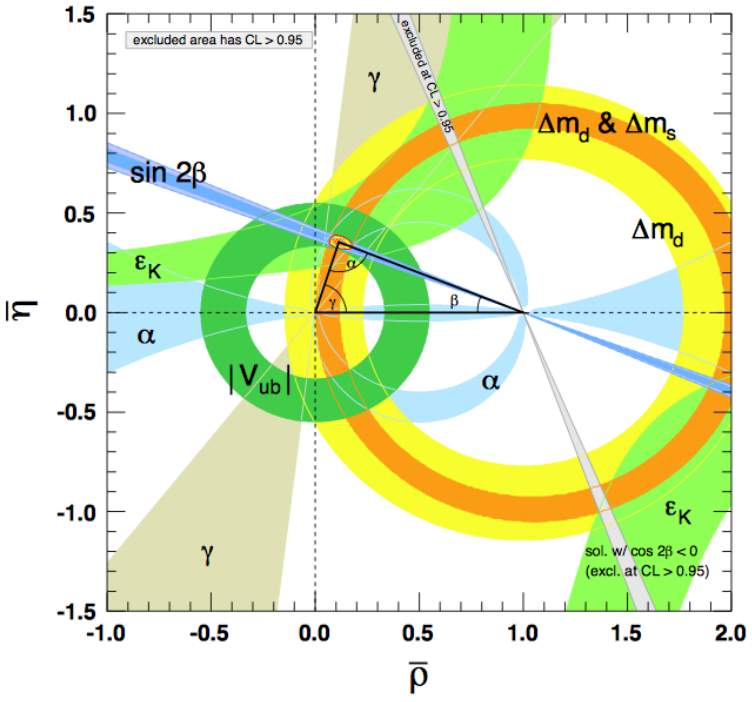

Figure 1.7: The $\overline{\rho}-\overline{\eta}$ plane showing the various experimental constraints on the unitarity triangle and CKM parameters. More details can be found in [16].

This final state is not a CP eigenstate, because in the SM the photon helicity is fixed to be right-handed for B decays or left-handed for $\overline{B}$ decays as shown in figure 1.8.

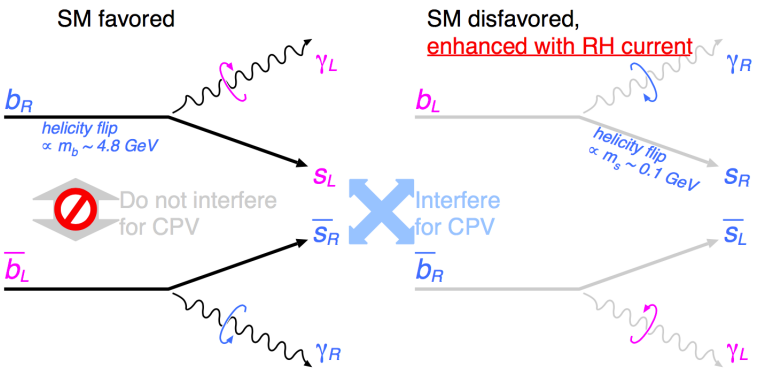

Figure 1.8: Photon helicity in the decay $b \to s\gamma$ for standard model favoured transition (left) and disfavoured (right).

However, new physics can change the helicity structure of the loop diagrams leading to interference effects.

The time-dependent formalism, together with the theoretical motivations of my analysis are described in more detail in this section. Finally, current measurement results and experimental challenges of the decay under study are pointed out.

1.3.1 Time-Dependent asymmetry

This section introduces the formalism needed to measure the time-dependent CP asymmetry. B factories, as SuperKEKB for the Belle II experiment, are able to produce $B^0\overline{B}^0$ pairs from the decay of the Υ(4S) ($e^+e^- \longrightarrow \Upsilon(4S) \longrightarrow B^0\overline{B}^0$). These pairs are produced in an entangled initial state, and therefore, when a B^0 meson decays into a final state which allows to identify its flavour, the flavour of the other B^0 is automatically fixed.
Let's consider the decay chain $\Upsilon(4S) \longrightarrow B^0\overline{B}^0 \longrightarrow f_{CP}f_{tag}$, where one of the B^0 mesons decays at the time t_{CP} to a CP eigenstate f_{CP} and the other decays at the time t_{tag} to a final state f_{tag} that allows flavour tagging. Using the time evolution mechanism discussed in section 1.2.1, it can be shown that the decay rate of each meson has a time dependence given by:

$$P_{\pm}(\Delta t) = \frac{e^{-|\Delta t|/\tau_{B^0}}}{4\tau_{B^0}}\Big\{1 \pm S\sin(\Delta m \Delta t) \mp C\cos(\Delta m \Delta t)\Big\} \tag{1.28}$$

where C and S are the CP-violation parameters, τ_{B^0} is the neutral meson life time, Δm is the mass difference between the two B^0 and $\Delta t = t_{CP} - t_{tag}$ is the decay time difference between the neutral B mesons ([7] pages 122-123). The + sign occurs when the tagging B meson is a B^0 while the - sign occurs when the tagging B meson is a $\overline{B}^0$. The parameters C and S represent respectively the direct and the mixing induced CP violation strength. These two parameters provide different experimental effects as shown in figure 1.9; it is possible to distinguish three combined effects:

- Presence of mixing induced CP violation ($S \neq 0$) and no direct CP violation contribution (C=0): the Δt distributions for B^0 and $\overline{B}^0$ are shifted in time while the resulting time-dependent CP asymmetry follows a sine shape;

- Vanishing contribution of mixing induced CP violation (S=0) and presence of direct CP violation contribution ($C \neq 0$): the Δt distribution shows a difference in the number of decays of B^0 and $\overline{B}^0$ while the resulting time-dependent CP asymmetry follows a cosine shape;

- Presence of both mixing induced CP violation ($S \neq 0$) and direct CP violation contribution ($C \neq 0$): the Δt distribution shows a shift in time and in the number of decays of B^0 and $\overline{B}^0$ while the resulting time-dependent CP asymmetry follows a superposition of sine and cosine shape.

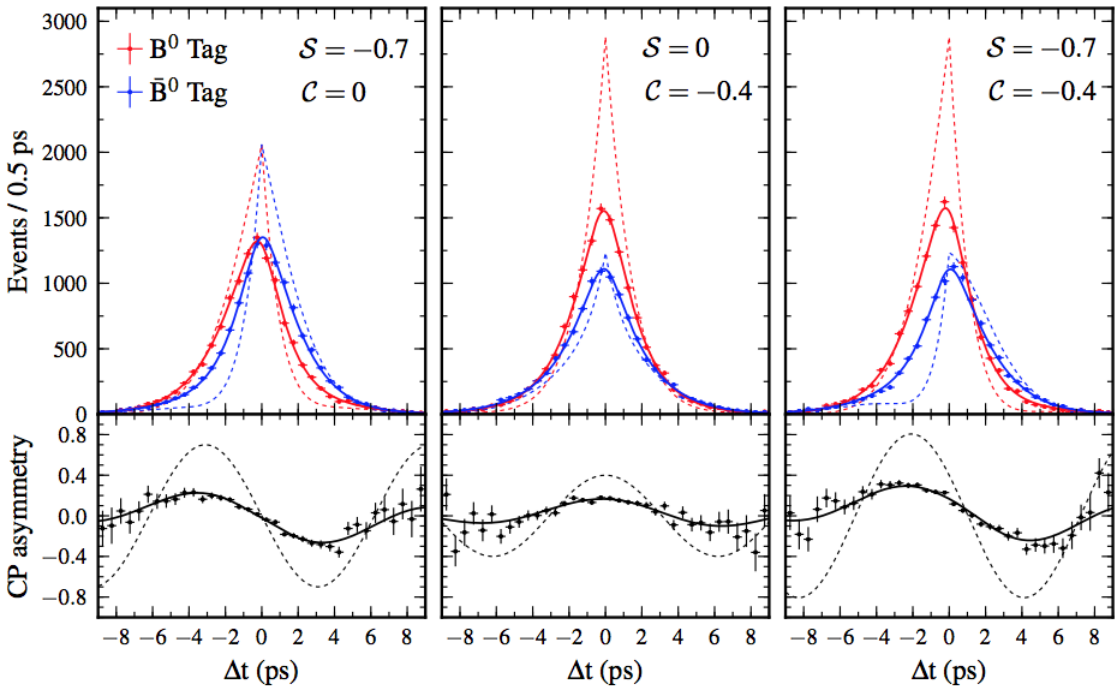

Figure 1.9: Distributions of proper decay time difference for B^0_{tag} (red lines) and $\overline{B}^0_{tag}$ (blue lines) mesons and corresponding CP asymmetries for three scenarios of mixing-induced and direct CP violation. Theoretical (dashed lines) and experimental (solid lines) estimations are shown. These results [17] come from a Monte Carlo sample generated by the Belle experiment.

1.3.2 Theoretical motivation and New Physics sensitivity

The decay mode under study has great potential for a time-dependent CP asymmetry search because its Branching Fraction (BF) is relatively large for a loop-mediated decay (BF$\simeq 3.8 \cdot 10^{-5}$) and because it is sensitive to the helicity structure of NP. It consists in a radiative decay based on the quark transition $b \longrightarrow s\gamma$ that is described at the leading order through a loop diagram (fig. 1.10).

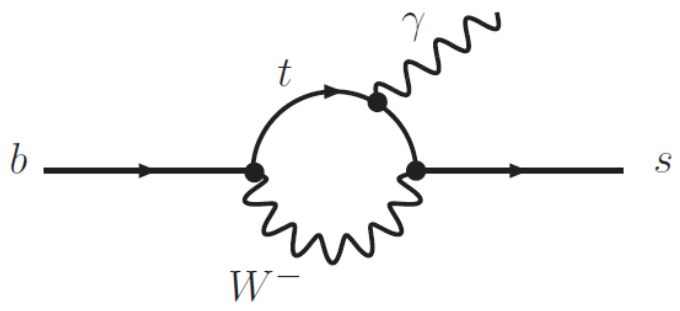

Figure 1.10: Loop diagram of the transition $b \to s\gamma$.

These diagrams are important because they describe flavour changing interactions which are suppressed at tree level in the SM. The measurement of the inclusive branching fraction is in agreement with the SM prediction at the level of 1σ, implying strong constraints on several NP models (more details in Ref. [18], [19]):

$$BF^{meas}(B \to X_s\gamma) = (3.43 \pm 0.21 \pm 0.07)\cdot 10^{-4} \quad , \quad BF^{SM}(B \to X_s\gamma) = (3.15 \pm 0.23)\cdot 10^{-4} \tag{1.29}$$

where the measured value, on the left, comes from the average of Belle and BaBar measurements while on the right the SM prediction is reported [7].

Within the SM, due to the left-handed coupling of the weak interactions, in the transitions $b \to s\gamma$ the photon emitted by a b ($\bar{b}$) quark is predominantly left-handed (right-handed). As a consequence, in the exclusive decay $B^0 \longrightarrow K^0_S\pi^0\gamma$, the interference between the direct decay and the decay after $B^0 - \overline{B}^0$ mixing is suppressed; thus, the parameter S, introduced in the equation 1.28, is strongly suppressed as it represents the mixed induced asymmetry. For this reason, one way to detect a NP signal is to reveal a time-dependent CP asymmetry and, although the final state is not a CP eigenstate, the theoretical formalism used in section 1.3.1 is still valid.

The naive estimate for the S parameter in the SM is $S^{SM}_{K^0_S\pi^0\gamma} \sim -2(m_s/m_b)\sin 2\phi_1 \sim 2\%$, where ϕ_1 is one of the unitarity triangle angles introduced in 1.5, while the term m_s/m_b is the ratio between the s and b quark masses. There are additional contributions to this predicted value coming from strong interaction processes, like $b \longrightarrow s\gamma g$, which are of the order of Λ/m_b. These contributions are difficult to compute in a reliable way but can be predicted through simple power counting estimates, by using a combination of Soft Collinear Effective Theory (SCET) [20] and heavy-Hadron Chiral Perturbative Theory [21]. The SCET theory can be applied only for soft and collinear K^0_S and π^0 and from the experimental point of view, this condition results in a requirement on the invariant mass of the $K^0_S\pi^0$ system. This is the reason why the Belle and the BaBar analysis required $M_{K\pi}$ <1.8 GeV/c^2. After these considerations, the value of $S_{K^0_S\pi^0\gamma}$ is allowed to became as large as $\sim 8\%$ (more details can be found in [22]). Therefore, the final inclusive SM prediction for S reaches the value $\sim$0.1: any significant deviation beyond this value is a striking evidence of NP.

1.3.3 Current measurements

The current world average for S, estimated by the BaBar and Belle experiments, is: $S_{K^0_S\pi^0\gamma} = -0.16 \pm 0.22$ including the contribution of the resonant measurement $B^0 \longrightarrow K^*(\longrightarrow K^0_S\pi^0)\gamma$. It has been recently verified that averaging the results of the resonant and direct measurements is a justified procedure (see [22]). Anyway, this result is still dominated by the statistical uncertainty. The Belle II experiment is expected to reduce the statistical uncertainty to better than 0.03 providing enough sensitivity to measure the expected SM value of 0.1 or, hopefully, NP deviations from it.
Other similar decay channels have been studied by the BaBar and Belle collaborations. They measured the S and C parameters of the decays reported in table 1.1, without finding any deviation from the SM predictions.

	BABAR	Belle	Average
$\mathcal{S}(K^{*0}\gamma)$	$-0.03 \pm 0.29 \pm 0.03$	$-0.32 \pm 0.35 \pm 0.05$	-0.17 ± 0.20
$\mathcal{C}(K^{*0}\gamma)$	$-0.14 \pm 0.16 \pm 0.03$	$0.20 \pm 0.24 \pm 0.05$	0.00 ± 0.13
$\mathcal{S}(K^0_S\pi^0\gamma)$	$-0.78 \pm 0.59 \pm 0.09$	$-0.10 \pm 0.31 \pm 0.07$	-0.40 ± 0.25
$\mathcal{C}(K^0_S\pi^0\gamma)$	$-0.36 \pm 0.33 \pm 0.04$	$0.20 \pm 0.20 \pm 0.06$	0.00 ± 0.16
$\mathcal{S}(K^0_S\eta\gamma)$	$-0.18 \pm 0.48 \pm 0.12$		-0.18 ± 0.50
$\mathcal{C}(K^0_S\eta\gamma)$	$-0.32 \pm 0.40 \pm 0.07$		-0.32 ± 0.41
$\mathcal{S}(K^0_S\phi\gamma)$		$0.74 \pm 0.90 \pm 0.20$	0.74 ± 0.91
$\mathcal{C}(K^0_S\phi\gamma)$		$-0.35 \pm 0.58 \pm 0.20$	-0.35 ± 0.61
$\mathcal{S}(K^0_S\rho^0\gamma)$		$0.11 \pm 0.33 \pm 0.07$	0.11 ± 0.35
$\mathcal{C}(K^0_S\pi^+\pi^-\gamma)^\dagger$		$0.05 \pm 0.18 \pm 0.06$	0.05 ± 0.20
$\mathcal{S}(\rho^0\gamma)$		$-0.83 \pm 0.65 \pm 0.18$	-0.83 ± 0.68
$\mathcal{C}(\rho^0\gamma)$		$0.44 \pm 0.49 \pm 0.14$	0.44 ± 0.53

Table 1.1: Summary of time-dependent measurements of CP asymmetries in $b \longrightarrow s\gamma$ decays [7].

Nonetheless a light tension between the BaBar and Belle results is present, as can bee seen in figure 1.11, and will need to be elucidated with increased statistics.

1.3.4 Experimental challenges

The decay channel $B^0 \longrightarrow K^0_S\pi^0\gamma$ is quite difficult to reconstruct due to the presence of three neutral particles in the final state. For this reason, this decay can be studied with good results only in a clean environment such as at a B-factory, where the background contributions are much less than in an hadronic collider. For example, the LHCb experiment, operating on forward p-p collisions, provides excellent results for decay channels

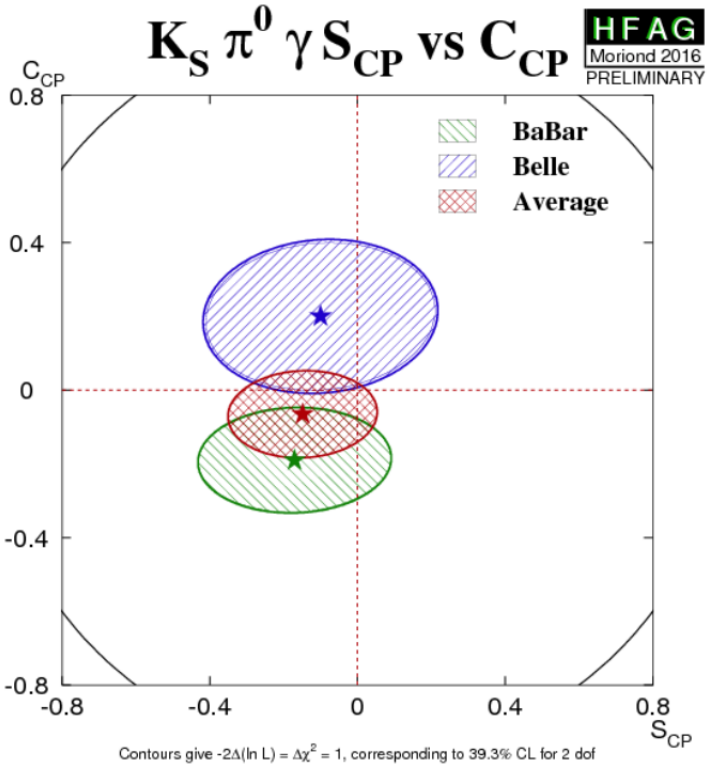

Figure 1.11: BaBar and Belle average result of C vs S for the decay $B^0 \to K^0_S\pi^0\gamma$; separated results are shown as well.

with charged leptons [23], where their trigger capabilities can be exploited, but is much less efficient for these neutral-only decay modes.

In the decay under study, only the K^0_S decays into charged particles, leading to difficulties in the reconstruction of the vertex of the B^0. In fact, in order to reconstruct the B meson vertex, one would need at least two charged particles coming from the same vertex. In the decay $B^0 \longrightarrow K^0_S\pi^0\gamma$, the kaons reconstructed through the decay $K^0_S \longrightarrow \pi^+\pi^-$ are extrapolated back to the interaction point and are used with an additional beam spot constraint in order to extrapolate the vertex position of the B^0 mesons. That constraint consists in an ellipse placed around the boost direction with very thin transversal dimensions. Thanks to the new nano-beam scheme (see section 2.1.1) of the Belle II experiment, this ellipse is able to provide a very tight constraint. With the high integrated luminosity of 50 ab^{-1} (corresponding to the maximum integrated luminosity expected), the expected number of reconstructed events, is in the order of $\sim 10^4$.

Chapter 2

Belle II experiment

The Belle II experiment is placed on the e^+e^- collider SuperKEKB in Tsukuba (Japan) at the KEK laboratory, which represents the new generation of B factories. Belle II and SuperKEKB are upgrades of Belle experiment and KEKB accelerator, which operated from 1999 to 2010. While the goal of the first generation B-factories (Belle at KEKB, KEK and Babar at PEP-II, SLAC) was the discovery of CP violation in the B mesons and the measurement of the unitarity triangle parameters, the Belle II main focus is the investigation of physics beyond the SM via the precise measurement of SM parameters like CP asymmetries, as well as the observation of rare or forbidden decays.
The SuperKEKB accelerator is planned to reach an instantaneous luminosity of $\mathcal{L} = 8 \cdot 10^{35} cm^{-2} s^{-1}$, about 40 times more than KEKB. This large improvement will be accomplished not only increasing the circulating current, but also employing the nano-beams scheme, which was initially proposed for the SuperB experiment by P.Raimondi [24]. In this chapter, a description of the accelerator machine and detector components is given. Additional information can be found in [25].

2.1 SuperKEKB accelerator

The SuperKEKB will be the accelerator machine with the highest instant luminosity ever built. It is constructed specifically for the Belle II experiment and is placed in the same tunnel of its predecessor KEKB. SuperKEKB is an asymmetric e^+e^- machine that operates at a Center of Mass (CM) energy of 10.58 GeV, corresponding to the $\Upsilon(4S)$ mass resonance.

The beams energy are 4 GeV and 7 GeV, respectively for e^+ and e^- thus:

$$\sqrt{s} \simeq \sqrt{4E_{e^-}E_{e^+}} = 10.58\ GeV \tag{2.1}$$

assuming the approximation $m_{e^\pm} \ll E_{e^\pm}$. The energy asymmetry of the beams results in a Lorentz boost of the laboratory system with respect to the center of mass system of $\Upsilon(4S)$. This boost is represented by a $\beta\gamma$ factor of:

$$\beta\gamma = \frac{P_{e^-} - P_{e^+}}{\sqrt{s}} \simeq \frac{E_{e^-} - E_{e^+}}{\sqrt{4E_{e^+}E_{e^-}}} \simeq 0.28\ . \tag{2.2}$$

The CM boost is needed in order to resolve the decay vertex positions of the B mesons coming from $\Upsilon(4S)$. The B mesons have low momentum in the CM system so, in the laboratory system, they are produced almost parallel to the boost direction; the Lorentz boost amplifies the separation in z between the decay vertices. Considering the Belle II boost of $\beta\gamma = 0.28$, the flight distance of the B mesons is around 130 μm. These distances can be resolved with the high resolution achieved by the Belle II vertex detectors. The increase in luminosity requires a reduction in the boost compared to the value used in KEKB, $\beta\gamma$=0.42. To compensate for the reduction in the vertex separation, a more precise vertex detector has been developed for Belle II.

The electron beam of the SuperKEKB is produced in the pre-injector accelerator through the interaction of an impulsed laser with a cathode. Then electrons are accelerated with a linear accelerator (Linac) up to 7 GeV. A part of these electrons are used to produce positrons through the interaction with a tungsten target located in the middle of the Linac accelerator. These e^+ are produced with a larger emittance than required, thus they need to be injected into a Damping Ring (DR) in order to reduce it to the level needed for high luminosity operation. After this process, they are accelerated using the remaining half part of the Linac up to 4 GeV.

Electrons are injected into the High Energy Ring (HER) while positrons into the Low Energy Ring (LER) and the collisions take place at a specified Interaction Point (IP). The beams are not perfectly head-on as they have a crossing angle of $2\phi = 83\ mrad$, which is about 4 times larger than KEKB. This value is chosen mainly by considerations related to the optics of the beams; with a large crossing angle, the final focus quadrupole magnets can be independent for the two beams and they can be placed closer to the IP. A schematic view of the acceleration processes is shown in figure 2.1.

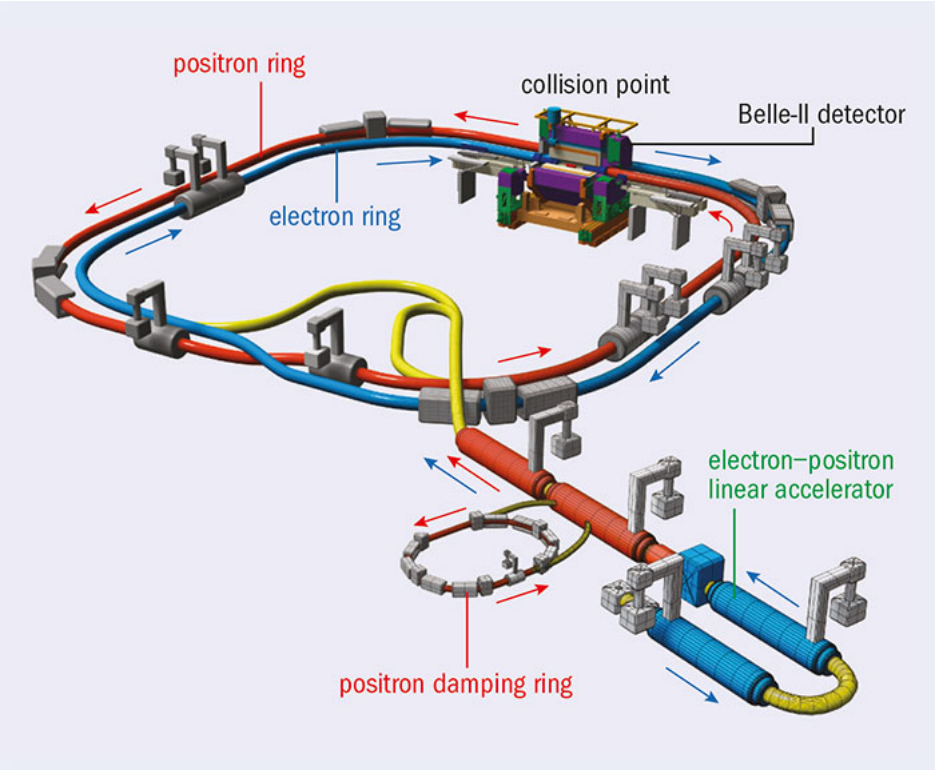

Figure 2.1: SuperKEKB accelerator system, from the production of the beams to the collisions at the IP.

2.1.1 Nano-beams scheme

The Belle II experiment will be able to reach a high luminosity thanks to the new idea of the nano-beams scheme, that consists in the minimization of the transversal dimensions of the colliding beams in order to improve the probability of e^+e^- to collide. This minimization is done reducing as much as possible the betatron function β_y^*, that represents the transverse spread of the particles circulating in the collider with respect to their nominal trajectory. Furthermore, in order to obtain a small size of the overlap region d (transversal bunch length), the horizontal emittance and the betatron function should be small (fig. 2.2).

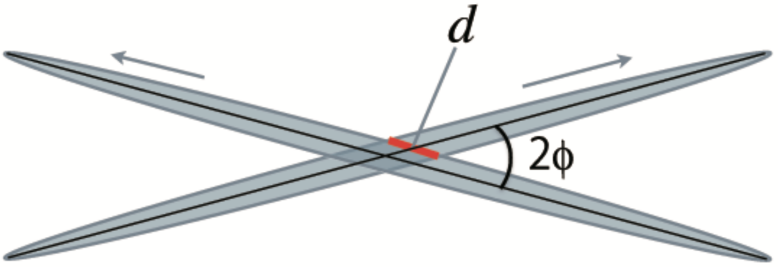

Figure 2.2: Schematic view of the nano-beams scheme adopted.

The luminosity of the accelerator machine is expressed as follows:

$$L = \frac{\gamma_{\pm}}{2er_e}\left(1 + \frac{\sigma_y^*}{\sigma_x^*}\right)\frac{I_{\pm}\xi_{y\pm}}{\beta_{y\pm}^*}\frac{R_L}{R_{\xi_y}} \tag{2.3}$$

where r_e, e and γ are respectively the electron classical radius, the elementary electric charge and the Lorentz factor. The $\pm$ signs distinguish the positron (+) from the electron (-) and the ratio between the parameters R_L and R_{ξ_y} represents a geometrical reduction factor, that takes into account the crossing angle. The overall value of the parameters just mentioned is around 1 so the luminosity depends on the other parameters: the total beam current ($I_{\pm}$), the vertical beam-beam parameter ($\xi_{y\pm}$) and the vertical beta function at the IP ($\beta_{y\pm}^*$). A comparison between KEKB parameters and SuperKEKB with the nano-beams scheme is shown in figure 2.3.

	KEKB Design	KEKB Achieved : with crab	SuperKEKB High-Current	SuperKEKB Nano-Beam
Energy (GeV) (LER/HER)	3.5/8.0	3.5/8.0	3.5/8.0	4.0/7.0
β_y^* (mm)	10/10	5.9/5.9	3/6	0.27/0.42
ε_x (nm)	18/18	18/24	24/18	3.2/2.4
$\sigma_y(\mu m)$	1.9	0.94	0.85/0.73	0.059
ξ_y	0.052	0.129/0.090	0.3/0.51	0.09/0.09
σ_z (mm)	4	~ 6	5/3	6/5
I_{beam} (A)	2.6/1.1	1.64/1.19	9.4/4.1	3.6/2.6
$N_{bunches}$	5000	1584	5000	2503
Luminosity (10^{34} cm^{-2} s^{-1})	1	2.11	53	80

Figure 2.3: Overview of the SuperKEKB and KEKB parameters [25]. The comparison shows how the nano-beams scheme improves the luminosity.

The Belle II experiment expects to collect data for an integrated luminosity of 50 ab^{-1} in ~5 years of data taking. The luminosity profile of SuperKEKB is reported in figure 2.4.

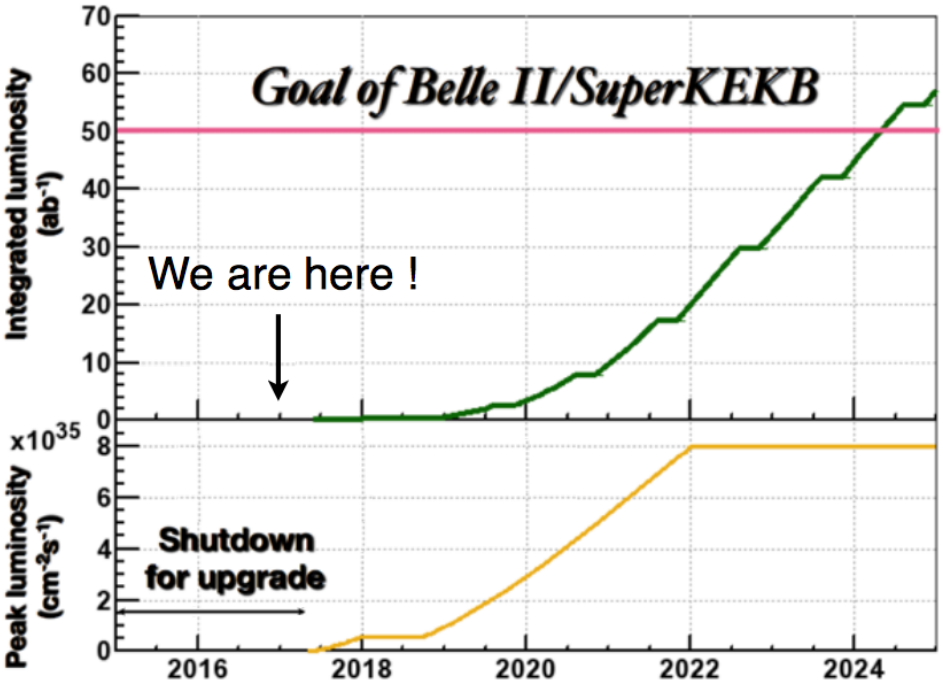

Figure 2.4: Luminosity profile of the SuperKEKB collider.

2.2 The BelleII detector

In order to take advantage of the high luminosity provided by the SuperKEKB machine, the Belle II detector needs to be improved with respect to its predecessor in Belle. The main changes are dictated by the increased event rate and machine backgrounds, as well as the already mentioned reduced CM boost. In general the goal of the Belle II detector design has been to obtain at least the same performances achieved by the Belle detector. The overall detector structure remains the same, with concentric cylindrical layers of detector elements. The overall mechanical structure is retained along with the superconducting 1.5 T magnet, the steel return yoke and the electromagnetic calorimeter. The tracking detectors, the particle identification detectors, as well as most of the readout electronics are instead replaced to cope with the new running conditions.

As in most high-energy physics experiments, the detection region is made by layers of detectors with cylindrical geometry; the central part is called barrel while the forward and backward regions are called end-caps. The end-cap detector consists in detector layers oriented perpendicular to the beam axis. In the innermost part of the detector, a

completely new silicon PiXel vertex Detector (PXD) is introduced, followed by 4 layers of Silicon-strip Vertex Detector (SVD). Moving out radially, the Central Drift Chamber (CDC) is installed, with the purpose of tracking charged particles together with the PXD and the SVD. Beyond the tracking detectors, a Particles IDentification (PID) system is placed. It consists of a Time-Of-Propagation counter (TOP) located in the barrel section (the central part of the cylinder) and of an Aerogel Ring-Imaging Cherenkov detector (ARICH) located in the forward part of the cylinder (forward end-cap). After the PID detectors, one finds the ELectromagnetic Calorimiter (ECL), providing a measurement of the energy of photons and electrons, followed by the super conductive solenoid. In the segmented return yoke of the magnet, the K-Long and Muon detector (KLM) is installed, with the ability of reconstructing long lived particles as K_L and μ. An overview of the whole Belle II detector is given in figures 2.5 2.6.

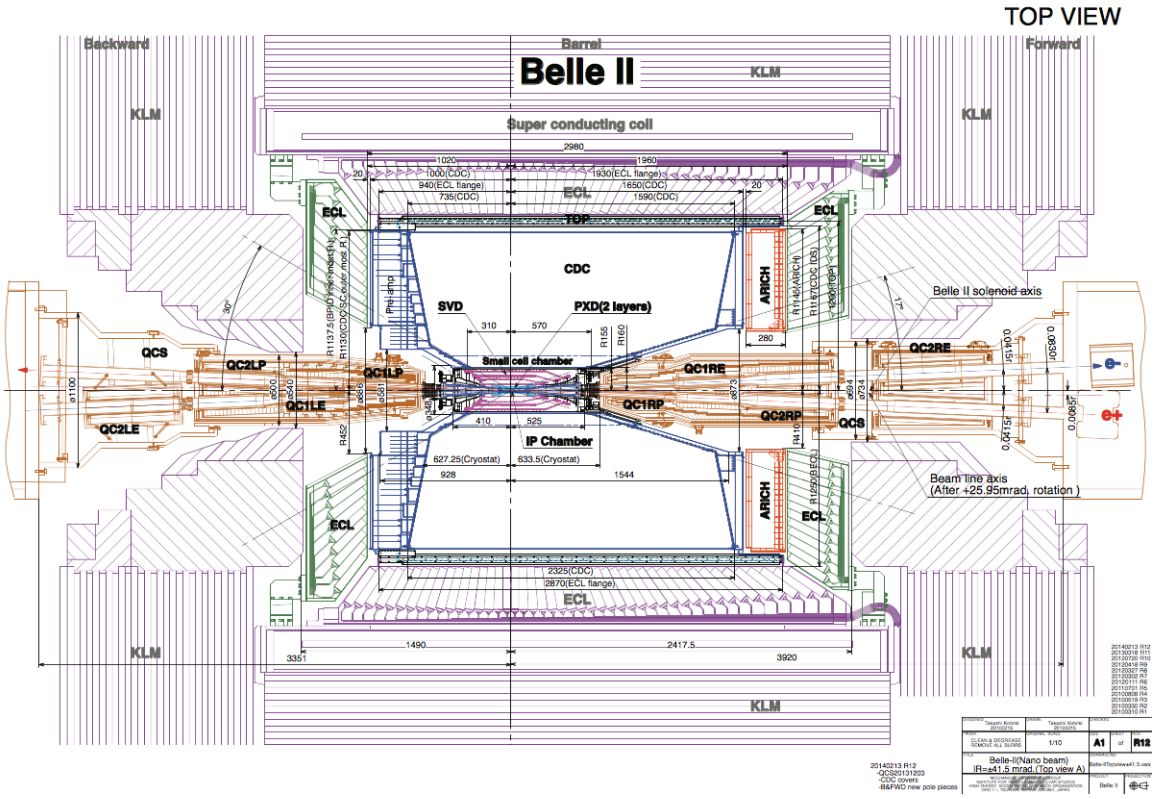

Figure 2.5: Overview of the Bell II detector. Here the geometry and all the detection components of the whole detector, from the innermost to the outermost layer, are represented.

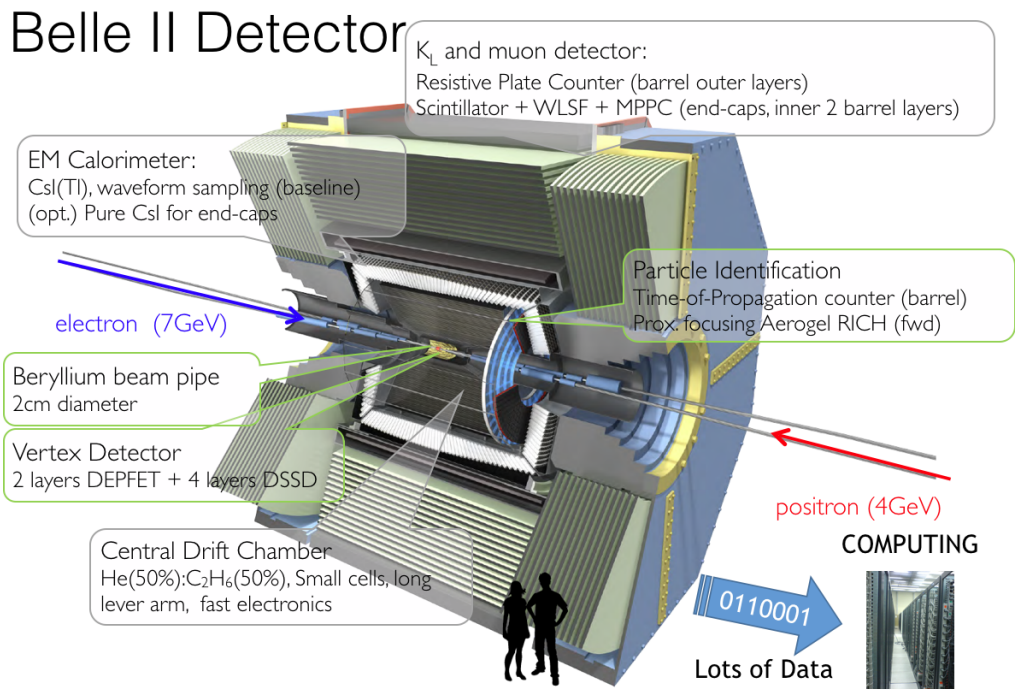

Figure 2.6: 3-D view of the whole Belle II detector; all sub detectors are displayed.

2.2.1 Pixel vertex detector

The pixel vertex detector consists in two layers of pixel sensors based on DEPleted Field-Effect Transistor (DEPFET) technology. The two layers are placed close to the IP, respectively at 1.4 cm and 2.2 cm radially. In this region it is not possible to use a strip detector because of high hit rates coming from background contributions, which would affect too much the occupancy of the strips. The small dimension of the single pixel (50 x 50-55 μ for the innermost layers and 50 x 70-85 μm for the outermost ones) reduces the occupancy problem and leads to an higher vertex resolution of ~ 10 μm. For low momentum particles, the reconstructed position is limited by the Coulomb multiple scattering so the material budget is required to be kept below $\sim 0.2\%$ X_0 for each layer.

Each pixel consists in a semiconductor detector that combines detection and amplification processes within the same device. It consists in a p-channel Metal Oxide Semiconductor FET (MOSFET) or a Junction FET (JFET), integrated onto a silicon substrate that becomes fully depleted if a sufficient reverse bias is applied. A deep n-doping implant, called internal gate, is located at ~ 1 μm under the transistor channel and it creates a minimum of potential. When an incident particle passes through the pixel detector, it generates electron-hole pairs in the substrate and the generated electrons are then collected by the internal gate. The latter acts as a back gate for FET transistor channel, meaning that the

charge located on it modulates the drain current through the transistor. This current is used as detection signal and it can be readout in a non destructive process. The signals are amplified in the periphery of the chip at the end of a column of pixels, with rows of pixels connected to the output in sequence. A schematic representation of a pixel detector and its operating principle are shown in figure 2.7.

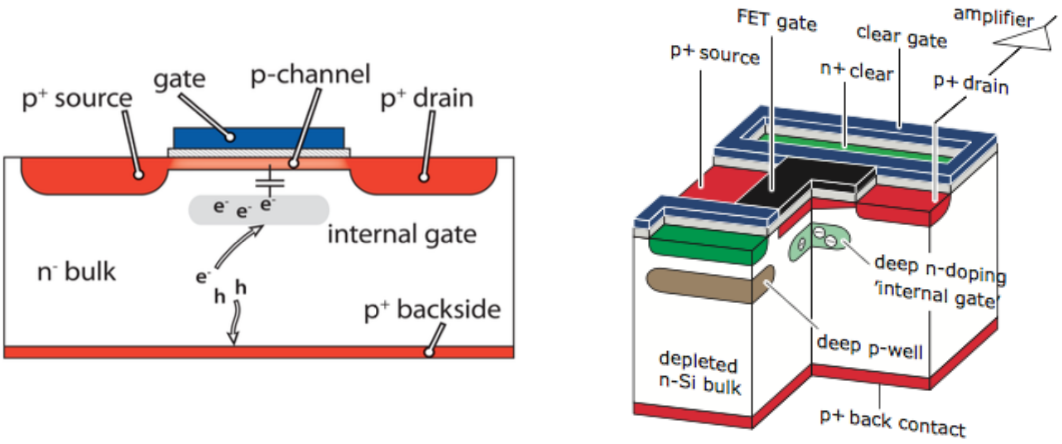

Figure 2.7: Section of a DEPFET pixel (left) and its schematic working principle (right).

2.2.2 Silicon-strip vertex detector

The silicon vertex detector consists in four layers of Double-sided Silicon Strip Detectors (DSSDs) with an asymmetric polar angular acceptance that goes from 17° to 150°; this asymmetry comes from the boost of the CM frame due to the asymmetric energy beams. A three-dimensional rendering of the PXD and SVD system is shown in fig. 2.8. The four layers are made of several ladders that are composed by DSSDs (from 2 to 5 sensors depending on the layer). Each ladder overlaps with the adjacent with $\sim 8-10\%$ of the sensors area, in order to cover the whole $r-\phi$ plane. The strips on the n-side of the sensors (that are oriented along the r-ϕ plane) are orthogonal to the strips on the p-side (oriented along the z axis). This allows to obtain the best reconstruction of the position of particles (more details on the sensors can be found in chapter 3). For the last three layers (number 4, 5 and 6), trapezoidal slanted sensors are used in the forward region while rectangular sensors are used in the central and backward regions as shown in figure 2.9. The use of the more complex trapezoidal geometry in the forward region allows a reduction of the total silicon area and of the crossing angle of the particles, resulting in cost savings and performance improvements for the same forward coverage.

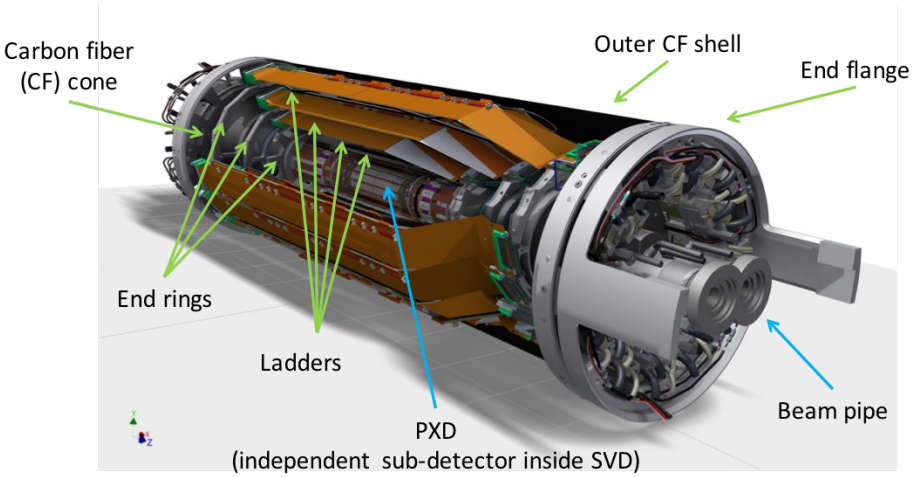

Figure 2.8: Schematic view of the entire Belle II vertex detector. Here the PXD and the SVD detectors are displayed.

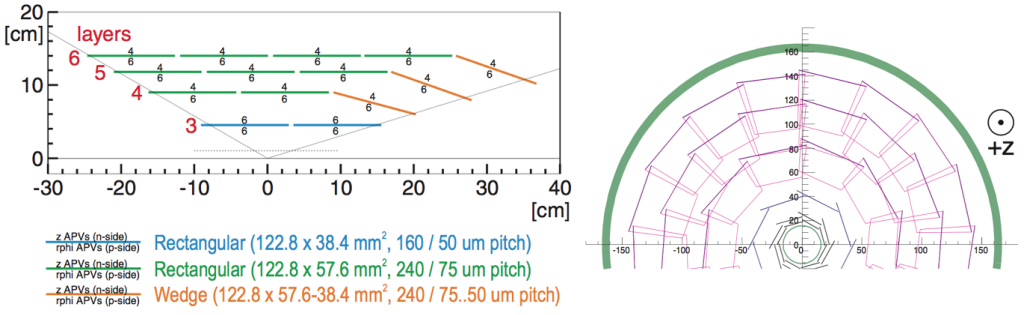

Figure 2.9: Schematic geometry of the Silicon Vertex Detector: the longitudinal section (left) and the transversal section (right) are shown. Dimensions are in mm.

The readout process is performed by the APV25 chips, that were used by the CMS experiment [26]. They are placed on a read out board called Hybrid Sandwich (HS). Each chip contains 128 channels with a low noise charge sensitive preamplifier, followed by a shaper stage with a shaping time of 50 ns. They provide a faster shaping time with respect to the chips used in Belle, allowing to maintain a low occupancy of the SVD layers and to read signals in a faster way. In a recent test beam (April 2016 at DESY, Hamburg), a sector of the Belle II SVD and PXD have been mounted (fig. 2.10). In that occasion the hit reconstruction efficiency and the hit resolution were estimated. The average efficiency of hit reconstruction is found to be above 99.5% while the hit resolution is $\sim 11\ \mu m$ in r-ϕ direction and $\sim 30\ \mu m$ in z direction [27].

The combination of the PXD and SVD (called the VXD) provides excellent vertex resolution as well as the reconstruction of low momentum tracks that do not reach the CDC.

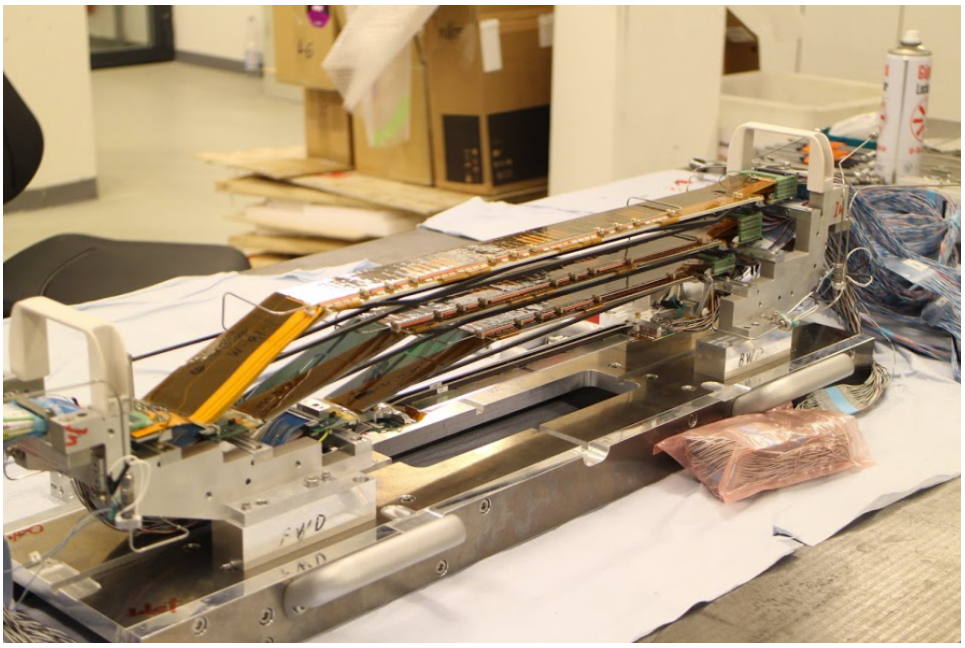

Figure 2.10: Picture of the four SVD ladders mounted for a test beam at DESY.

In figure 2.11 (right) the error on the impact parameters as a function of the transverse momentum of tracks is shown.

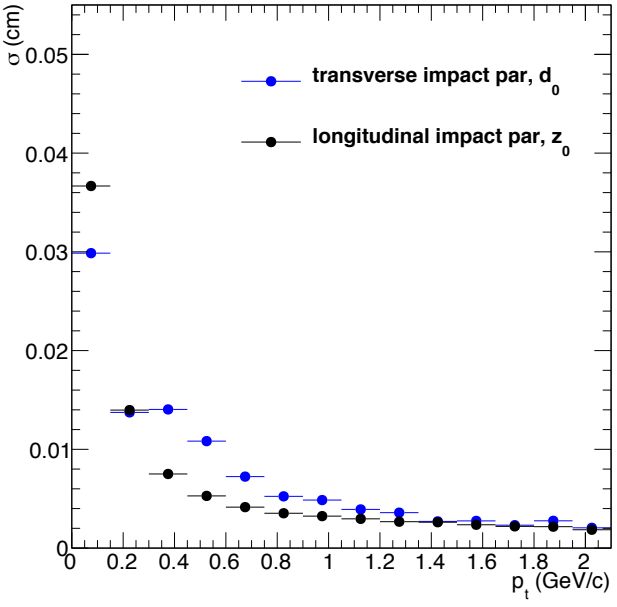

Figure 2.11: Transverse (blue) and longitudinal (black) impact parameters error as a function of the track transverse momentum.

2.2.3 Central Drift Chamber

The central drift chamber of Belle II plays three important roles:

- It reconstructs charged particle tracks and measures their momentum from deflections due to the magnetic field;
- It provides information about the particle identification process by measuring the energy loss within its gas volume;
- It provides trigger signals for charged particles.

The CDC is a large gaseous detector (50 % He, 50 % C2H6) composed by 56 cylindrical layers of wires, divided into 9 super-layers. The super-layers alternate between stereo and axial layers; the stereo angles goes from $\sim$ 45 mrad to ~ -74 mrad and is necessary to measure the z coordinate of the tracks. Super-layer are composed of six layers, except for the innermost one which has two additional layers that contain active guard wires. The radial cell size is 10 mm for the innermost super-layer and 18.2 mm for the other super-layers. The chamber inner radius is 16 cm while the outer radius is 113 cm, and the geometrical acceptance goes from 17° to 150° in θ. The CDC provides a position resolution of $\sim$2 mm in z and $\sim$100 μm in r. The resolution on the energy loss by a charged particle inside the chamber is $\sim$12%, for incoming particles at $\theta = 90°$. There are three main structural components of the CDC: a carbon-fiber inner cylinder, two aluminium endplates and a carbon-fiber outer cylinder. The two aluminium endplates have complex conical shapes to maximize acceptance avoiding excessive rates coming mainly from Bhabha scattering. The front-end electronic is located near the backward endplate and it uses a new Application-Specific Integrated Circuit (ASIC) chip that incorporates an amplifier, a shaper, and a discriminator. The new readout system must handle higher trigger rates with less deadtime, with respect to the readout system of Belle. The Belle II CDC and its electronics have been installed in the experiment in December 2016.

2.2.4 Particles identification system

The Belle II particle identification system is composed by two detectors: the Time Of Propagation counter (TOP) and the Aerogel Ring-Imaging CHerenkov counter (ARICH). The TOP detector uses the Cherenkov effect to provide information to identify charged particles in the barrel section. It consists in 16 quartz bars placed between the CDC

outermost cylinder and the electromagnetic calorimeter. When a charged particle passes through the quartz bars, Cherenkov radiation is emitted with an angle θ_C with respect to the direction of motion of the particle. The cosine of θ_C is inversely proportional to the speed of the particle and to the refractive index of the material. Thus Cherenkov photons are emitted at different angles, depending on the mass of the incoming particle. The photons generated into the quartz propagates through the bars due to the total internal reflection with the internal surfaces of the quartz (fig. 2.13). A mirror is placed at the forward end of the bars, in order to reflect any photons that hit it, while at the backward end of the quartz bars is an array of Micro-Channel Plate (MPC) PMTs that measure the x position and the precise time of arrival of incident photons (fig. 2.12).

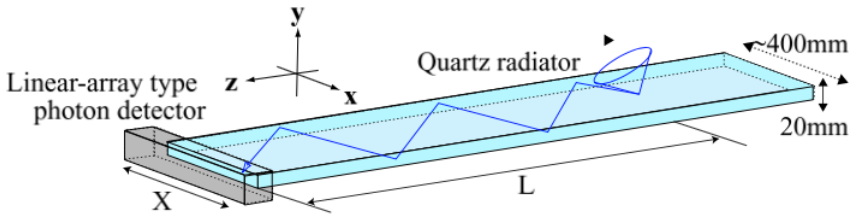

Figure 2.12: Quartz bar design. Here the Cherenkov cone and the propagation of the photons towards the MPC-PMTs are shown.

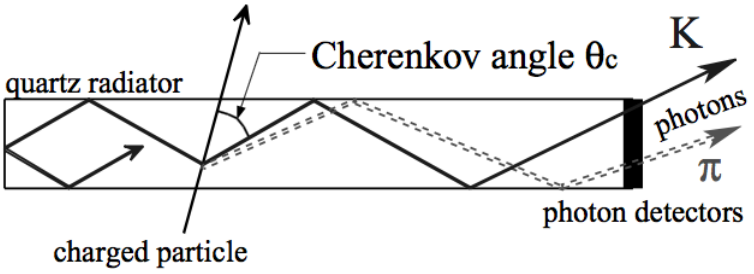

Figure 2.13: Total internal reflection of Cherenkov photons produced by kaons and pions inside a quartz bar. Here different Cherenkov angles are shown.

The MCP-PMTs have excellent timing and gain performance: the transit time spread is around 30 ps and the gain is $\sim 10^6$ for single photo-electrons, even with the presence of a magnetic field of 1.5 T. Each PMT is divided into 4x4 channels, giving a total of 512 channels per bar. The readout system includes two waveform sampling ASIC per PMT. The charge deposited on a MCP-PMT anode is converted to a waveform that will be used to determine the photon detection time, with a resolution of 50 ps.

The ARICH detector is placed in the forward endcap and its working principle is

also based on the Cherenkov effect, measuring directly the circle formed by the emitted photons. The ARICH is composed by several elements as in figure 2.14 (left):

- Silica aerogel Cherenkov radiator: the charged particles pass through the aerogel generating Cherenkov photons. This radiator should be highly transparent in order to avoid absorptions or scattering processes of the generated photons;
- Expansion volume of 20 cm: the Cherenkov radiation cone, originated in the aerogel detector, "expands" in order to form a ring on the photon detector placed at 20 cm from the silica radiator;
- Photon detector: it consists in an array of Hybrid Avalance Photo-Detector (HAPD), each composed by a vacuum tube with enclosed Avalance Photo-Diode (APD) sensor (fig. 2.14 right). Those are pixelated into 6 x 6 pads which provide position measurements; each pad has a size of 4.9 x 4.9 mm^2. The photons enter the HAPD and generate photoelectrons from the interaction with a bialkali photocathode. Thus the photoelectrons are accelerated with an electric field and send to the APD, which amplifies the signal of a factor ~40. About 10 photons have to be detected in order to generate the ring image with the necessary precision (this number depends on the aerogel radiator thickness);
- Readout system: it is able to readout the ~80000 channels of the photon detector using the ASIC chips, mentioned in the previous sections.

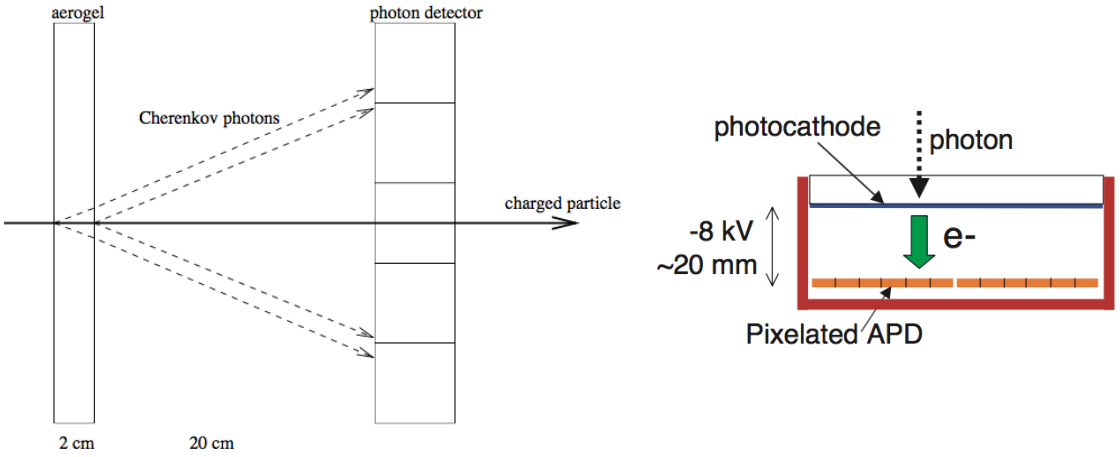

Figure 2.14: Left: schematic view of the ARICH detector. Right: schematic view of an APD hybrid and its working principle.

The resolution per charged particle is one of the most important parameter of a RICH counter. It is defined as $\sigma_{track} = \sigma_0/\sqrt{N}$ where σ_0=14.3 mrad is the single photon resolution coming from a charged particle while N is the number of photon detected. The number of photons increases with the radiator thickness but, at the same time, also the emission point uncertainty of the radiation does. The adopted solution consists in a non-homogeneous aerogel radiator, using two different refractive indices for the 2 layers of aerogel: n_1=1.046 and n_2= 1.056. This allows to focus the Cherenkov rings on the photon detector increasing the precision of radius measurements. From test beam results, $\sigma_{track} \simeq$3.1 mrad with 20 photons detected per charged track.
The final identification of a particle obtained through the Belle II PID system is based on the value of a Likelihood function, that takes into account the information coming from the PID detectors and the CDC.

2.2.5 Electromagnetic calorimiter

The Belle II Electromagnetic CaLorimeter (ECL) consists of a 3 m long barrel section with an inner radius of 1.25 m and annular end-caps at z = 1.96 m (forward) and z = -1.02 m (backward) from the interaction point. The calorimeter has a polar angular acceptance that goes from 12.4° to 155.1°. The barrel part contains 6624 CsI(TI) crystals of truncated pyramid shape, with an average size about 6 x 6 cm^2 in cross section and 30 cm in length, corresponding to about 16 X_0. Each of these crystals points to the IP position. The end-caps part contains 2112 crystals for a total number of crystals of 8736 and a total mass of about 43 tons. Each crystal is wrapped with a 200 μm layer of Gore-Tex teflon and it is covered by a laminated aluminium sheet of 25 μm and a mylar sheet of 25 μm. Belle II ECL reuses the crystals of the Belle experiment, but the readout electronics is replaced with a waveform sampling one with which it is possible to distinguish multiple photons in the same time window and therefore improve resolution and background rejection.
For what concerns the scintillation light readout system, two 10 x 20 mm^2 photo-diodes are glued to the rear surface of the crystal. Some LED are used to inject light pulses into the crystal volume to monitor the optical behaviour. A pre-amplifier is attached to each photo-diode and it's able to provide two independent output signals from each crystal. In order to eliminate the heat generated by the pre-amplifiers a water cooling system is used. The average output signal coming from the crystals, calibrated with cosmic ray muons, is about 5000 photoelectrons per MeV, while the noise level is about 200 keV. Furthermore,

the intrinsic energy resolution of the calorimeter can be approximated as:

$$\frac{\sigma_E}{E} = \sqrt{\left(\frac{0.066\%}{E}\right)^2 + \left(\frac{0.81\%}{\sqrt[4]{E}}\right)^2 + (1.34\%)^2} \tag{2.4}$$

where the energy is measured in GeV.

2.2.6 K_L and μ detector

The KLM provides the particle identification for particles with high penetration power (mainly $\mu^{\pm}$ and K_L). The detector is placed outside the superconducting solenoid and is composed of alternating layers of active counters and iron plates which provide 3.9 interaction lengths of material. The whole KLM covers an azimuthal angle between 20° and 155°. It can be divided into a barrel part (BKLM), oriented parallel to the z axis, and a new part installed in the end-cap region (EKLM). The active elements of the BKLS are Resistive Plate Chambers (RPC) but, for the two innermost layers of the barrel region and the whole EKLM the active elements are plastic scintillators. The scintillator strips have a cross section of (7-10) x 40 mm and a length of ∼2.8 m. They accommodate Wave Length Shifter (WLS) fibers in the center, in order to guide the light to the strip ends where SiPMs (Silicon Photo Multiplier) are coupled. The SiPMs consist in a matrix of pixel photodiods that have a time resolution of less than 1 ns allowing the KLM to provide measurements of the K_L time-of-flight. With SuperKEKB, the background rate will be much higher with respect to KEKB, thus the plastic scintillator layers in the barrel and end-cap regions are inserted in order to cope with the high rate foreseen at this radius. For the Belle experiment, only RPC elements were used. The RPC consists in two parallel sheets of float glass (the electrodes) separated by 1.9 mm of free space. This gap is filled with a gas mixture composed by 62% HFC-134a, 30% argon, and 8% butane-silver. The high voltage is applied to the electrodes through a thin layer of carbon-doped paint, placed on the outer surfaces of each electrode.

The reconstruction efficiency of muons with 1 GeV momentum is found to be ∼ 89% in the barrel section of the KLM while, for particles with momentum higher than 3 GeV, the K_L reconstruction efficiency is around 80%.

2.3 Trigger

In order to manage the SuperKEKB high luminosity, that increases the total event rate to ∼20 kHz, a robust trigger system is needed. The clean environment of the e^+e^- collision allows relatively simple trigger strategies, using the number of charged tracks and the calorimetric energy. Nonetheless, several interesting physics categories would require very low multiplicity triggers (τ and two-γ physics) or even single photon triggers (dark photon searches), which are difficult to realize in the presence of high rate Bhabha processes.
The trigger system is divided into a Level 1 trigger (L1) and a High Level Trigger (HLT) which are respectively implemented in the hardware and in the software.
The L1 trigger is composed by many sub-trigger systems which summarize the information coming from each sub-detectors and sends them to the Global Decision Logic (GDL), that issues a trigger signal when its criteria are satisfied. All the trigger components are based on a new technology, with respect to Belle, that uses a Field Programmable Gate Array (FPGA) logic. A large part of the L1 trigger information are provided by the CDC and the ECL.
The CDC adds information on the z coordinate of the track, allowing to reject background events with a z-position far from the interaction region. The z coordinate has to be reconstructed in less than 1 μs; the trigger latency is 5 μs maximum and, using a neural network system, that requirement is met.
The ECL trigger system uses two complementary configurations: a trigger signal based on the total energy, that is sensitive to events with high electromagnetic energy deposition, and an isolated-cluster counting trigger, that is sensitive to multi-hadronic physics events with low energy clusters. The calorimeter trigger system can identify BhaBha scattering and $\gamma\gamma$ events (back-to-back topology) with high efficiency. This allows to maintain a high trigger efficiency for low multiplicity processes.
The HLT is divided into two levels: the Level 3 trigger (L3) and the physics-level trigger. The former selects events taking into account the track multiplicity, the total energy and the vertex position leading to a background reduction of almost 50%. The latter can exploit the full event reconstruction and uses offline code in order to select, for instance, low multiplicity events. The HLT provides a total reduction of the event rate of ∼12.5%.

The following chapters will describe in more detail the Silicon Vertex Detector and my contribution to the assembly work and to the understanding of sensor defects.

Chapter 3

Silicon-strip Vertex Detector

In this chapter, a detailed description of the Belle II silicon strip detector is given, together with the assembly procedures, with specific attention to the activities related to the forward and backward modules in which I have worked personally. Furthermore, the description of the standard electrical tests performed on the modules and some more detailed measurements done on them are reported.

3.1 Silicon strip detectors

Silicon radiation detectors are based on a reverse-biased p-n junction. In the depleted region of a p-n junction, which is regulated by the applied bias voltage (V_{bias}), an electric field is present that allows the collection of the charge released by interacting radiation (fig. 3.1). The diode structure and the reverse bias are also necessary to remove the free electrons and holes from the active region, since they are several order of magnitude more numerous than the particle signal.

When a charged particle passes through the detector, it looses energy due to the interaction with the material generating electron-hole (e-h) pairs (fig. 3.2). In a 300 μm silicon sensor, the number of e-h pairs produced by a Minimum Ionization Particle (MIP) is $N_{e-h} \simeq 3{\cdot}10^4$, considering the mean energy loss $(dE/dx)_{mean} = 388\ \frac{eV}{\mu m}$ and the energy to create a pair $E_{pair} = 3.63\ eV$. In the SVD strip detectors the thickness of the sensor is realized with high resistivity n-type silicon, allowing a moderate total depletion voltage (about 35 V), while the p and n implants on the two sides of the wafer are segmented in orthogonal strips to allow the readout of the two coordinates. As e-h pairs move in the electric field generated by V_{bias}, their drift motion to the strips generates a current in the sensor, which

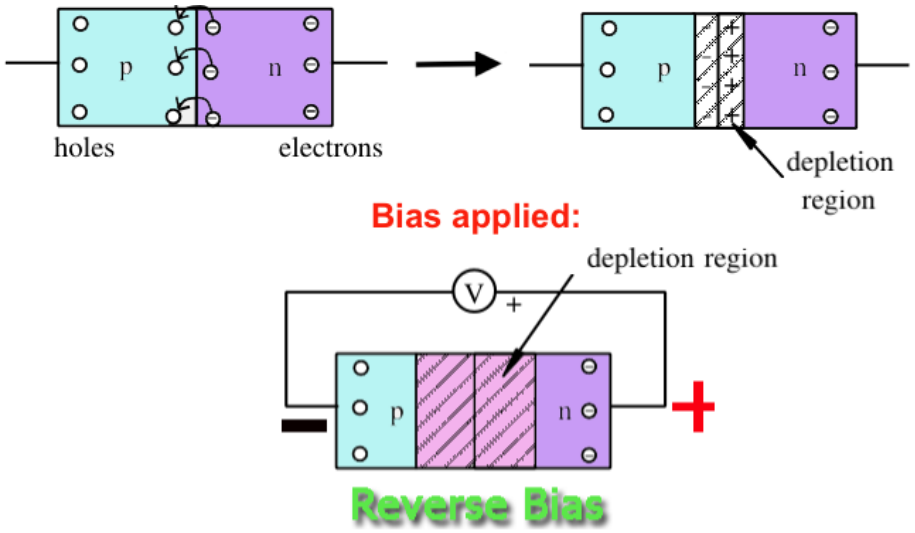

Figure 3.1: Scheme of the reverse bias mode working principle on a diod junction. When the bias voltage is not applied, electrons migrate towards holes and vice versa, due to a concentration gradient (top left). This motion creates a potential barrier and a small depletion region (top right). When the reverse bias V_{bias} is applied, the potential barrier increases and the depleted region enlarges, preventing the flowing of current (bottom).

represents our signal. The current generated in this way is collected mainly by the closest strip while the strips near to that one collect progressively less current. Then, the strip current flows through the amplification device and it finally reaches the read-out system, which is sensitive to the integrated charge collected by the strip.

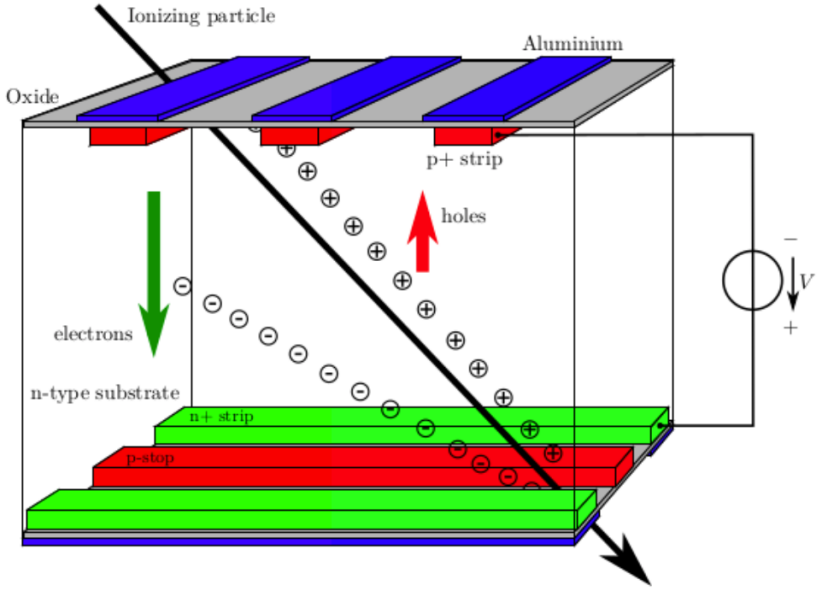

Figure 3.2: Working principle of a double-sided silicon strip detector. The e-h pairs generated by the incident particle are collected by the strips thanks to the bias voltage applied.

3.1.1 Sensors used in the Belle II Silicon Vertex Detector

The Belle II SVD employs three types of large size double-sided silicon strip detectors in order to achieve a low material budget. They are realized on six wafers with about 12 cm of length and 6 cm of width (see figures 3.3, 3.4 and 3.5). Additional information about the dimensions and the entire design can be found in [25] [28].

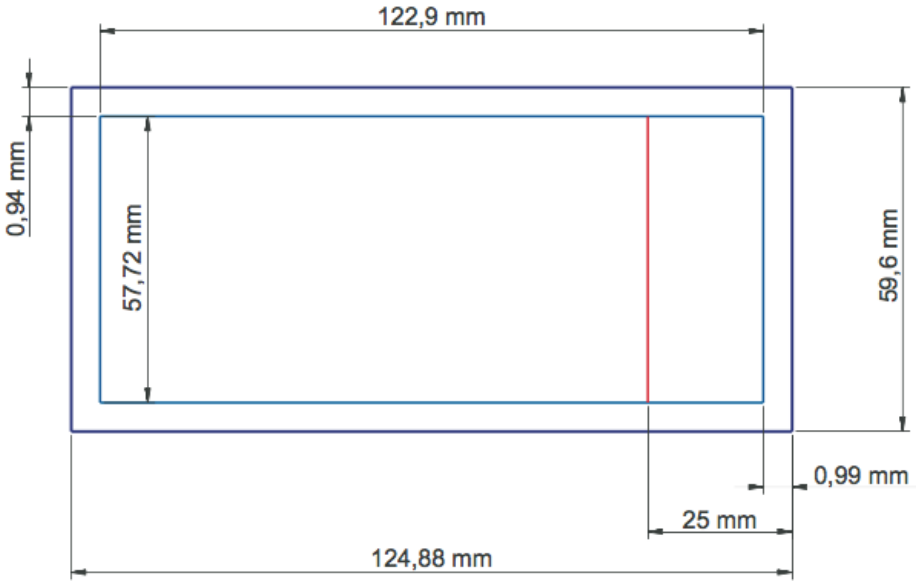

Figure 3.3: Geometrical dimensions of a large rectangular sensor. The light blue line represent the active area while the red one indicates the position of an additional row of pad.

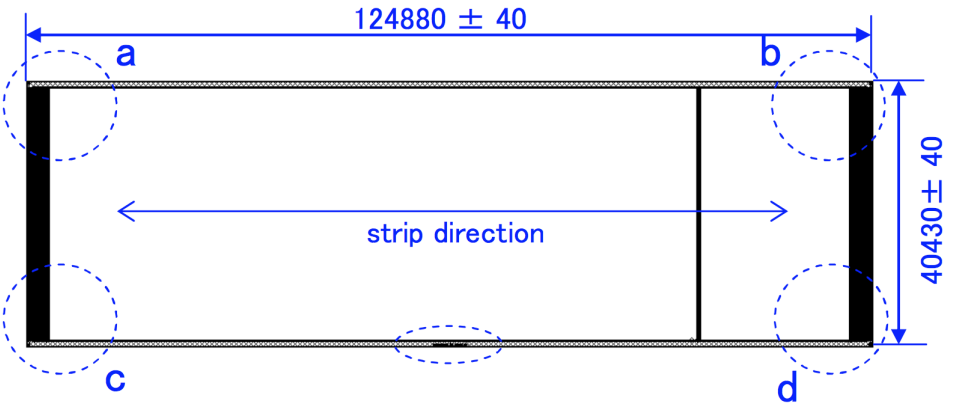

Figure 3.4: Geometrical dimensions of a small rectangular sensor. Here the p-side is displayed.

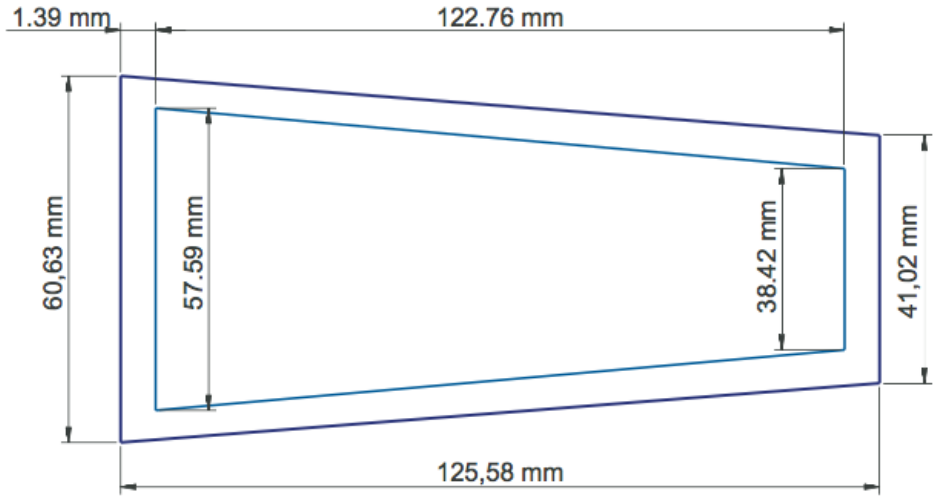

Figure 3.5: Geometrical dimensions of a trapezoidal FW sensor. The light blue line represent the active area.

The detectors used in the SVD are produced by:

- Hamamatsu Photonics (HPK) for the rectangular sensors used in the layer 3 and as barrel and backward (BW) sensors in layers 4 to 6 [29].
- Micron Semiconductor for the trapezoidal sensors used as forward (FW) sensors [30].

A summary of the geometrical properties of the sensors used in the Belle II SVD is shown in table 3.1.

Type	Active area $[mm^2]$	p-pitch $[\mu m]$	n-pitch $[\mu m]$	p-strips	p-strips
Large rectangular	122.8 x 57.6	75	240	768	512
Small rectangular	122.8 x 38.4	50	160	768	768
Trapezoidal	122.8 x 38.4-57.6	50-75	240	768	512

Table 3.1: Properties of rectangular and trapezoidal sensors used. The prefixes "p-" and "n-" indicate the sensors side.

More in detail, several important elements are present on the detector: the bulk, the strips, the p-stops, the oxide layer, the pads and the guard ring.
The bulk (or substrate) consists in a large n-doped region representing the active area of the detector. A bias ring surrounds the area where the strips are located and provides the bias voltage to each strips through an array of bias resistors R_{bias} (one per strip). The bias resistor consists in a polysilicon resistance integrated on the sensors, with a nominal value of about 10 $M\Omega$ (fig.3.6 left).

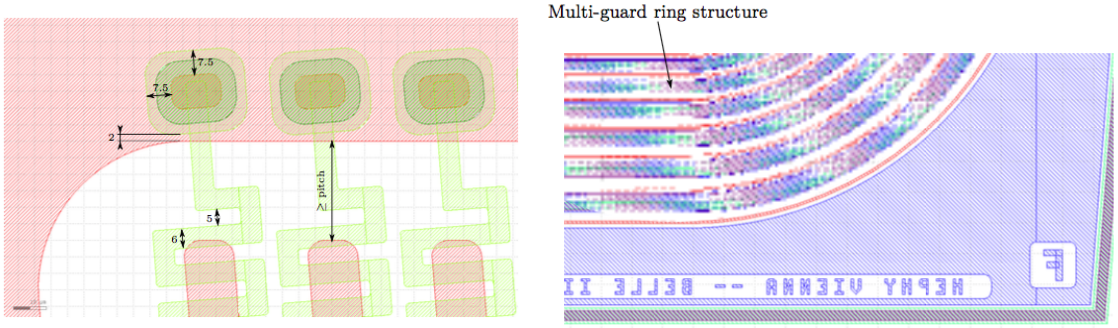

Figure 3.6: Left: design of the bias resistor and implanted strip ends. The p-type strips are in red and the R_{bias} is in light green. Right: bias ring structure.

A protection structure against the breakdown effect [31][1], called guard ring, is realized between the bias ring and the sensor edge. It consists of several concentric ring like structures, helping to protect the device from breakdown by lowering the electric field in a defined way towards the edge of the sensor (fig. 3.6 right).

The strip structure of the collection electrodes is obtained with ion impantation of p and n dopants on the two sides of the wafer. Between these strips, additional floating strips (not for read out) are implanted in order to increase the position resolution. The additional charge collected by the floating strips is transferred to the read-out ones though a capacitive coupling and using an analog readout, it is possible to perform charge interpolation to improve spatial resolution [28].

The strip implants are covered with a Silicon dioxide layer (SiO_2) to introduce a capacitive coupling between the strips and the readout electronics. Long aluminium strips forming the other plate of the capacitor are placed on top of the oxide. The metal strips are connected to the AC pads, which provide the connection to the readout electronics. Additional DC pads are directly connected to the strip implants and are used for electrical characterization. They allow, for example, to perform measurements regarding the currents generated in the substrate.

The silicon area between the implants is protected and electrically passivated with a layer of oxide. During construction, a fixed passive charge is formed in the oxide layer inducing an electron accumulation layer between the n-strips that would cause an undesirable connection between adjacent n-implants. Therefore, between the n-doped strips, p-type

[1] In presence of high electric field (greater than $\sim 10^5$ V/cm in silicon) electrons acquire enough energy to eject secondary electrons after collisions, which in turn can eject new secondaries. This condition produces a charge avalanche that can cause permanent damages to the sensors, if not controlled. High electric fields can build up at the sharp edges of a doping distribution or electrode structures; furthermore, also the presence of imperfections or defects on the silicon can lead to high electric field, thus to the breakdown.

implants are realized (p-stops); the p-stop structures cut off the n-channel surfaces, preventing the n-strips connections (fig. 3.7).

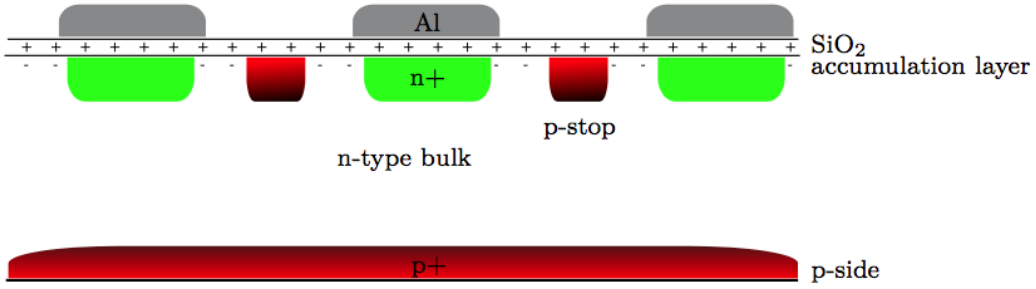

Figure 3.7: Schematic view of the section of a sensor (a small part of it) in which the p-stop structure are placed between n-strips. The p-stops interrupt the conductive layer induced by the oxide charge.

A detailed view of the strip, p-stop and pad geometry for the trapezoidal sensors is shown in figure 3.8.

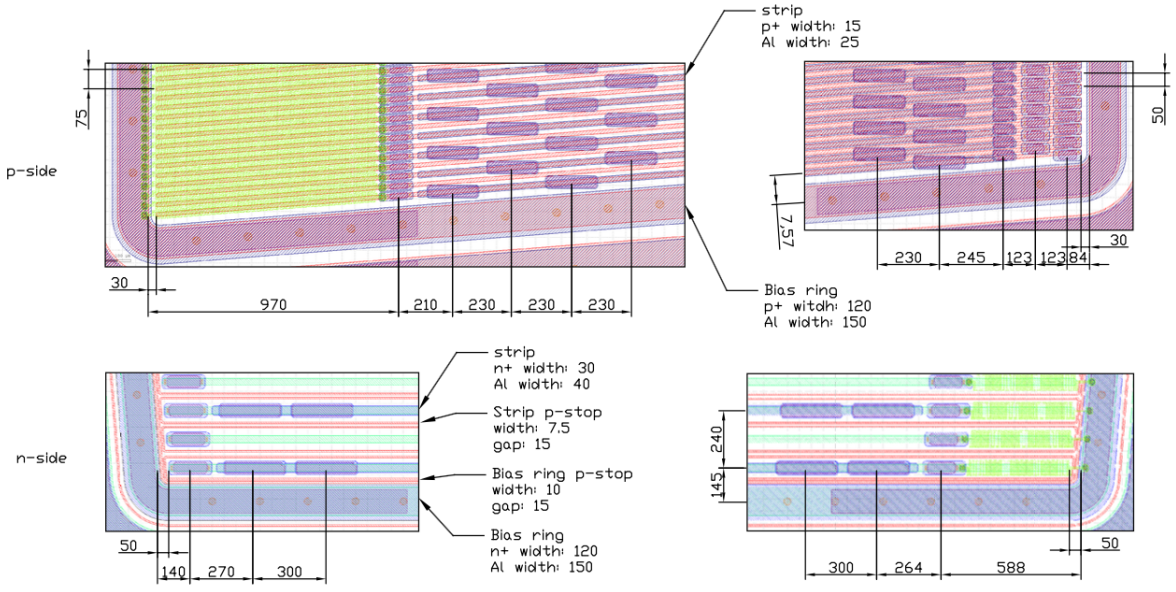

Figure 3.8: Detailed scheme of the most important areas of a forward sensor. The p-side is reported on top while the n-side on bottom [28].

3.2 Silicon Vertex Detector design

The Silicon Vertex Detector is composed of four layers of double-sided silicon strip detectors, implementing a fast readout based on APV25 chips [32] to cope with the high

luminosity and machine backgrounds. In order to avoid confusion between PXD and SVD, all layers of the VXD are numbered continuously, thus the layers of the SVD are labelled from 3 to 6; the sensors of the SVD are arranged in 7, 10, 12 and 16 ladders, which are concentrically installed around the beam pipe and the PXD in radii of 3.9, 8.0, 11.5 and 14.0 cm. Each ladder is composed of two to five DSSDs, excluding layer 3, which only has two small rectangular sensors. The other ladders are equipped with two to four large rectangular DSSDs in the barrel section and one trapezoidal sensor in the slanted forward section (fig. 3.9).

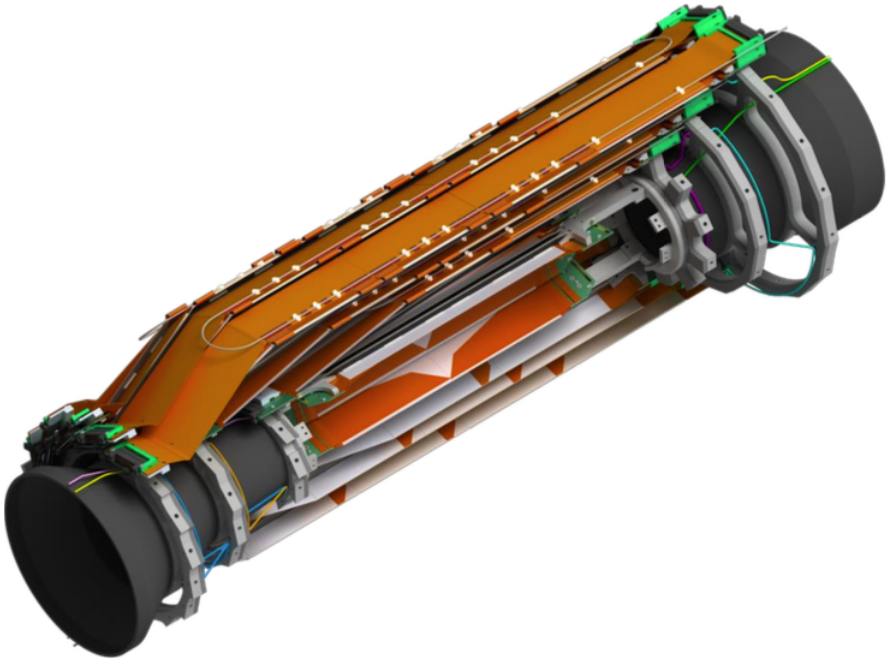

Figure 3.9: Representation of one half of the SVD. Here the cooling pipe tube and the endrings are also shown.

The mechanical support structure of the ladders consists in two carbon fiber reinforced ribs with a very light-weight AIREX® foam core, to which the sensors are glued with Araldite® 2011. These ribs are glued into end mounts made of aluminium, which are precisely screwed onto support rings on both ends of the detector. The rings are glued onto two carbon fiber cones, which are mounted to the end flanges. These flanges, placed at the forward and backward ends of the detector, are connected by a 1 mm thick carbon fiber shell, which encloses the whole VXD.

3.2.1 Ladder

The ladders of layer 3, which consist of two rectangular DSSDs, are read out conventionally by amplifier boards, using the APV25 chips accommodated at both ends of the ladder. The chips are connected to the sensors strips by flexible single layer pitch adapters made of Kapton. The ladders of layer four to six are composed of three sub-assemblies. The backward and forward sub-assemblies consist of the very backward rectangular and the trapezoidal forward sensors and their corresponding hybrid boards. As in layer three, the hybrid boards of these sensors are located outside of the Belle II active area and are connected to the APV25 chips by flexible pitch adapters. The implemented Origami chip-on-sensor concept [33] allows to read out the central DSSDs of the ladders using a single 3-layers flexible circuit attached on top of the sensor. This section of the ladder is called Origami sub-assembly and comprises one, two or three sensors for the layers four, five and six respectively.

The Origami chip-on-sensor concept

Figure 3.10 shows the structure of layer 5, which, in addition to the forward and backward modules, consists of two central DSSDs with two Origami circuits on top of them. In total there are three different Origami flex circuit designs and, according to their position on the ladder, they are named -z (backward), ce (central) or +z (forward). These three designs are electrically equivalent and only differ in the length of their tail part or, for the Origami +z which is only used in layer 6, also in the outer shape.

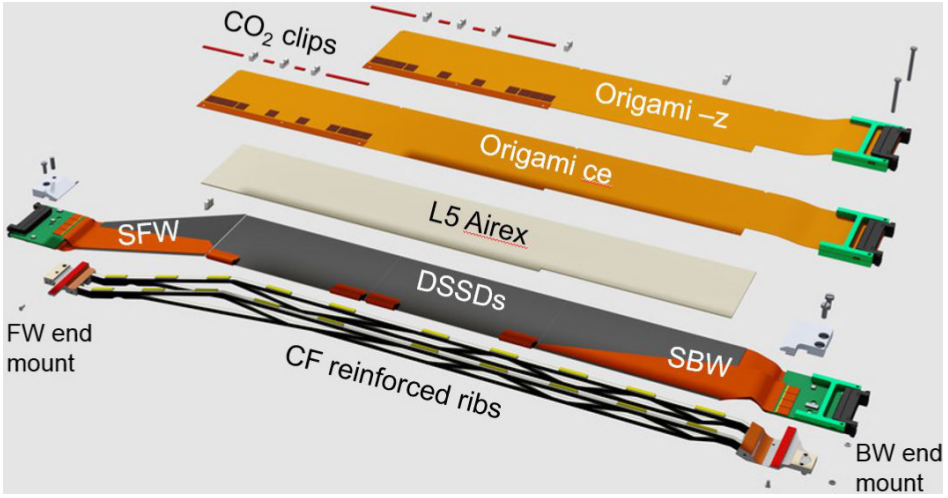

Figure 3.10: Exploded view of a layer 5 ladder of the Belle II SVD.

Between the flex circuits and the sensors, a 1 mm thick AIREX® sheet is inserted. This sheet provides electrical and thermal isolation, avoiding signal crosstalk and reducing the heat transfer from the chips to the sensors. The APV25 chips are thinned to 100 μm and attached to the Origami flexes using a thin layer of conductive adhesive. The strips on the top of the sensor are directly connected to the chips by wire bonds and a pitch adapter. Those of the bottom-side are attached by two flexible single-layer circuits (pitch adapters), which are bent around the edge of the sensor and glued close to the APV25 chips. This bending and gluing technique of the pitch adapters allows all chips to be connected to a single flex circuit on top of the sensor. All APV25 chips of the SVD are cooled by a highly efficient CO_2 system. Since the chips of an Origami sub-assembly are aligned in a row, each ladder needs only a single cooling pipe for the cooling of all chips in the sensitive volume 3.11. Hence the Origami concept ensures low noise (due to a short distance between read-out chips and sensor), efficient cooling and low material budget (the average material budget of a SVD ladder is about 0.60 % X_0).

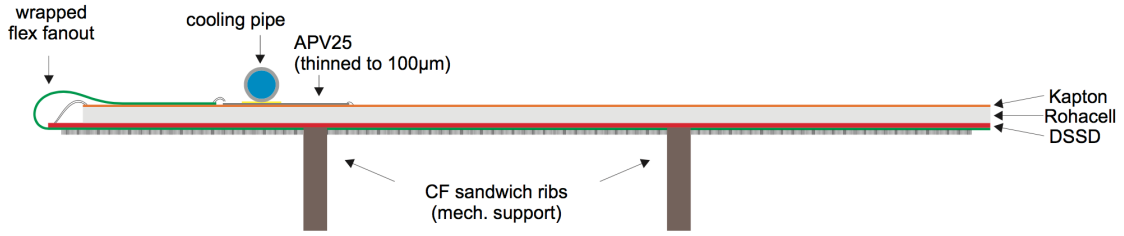

Figure 3.11: Side views of the Origami concept read out system.

3.2.2 Ladder assembly procedure

In this section, the procedure to build a SVD ladder is described, using layer 5 ladder as example (fig. 3.12). The main steps of the ladder assembly procedure can be divided into three main steps:

- production of forward and backward sub-assemblies and the mechanical structure;
- sensor and sub-assembly alignments, and construction of the Origami sub-assembly;
- ladder assembly, during which all the sub-assemblies are glued onto the ribs.

This three tasks are more or less independent and, a part of the work, can be performed in parallel. As an example, all the forward and backward sub-assemblies are produced and

electrically tested at the INFN in Pisa, and then are sent to the other assembly groups, in order to produce the ladders.

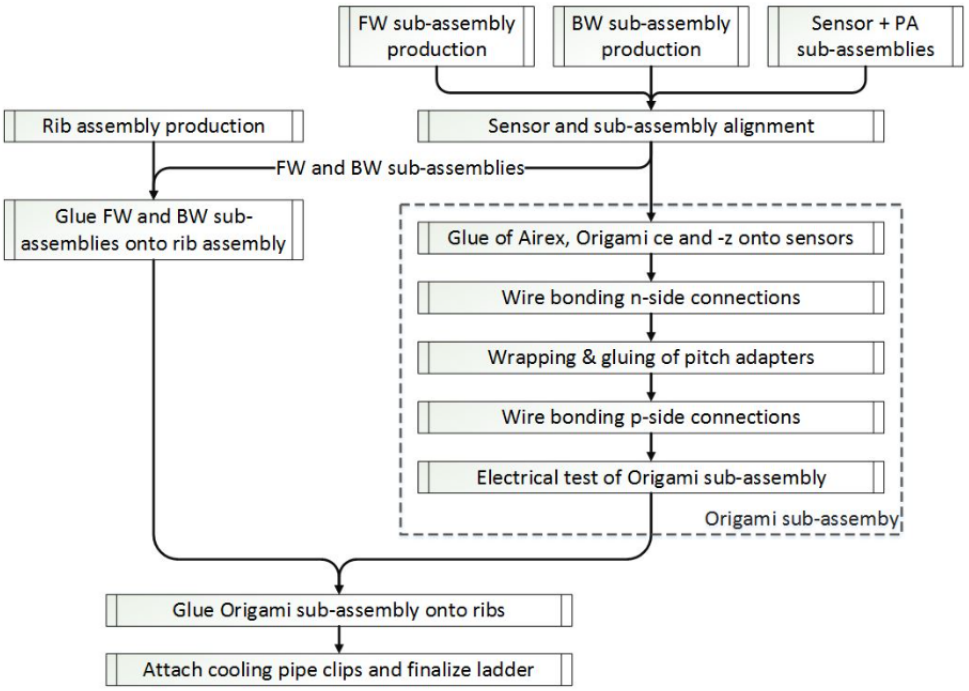

Figure 3.12: Schematic diagram of the main steps of the layer 5 ladder assembly procedure.

3.3 Forward-backward modules assembly in Pisa

The Pisa group is responsible for the assembly of the forward and backward module of 4^{th}, 5^{th} and 6^{th} layers. The assembly procedures take place in the INFN Pisa laboratories of high technologies, inside a clean room kept in constant overpressure in order to avoid contaminations. The complete modules are then send to the collaboration sites which create the ladders, in particular TIFR (Tata Institute of Fundamental Research in Mumbai, India) is making layer 4, HEPHY (Institute of High Energy Physics in Vienna, Austria) layer 5 and IPMU (Kavli Institute for the Physics and Mathematics of the Universe in Kashiwa, Japan) layer 6. Each site will send its ladders to the KEK laboratory, where the full SVD detector will be assembled. In the next sections the module components, the assembly procedure (gluing) and the electrical tests are described more in detail. The laboratory activity carried by the Pisa group has been an important part of this thesis work.

3.3.1 Components

The final assembled modules are composed by the sensor, the pitch adapter (PA) and the hybrid sandwich (HS) (fig. 3.13).

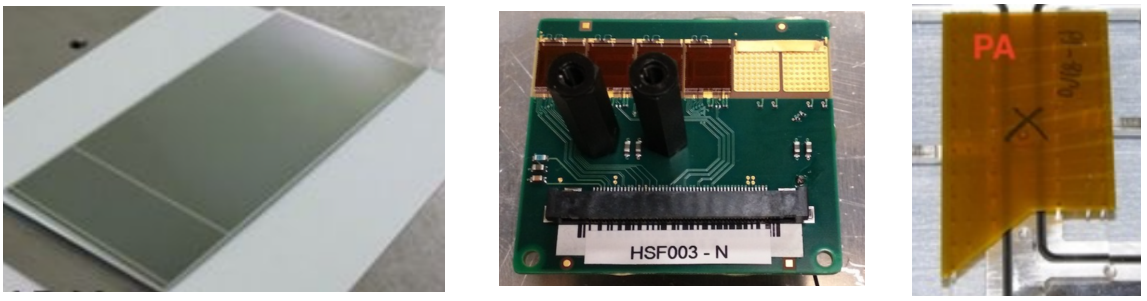

Figure 3.13: Backward silicon sensor (left), hybrid sandwich n-side up (center) and pitch adapter used for BW modules p-side (right).

The HS is connected to the forward and backward sensors through a flexible kapton layer, the PA, that contains fine pitch metal strips connecting the sensor to the electronics. The HS is made by two "single-side hybrids" glued together. One of the single-side hybrid allocates 4 APV25 chips (n-side) while the other allocates 6 chips (p-side). Each chip is connected to the board through micro-bonds, made with Al+Si wire of 25 μm of diameter. The micro-bondings are done by an automatic machine that uses an ultrasonic technology. The PAs allow the connection between the HS and the sensor on both sides. This connection is made by wire bondings between the sensor AC pads and the PA pads. The PA used on the p-side is smaller (around 6 cm x 2 cm) with respect to the one used on the n-side (around 6 cm x 16 cm) because the sensor AC pads on n-side are placed along the long side of the detector while on the p-side the AC pads are placed along the short side of the sensor.

3.3.2 Gluing procedure

In order to create a forward or a backward module, it is necessary to glue together the three components described previously: sensor, PA and HS. The PA is glued on both the sensor and the HS at the same time in order to provide the connections needed. The assembly procedures are the same for both FW and BW modules.

Before the beginning of the gluing process, an optical inspection of each components is performed, using a microscope, to identify scratches or dirty elements and verify the quality of the wire bonds. The first step of the gluing process consists in the positioning of the HS

and the sensor (both p-side up) on a dedicated metallic structure called gluing jig. The surface of the jig is covered by a teflon layer in order to avoid damages to the sensor. There are 4 different type of jigs: two used for FW modules, n and p-side, and the remaining two for BW modules, n and p-side. Each jig is equipped with a system of micrometer screws that allows the independent motion of the surfaces where the HS and the silicon sensor are positioned (fig. 3.14).

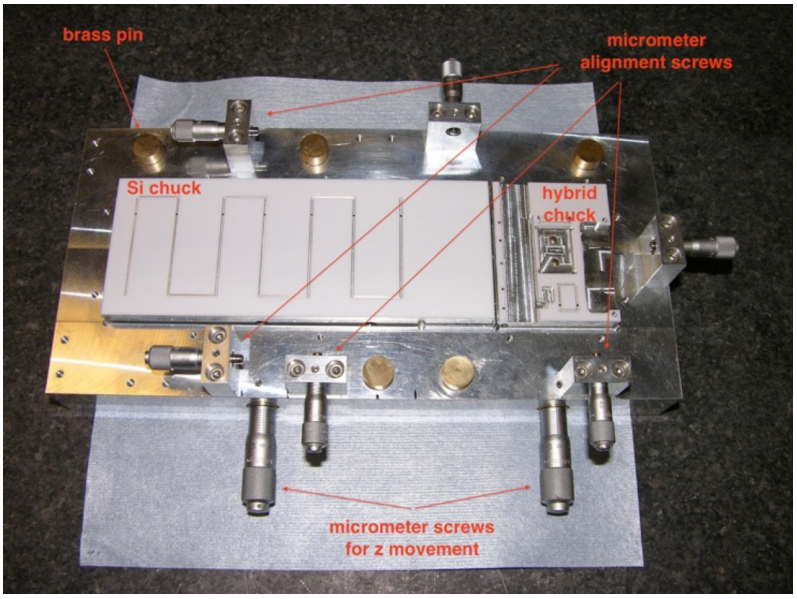

Figure 3.14: Picture of the gluing jig used for backward modules.

The HS is positioned using 2 pins as a guide while the sensor is aligned using two mechanical stops. The hybrid is fixed with 4 screws while the sensor is held by a vacuum system integrated inside the jig. Using the Mitutoyo CMM software, it's possible to align the CMM reference system to the sensor, taking as origin the central point of a reference mark painted on the sensor. Afterwards, the HS has to be aligned to the sensor and its position is adjusted at first by hands and then with the CMM, using two crosses as reference. The alignment is reached if the position of the HS is within 100 μm with respect to its nominal position. All the coordinates and the distances taken during these procedures are stored into a coordinate file. Then the HS and the sensor are moved down in z using the micrometer screws system of the jig, in order to free space for the PA chuck that will be placed over them.

The next step consists in the positioning of the PA on its dedicate chuck (fig. 3.15 left) using pins with a diameter of 0.5 mm. A vacuum system, integrated in the chuck, is activated in order to lock the position of the PA. Then the PA chuck is placed over the

gluing jig resting on 3 brass pins (fig. 3.15 right).

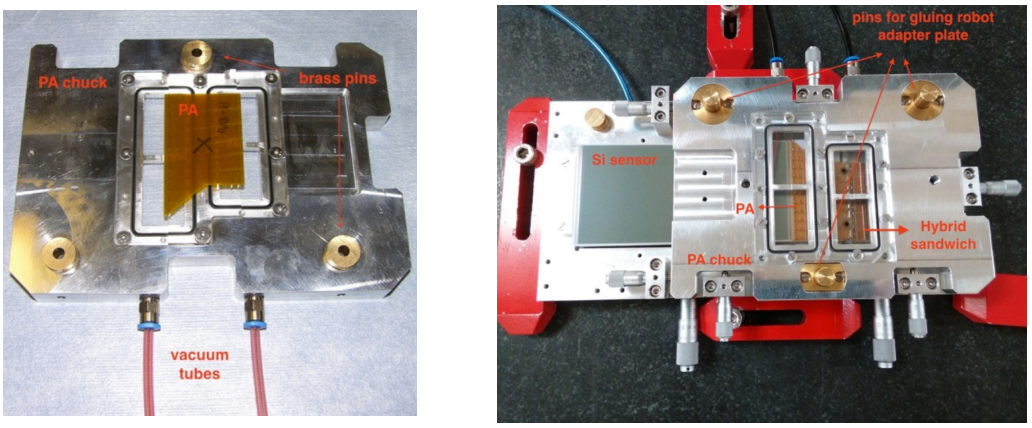

Figure 3.15: Picture of the pitch adapter positioned on chuck (left) and of its positioning over the gluing jig (right).

With the help of three micrometers screws integrated in the jig, the PA is aligned to the system HS + sensor. The maximum distance allowed between the PA and the sensor pads is 150 μm while the maximum distance allowed between the PA and the chip pads is 100 μm. These limit values are chosen in order to make sure that the wire bonds can be performed correctly on the pads. Furthermore, the height of the PA in the regions to be glued is taken. The aim is to reach a planarity condition of those regions within 30μm. If this is not the case, spacers of different thickness can be inserted between the brass button of the gluing jig and the PA chuck. This allows to modify the height of the PA with respect to the HS and to the sensor so that the planarity condition can be reached. This is one of the most challenging step because it directly affects the final result of the whole gluing procedure.

The next step consists in the glue deposition on the PA, that is done by the $I\&J$ Fisnar 750 gluing robot, which consists of a movable arm controlled by LabView programs. The glue (Araldite 2011) is contained in a syringe which is plugged into an compressed air tube (with a pressure of 2.8 bar) that manages the ejection of the glue. The syringe is placed at the end of the robot arm in order to dispense the glue on the PA (see fig. 3.16 right). The PA chuck is embedded on the robot adapter plate using pins as a guide. In order to align the PA to the robot coordinate system, it is possible to move the robot plate using micrometers screws (fig. 3.16 left).

After the deposition of the glue, the PA chuck is positioned back on the gluing jig. The position of a reference cross of the PA is checked in order to verify that the PA didn't

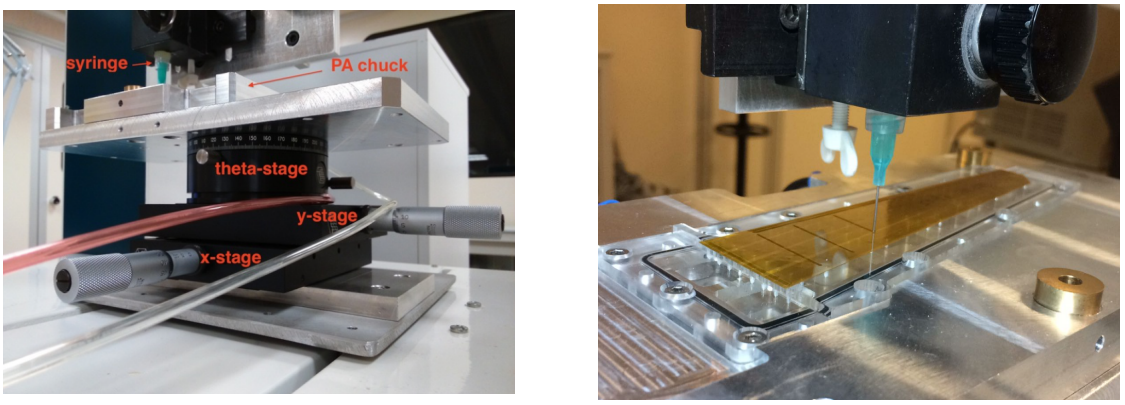

Figure 3.16: On the left the gluing robot structure support is displayed. On the right the glue depositing process is shown.

move during the previous procedure. Using three micrometer screws, the position of the PA chuck is fixed. Then the HS is moved up using a micrometer screw until the glue touches the hybrids. The gluing is considered finished when the glue overflows all over the entire edge of the PA without covering any sensitive areas. The spread of the glue is visible directly with the CMM. The same procedure can be performed in a second moment with the sensor. Once the glue has cured (it takes around 15 hours) the module has to be flipped in order to perform the gluing of the PA on the other side (the n-side). After the end of the gluing process the PA chuck is removed and a detailed optical inspection has done.

At the end, the wire bondings are performed with an automatic machine and the module is considered ready to be electrically tested. A completed module is shown in figure 3.17.

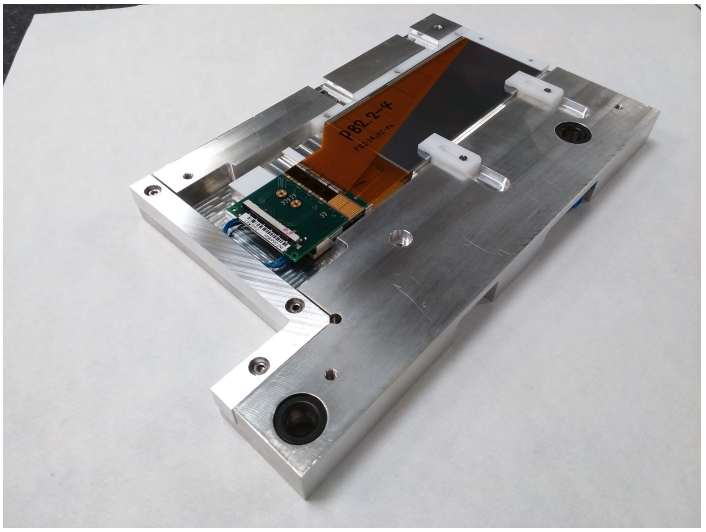

Figure 3.17: Picture of a glued BW module, ready to the shipment.

The gluing procedure is challenging in several ways: first of all good alignment must be ensured, both to obtain the required mechanical precision, but also to allow an efficient wire bonding operation; in addition, the glue must be deposited uniformly and continuously under the PA pads, but must not overflow, to avoid covering the bonds pad; finally enough glue must be applied to obtain a strong glue point. As an example, several studies have been made in order to obtain a better planarity of the regions to be glued, through the use of spacers; in figure 3.18 the height of a PA with respect to the silicon sensor, before and after the introduction of dedicated spacers, is shown.

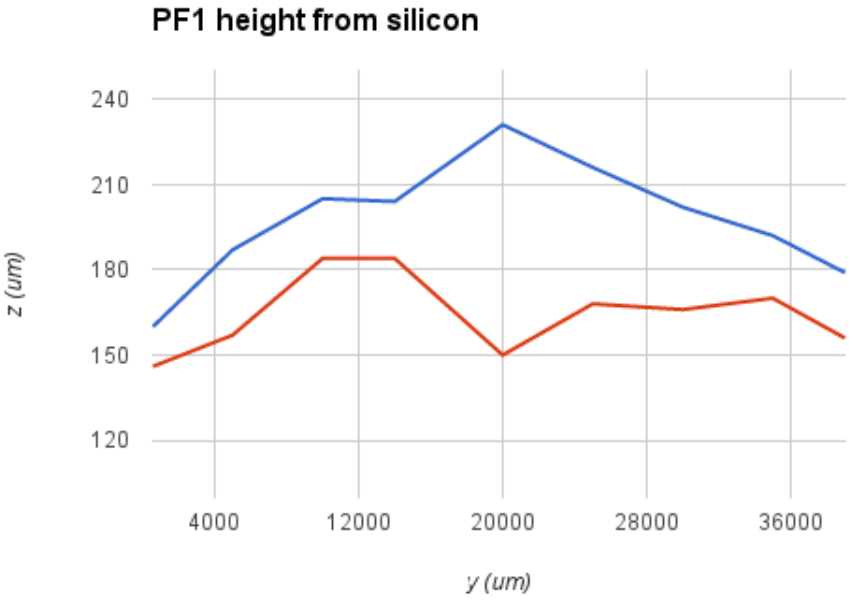

Figure 3.18: Pitch adapter height from silicon sensor with (red line) and without (blue line) the introduction of spacers.

3.3.3 Electrical test

The first electrical tests are done on the sensor detectors and the hybrid sandwiches separately. The sensors used in Pisa are already tested by other groups of the collaboration while the hybrids are tested by ourselves. Once verified that both the HS and the sensor are working correctly, the module is assembled and tested in order to check if all the components are working together in the proper way. During the entire time of the test, the module/hybrid is placed inside a box in order to shield from electrical disturbances and from light. In figure 3.19 the overall scheme for the bias connections is shown.

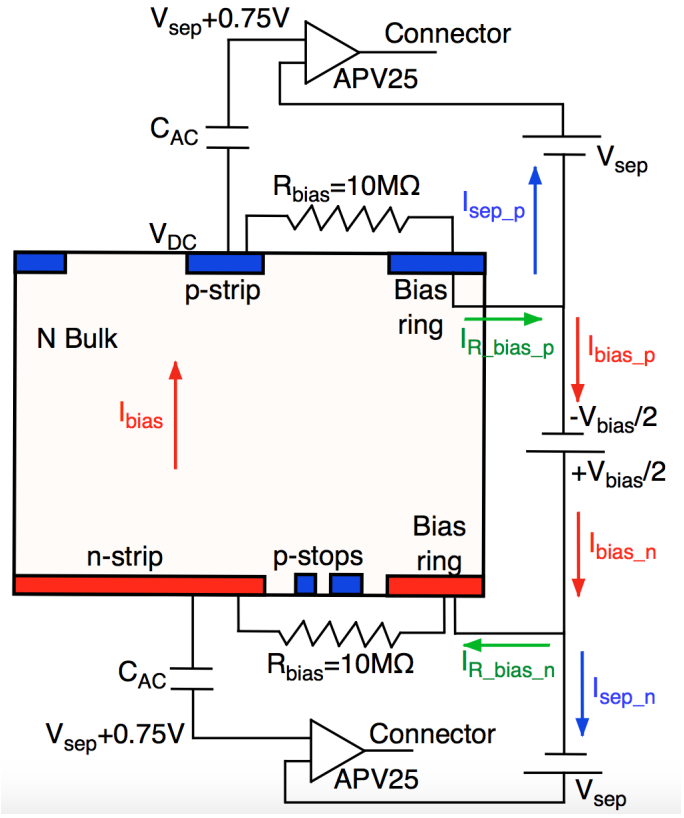

Figure 3.19: Scheme of the connection of the V_{sep} to the sensor. Here the currents directions are shown.

The sensor bias is ∼100 V, and it is normally applied symmetrically with respect to ground. The readout electronics is biased with 1.25 V and 2.5 V voltages referenced to the sensor bias voltage on each side. The reason for this arrangement is to keep the voltage across the coupling capacitor C_{AC} as small as possible, to reduce electrical stress. Additional voltage (V_{sep}) on each side is used to fine tuning the reference of the APV25, allowing the adjustment of the voltage across C_{AC}, which is important, as we will see, when some of the C_{AC} are broken (pinhole). The test stand station is made up of the following components:

- low voltage power supply used to supply the APV25 chips and the readout boards; the voltage is +5 V and -5 V;
- high voltage power supply used to provide the bias voltage of up to 200 V to the sensors;
- VME-based Data aquisition system APVDAQ, controlled using a dedicated LabView interface;

- V_{sep} board used to set the V_{sep} voltage between -5 V and +5 V. This voltage is applied between each n (p) chip power supply and the bias ring of n (p) side (fig. 3.19);

- temperature sensors used to check the temperature of the modules during the tests;

- laser system used to test the response of the strips to the IR light.

In the following, all the steps performed in the electrical test of backward and forward modules are reported in detail:

- Passive measurements: it measures the passive components (capacitance and resistance) of the hybrid sandwich;

- I-V characteristic: it makes a voltage sweep from 0V to 100V - 200V, respectively for forward-backward sensors, in order to measure the leakage current of the sensor;

- Pedestal run: it measures the signal mean value (pedestal) and RMS (noise) of each strip when the bias voltage is applied;

- Internal calibration run: it measures the gain for each channel of the chips injecting a known impulse as input and looking to the output. Furthermore, varying the time of injection, this test is able to measure the whole shape of the output signal.

- V_{sep} scan: for each channel of the chips, it performs a V_{sep} sweep between -5 V and +5 V, measuring at each point noise and gain; this varies the voltage across the C_{AC}. Good channels show negligible change in noise and gain as V_{sep} is varies, while broken capacitors and other defects show characteristic behaviours.

- Laser scan: it measures the number of hits recorded by each strip when a pulsed laser beam irradiates the module; a 1020 nm IR laser is used so that the charge is released uniformly in the sensors thickness, simulating a minimum ionizing particle. Two orthogonal scans are done: one is perpendicular to the n-side strips and the other is perpendicular to the p-side strips, to test the response of all strips.

If the modules pass all the tests, they are sent to the respective collaboration sites.

3.4 Defects characterization

A small fraction of defects (less than 1%) is unavoidable in large productions. The electrical test allows a full characterization of the defect so that the quality of the module is determined and, in some cases, it is possible to apply corrective actions. This section will describe the possible defects found through the electrical tests and the possible cures.

3.4.1 Sensor defects

There are five major type of defects, listed below:

- Open: it consists in a broken strip, chip channel or bond. This means that the information of the defected strips can't be readout. If the defect consists in the broken bond, it is, in principle, possible to perform again the bonding (manually) and fix the problem;
- Short: it consists in the connection of two adjacent strips or bonds, causing a flowing of current. In this case the channel results noisy but the information coming from the defected strip are not lost;
- (Normal) Pinhole: it consist in the breakdown of the oxide layer between the aluminium strip and the strip implant (fig. 3.20).

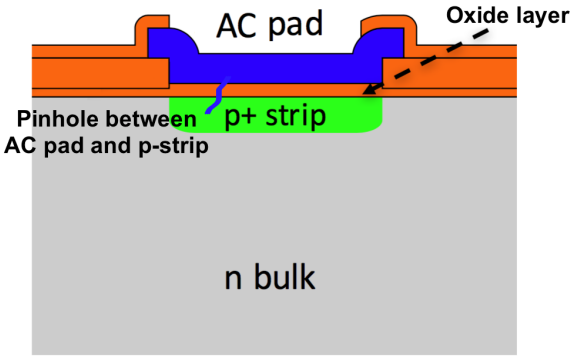

Figure 3.20: Graphic representation of a pinhole defect.

When it occurs, the strip current flows through the defect towards the APV25, instead of the bias resistor R_{bias}. In addition, any voltage difference between the APV25 input and strip implant will result in a large current flowing into or out of

the amplifiers. This can cause a saturation of the amplification channel, making it unusable. Referring to figure 3.19, this current flows through the R_{bias} to the bias ring, and through the V_{sep} battery. Therefore, it contributes to the I_{sep} current of the corresponding side, but not to the bias current I_{bias}. In some cases, the adjustment of $V_{sep} \simeq$ -0.75 V allows to bring to 0 the voltage difference between the strip and the APV25 input, since the chip input voltage normally sits at $\sim$ 0.75 V above the strip voltage, curing the defect.

- Deep pinhole: it consists in the breaking of the oxide layer between the AC aluminium strip and the substrate, as illustrated in figure 3.21. This defect is observed on the p-side.

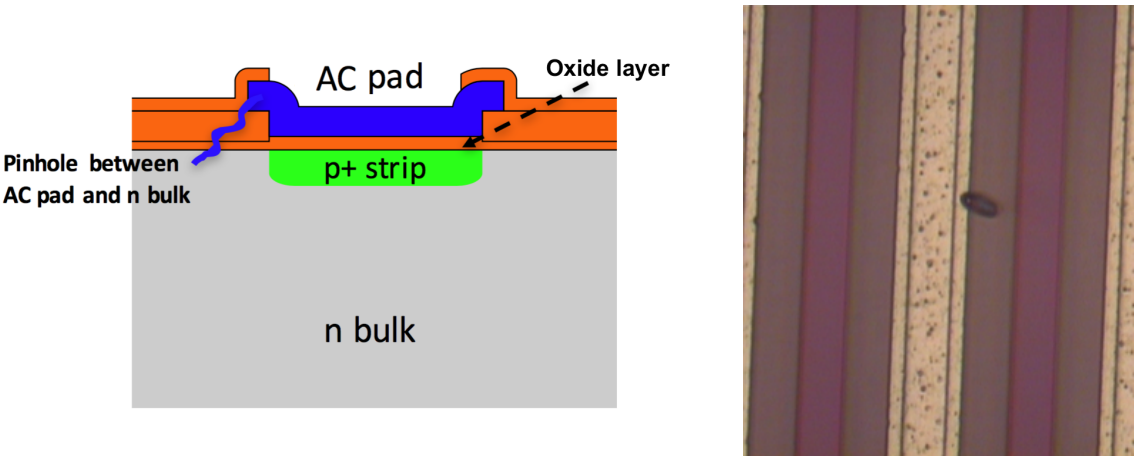

Figure 3.21: Left: graphic representation of the bad pinhole. Right: picture of the deep pinhole found on a module in Pisa.

In this case, a potentially large current coming directly from the bulk can flow into the APV25. Since this current is coming from the bulk, and not from the bias ring, it contributes to both I_{bias} and I_{sep}. This kind of defect can change the behaviour of the whole detector, whereas the normal pinhole changes the behaviour of one channel only.

Since the large bulk current is generated by a point defect on the p-side, it is collected on the n-side only by a few strips corresponding to the defect position. These n strips increase their potential due to the resistive voltage drop on the corresponding R_{bias}.

$$V_{n-strip} = R_{bias} \cdot I_{n-strip} \ , \tag{3.1}$$

where $I_{n-strip}$ depends on I_{bias}. When the strip voltage exceeds the Punch Through (PT) threshold (defined in section 4.3.1), the current start flowing via PT to the adjacent strips or to the bias ring through the bulk, bypassing the bias resistance. In this way, on n-side the high current generated by the bad pinhole can be collected.

- Double pinhole: it consists in the breakdown of the oxide layer between the AC aluminium strip and the edge of the relative strip. This implies that the AC pad is connected with both the strip and the bulk (fig. 3.22).

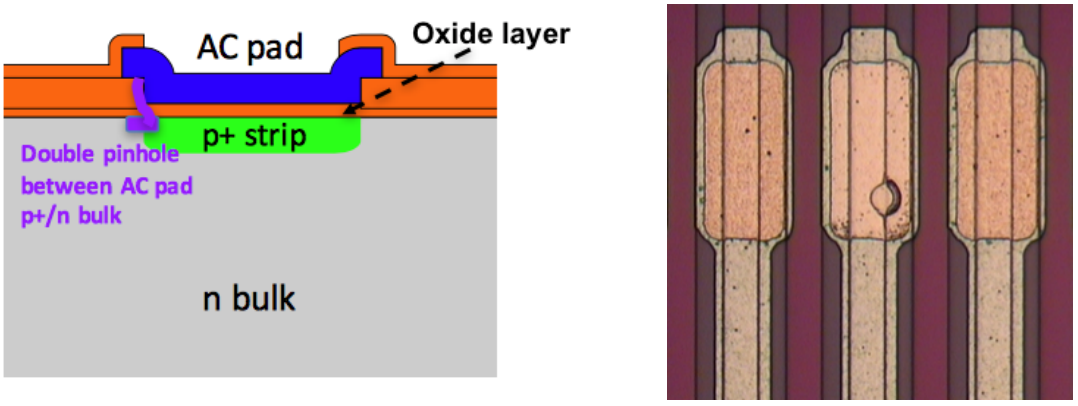

Figure 3.22: Left: graphic representation of the double pinhole. Right: picture of the double pinhole founded on a module in Pisa.

3.4.2 Characterization of defects during the electrical test

The defects described in the previous section can be distinguished by the electrical test since each of them has a distinctive behaviour. The open is identified by high noise and low gain of the channel involved. Furthermore also the adjacent channels result noisy. This apparently counter-intuitive behaviour (n open channel should have less noise), is due to the internal common mode subtraction performed by the APV25. Since the average value of all channels is automatically subtracted, any channel that does not follow the average (such as the open), appears as noisy. The short is identified through the gain of the involved channels, which results $\sim 1/2$ of the expected value. When a short occurs, the same signal flows through the two shorted channels and consequently the gain of both the involved channels is halved.

When a pinhole occurs, the strip involved is identified by a specific gain and noise dependence on V_{sep}. The channel is recovered for V_{sep} around -0.75V, while for V_{sep} below or above that value the gain is significantly reduced, as shown in figure 3.23. This is explained

in terms of the current following into the pre-amplifiers whenever the voltage difference across the C_{AC} is different from zero. During the construction of the modules, it was decided to connect all the known pinholes identified during the sensor tests because they could be recovered, and also because a single disconnected channel causes the adjacent channels to become noisy.

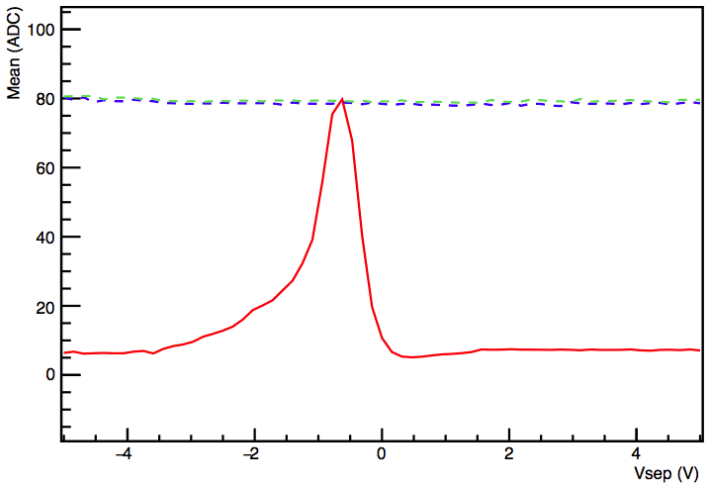

Figure 3.23: Gain (in terms of ADC) of the strip with a pinhole (red line) with respect to the V_{sep} voltage. In green and blue the behaviour of the adjacent strips is shown.

The deep pinhole is identified by a different response to the V_{sep} scan; the gain of the strip is very low until $V_{sep} \simeq +2V$ while for V_{sep} >+2 V gain returns normal (3.24 left). This can be understood by considering that the silicon-oxide interface on the p-side is naturally polarized at a positive voltage of a few volts with respect to the p implants (due to the positive voltage applied on the n-side). As long as the chip input voltage is below this natural voltage, a large injection of electrons from the metal into the bulk occurs. As soon as the chip input voltage exceeds the surface natural voltage, the injection current stops. This explanation is also confirmed by the sensor simulation shown in section 4.4.
This is confirmed by the fact that, for V_{sep} <+2 V, a very high current on the sensor, up to 50 μA is found (fig. 3.24 right). Because of the localized nature of the defect, this current is collected only on a few n-side strips, in correspondence of the position of the defect, that exibit high noise (fig. 3.25). Note that this current is due to the connection of the p-side strip to the pre-amplifier and was therefore not observed during the test performed on the bare sensors. This behaviour will be discussed in detail in the next section.

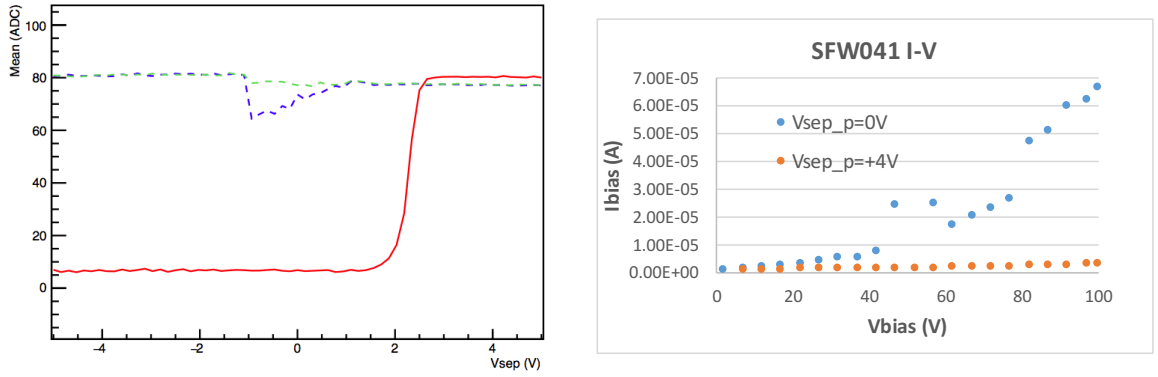

Figure 3.24: Left: gain (in terms of ADC) of the strip with a deep pinhole (red line) with respect to the V_{sep} voltage. In green and blue the behaviour of the adjacent strips is shown. Right: I-V curve of a module for V_{sep}= 0 V and V_{sep}= +4 V, when a deep pinhole occurs.

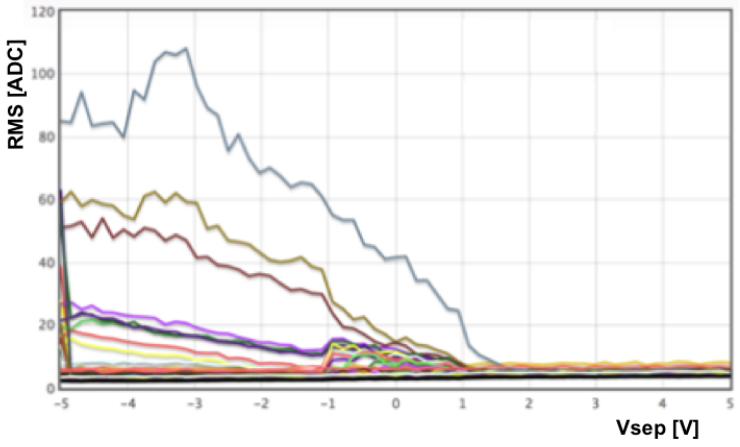

Figure 3.25: Noise of the n-strips in correspondence to the deep pinhole defect on p-side with respect to the V_{sep}. Here the noisy strips are regular for V_{sep} >∼+2 V.

The double pinhole shows a dependence to the V_{sep} voltage, which is a combination of the previous ones. The gain of the channel is normal, although a bit low, only for $V_{sep} \sim V_{pinhole}$, where $V_{pinhole}$ is the natural voltage of the defect (fig. 3.26). Below this value, the deep pinhole bulk current dominates, while above this value the broken AC pinhole current is present, reducing the gain.

Deep and double pinholes, because of their effect on the total leakage current of the sensor, and also because of potentially dangerous evolution with radiation, are disconnected.

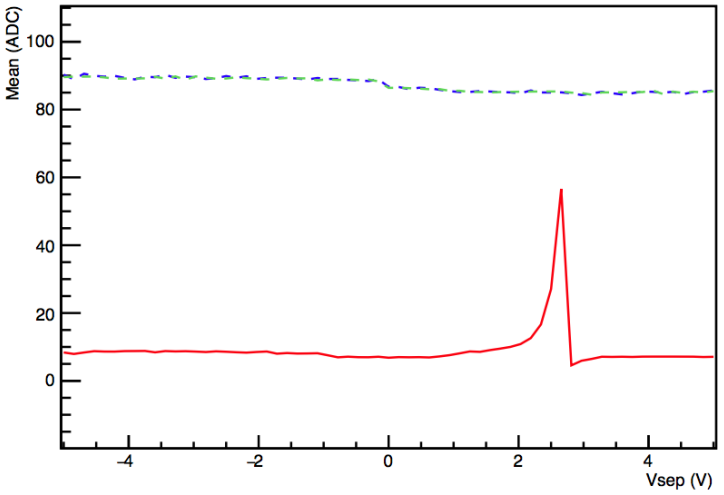

Figure 3.26: Gain (in terms of ADC) of the strip with a double pinhole (red line) with respect to the Vsep voltage. In green and blue the behaviour of the adjacent strips is shown.

3.4.3 Defect statistics at the electrical test

All the performed electrical tests have been analysed with an automated program (called aDefectFinder) to systematically identify and categorize defects. The quality of the produced modules is rather high as shown by the distribution of defective strips depicted in figure 3.27.

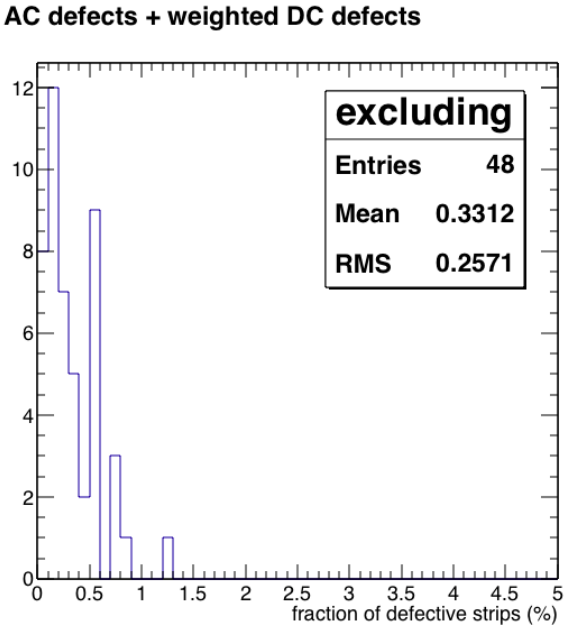

Figure 3.27: Distribution of the fraction of defected strip in a module. It includes both AC and DC defects.

3.4.4 Measurements performed on sensors

Several measurements have been done in order to understand the strange behaviour shown by the various pinhole types. In order to understand the phenomenon, the system has been simulated using a device modelling software (Sentaurus TCAD, as described in the next chapter) connecting the observed behaviour to the physical characteristics of the defect. To perform the measurements, a resistor of 100 $K\Omega$ (R_{sep}) has been added in series to the V_{sep} board so that it's possible to measure the voltage drop across the resistor and to obtain the value of the current (fig. 3.28).

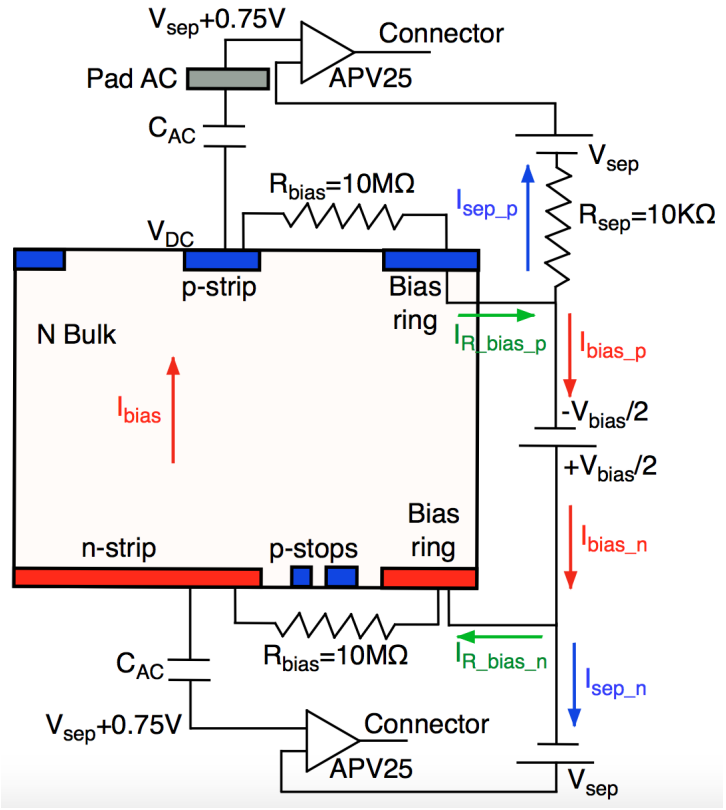

Figure 3.28: Schematic view of the setup used for the measurements where the APV25 chip is represented by an amplifier. Here the R_{sep} is added and the V_{sep} voltage generator is shown.

Using probe points mounted on micro manipulators, it is also possible to contact the AC and DC pads and measure the voltage on specific strips, as shown in figure 3.29. The measurements are performed using an HP4145B semiconductor Parameter Analyser. The purpose of the measurement is to verify the conceptual models and compare the potential on the various circuit points with the simulated values, as discussed in chapter 4.

In the case of a "normal" pinhole, the potentials of the DC and the AC pads should be the

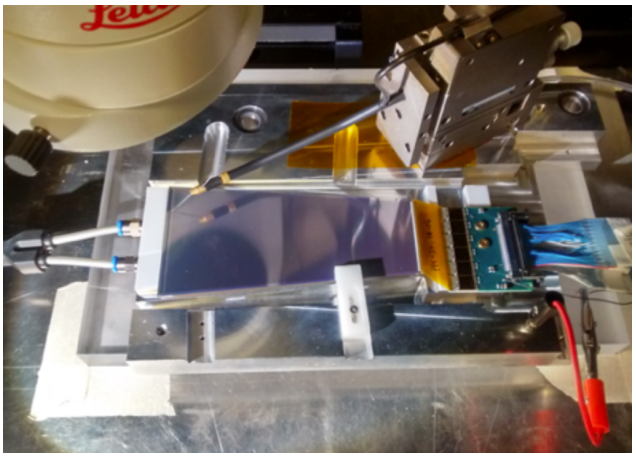

Figure 3.29: Picture of the setup adopted during the measurements performed in the Pisa laboratory. The probe station is fixed with vacuum on the chuck surface of the module and the probe has been contacted with one AC pad.

same because the defect connects directly the two pads (fig. 3.30 left). For a deep pinhole, the connection between the bulk and the APV25 input causes a flow of current towards the chip, changing the AC pad potential (fig. 3.30 right) because of the series resistance of the connection.

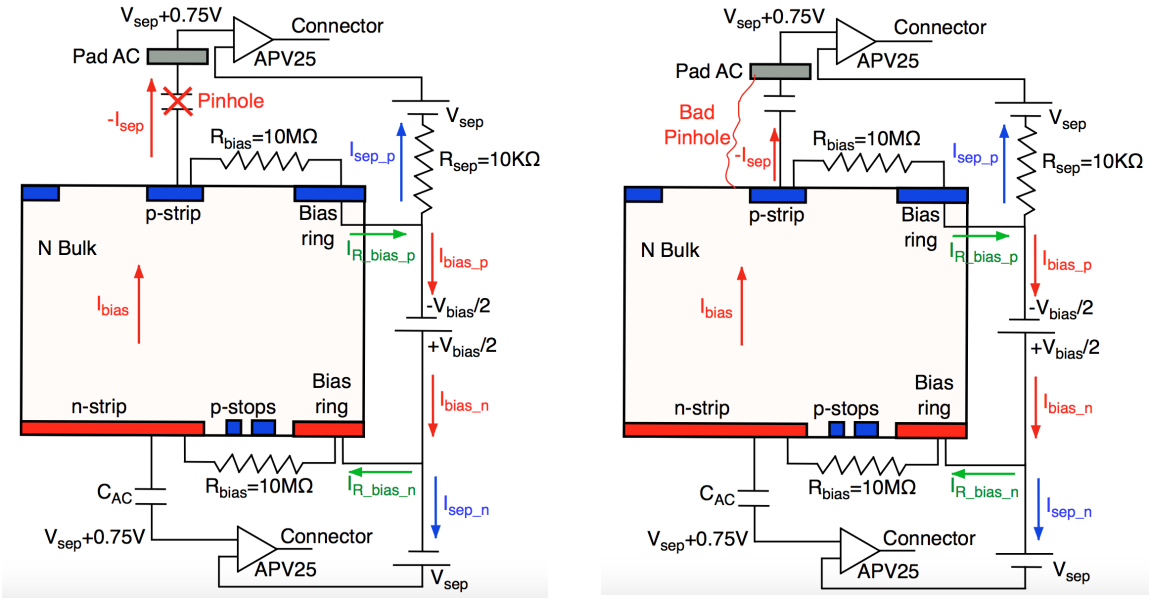

Figure 3.30: Schematic view of the setup used for the measurements when a pinhole occurs (left) and a bad pinhole occurs (right).

For this reason, in some cases, the involved p-strip was disconnected from the APV25 in order to verify our model. After the disconnection, we observed that the bias current I_{bias} becomes normal and the module seems cured. The DC pad relative to the defected strip

is contacted and its voltage (V_{DC}) has been measured. The V_{DC} voltage results equal to the bias voltage applied to that side (as expected). After that check, the AC pad is contacted and its voltage measured while varying the bias voltage applied to the n-side. This measurement is performed setting the semiconductor Parameter Analyser in current mode, thus forcing zero current and measuring the voltage.

The measurements show that the potential of the AC strip (V_{AC}), that correspond to the natural voltage of the pinhole ($V_{pinhole}$), is ∼4 V with the bias voltage V_{bias}=100 V. Furthermore V_{AC} follows V_{bias}, proving that the pinhole is directly connected to the bulk (fig. 3.31).

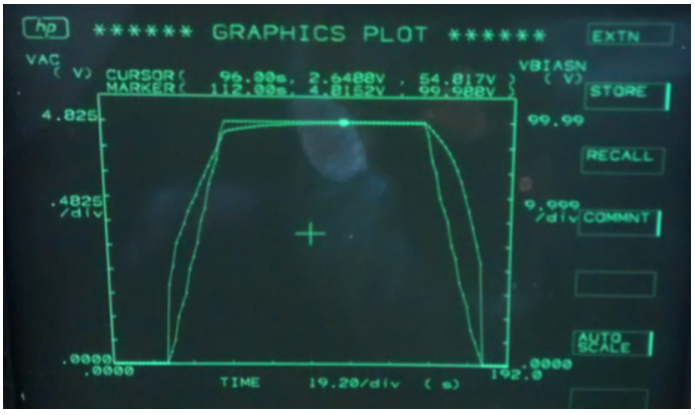

Figure 3.31: Measurement result showing the V_{AC} (rounded shape, left scale) and the V_{bias} (square shape, right scale) changing in time. Here the V_{AC} follows the bias voltage, meaning that the bad pinhole made a connection between the bulk and the AC pad

An additional check is provided by the I-V curve of the AC pad; the current is measured for values of V_{AC} between -4 V and +6 V (fig. 3.32).

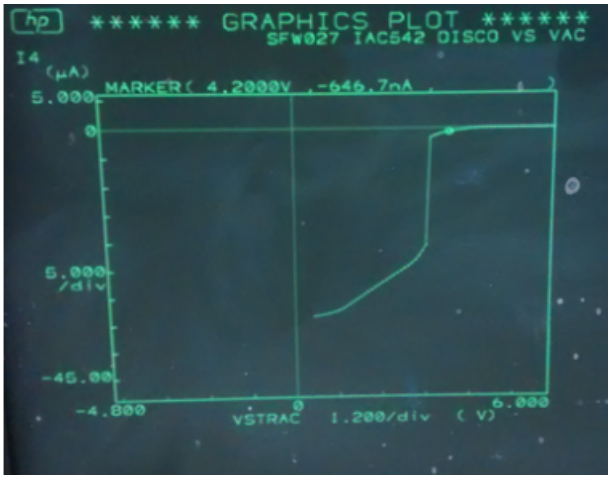

Figure 3.32: Measurement result showing the I_{sep} with respect to V_{AC}. Here the I_{sep} goes to 0 when the $V_{AC} > V_{pinhole}$ that is around 3.5 V.

In this case, the measurement is performed in voltage mode, thus forcing a specified voltage and measuring the current. The V_{AC} voltage is the same of the input voltage of the APV25, which consists in the V_{sep} with a difference of ∼0.75 V. The I-V curve shows a high current for $V_{AC} < V_{pinhole}$ which corresponds to a low APV25 gain. This shape explains the behaviour of the deep pinhole current with respect to V_{sep} that comes out from the V_{sep} scan test (fig. 3.21). The exact value of $V_{pinhole}$ varies from case to case. Other measurements have been performed in order to understand the behaviour of the double pinhole. The AC strip has been contacted with a probe and the dependence of the I_{sep} with respect to the V_{AC} has been measured. The result is shown in figure 3.33. The explanation of this particular shape is still under investigation and it has not been reproduced with the computer simulation.

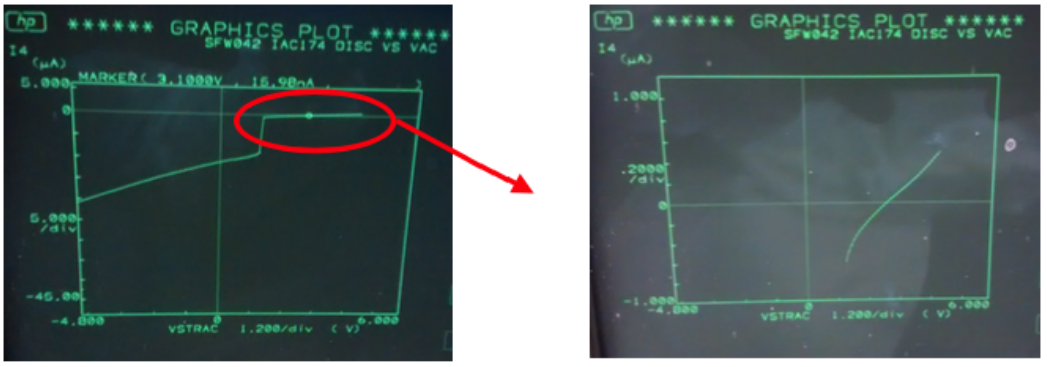

Figure 3.33: On the left, the plot of the current flowing through the APV25 chips with respect to the potential of the AC pad is reported. On the right, the zoomed plot in the interesting region is shown.

In this chapter, the Belle II SVD is described more in detail and particular attention is given to the forward and backward modules assembled in the Pisa laboratory. The gluing procedures are explained together with the electrical tests, which indicates some issues caused by unknown defects. Thus, not standard measurements have been performed in order to understand the defects electrical behaviour. A computer simulation of the electrical effects produced by the deep pinhole defect has been performed and it is described in the next chapter. The simulation is an helpful tool used to understand better the defect behaviour and to confirm the measurement results.

Chapter 4

Silicon sensor simulation using Sentaurus software

This chapter presents a detailed study of the electrical behaviour of the SVD silicon detectors I personally performed with Synopsys Sentaurus Technology Computer Aided Design (TCAD) [34], which is a standard software used to design and simulate semiconductor devices.
The purpose of this sensor simulation was to reproduce the behaviour of the new defect discovered during the electrical tests (see section 3.4.2). Initially the structure of the sensor was implemented and validated; the validation was performed comparing the simulated results with measurements of basic quantities. The defect was then introduced in the sensor, comparing its simulated behaviour with the measurement shown in chapter 3. This simulation was very helpful to confirm that the interpretation of the new defect discovered was the correct one.

4.1 Simulation framework

The Synopsys Sentaurus simulation framework utilizes the standard finite element analysis (FEA) scheme of creating a mesh-like grid structure and then solving equations at each mesh point to calculate physical properties. The TCAD simulation tools solve fundamental, physical and partial differential equations that model the device, performing numerical calculations of voltages, currents and charges. The fundamental equations include the Poisson's equation, the current continuity equation and the drift-diffusion equation for holes

and electrons. The recombination and generation models implemented in the packages use concentration and lifetime dependent Shockley- Read-Hall (SRH), Auger and radiative recombination models, as well as concentration and field dependent mobility models. The simulation packages enable the additional generation of charge carriers via the impact ionization [34]. These models are used directly in the solution of the device equations in a self-consistent manner.

The semiconductor device geometry is reproduced through a non-uniform grid (mesh). For each node of the grid, the carrier concentration, current densities, electric field, generation and recombination rates, and so on are computed. The electrodes are simulated as a region on which boundary conditions (voltage, current and resistance) are imposed. The device simulator solves the Poisson equation and the carrier continuity equation (if necessary, also other equations) in order to extract the current value at the contacts. The detailed physical approach gives to TCAD simulation a good predictive accuracy. The simulation process is described by a command file that contains the physical models used, the boundary conditions set on the contacts and the goals[1] of the simulation itself.

The simulation work can be summarised in 3 fundamental steps:

- Creation of the device structure and definition of the mesh;
- Simulation of the electrical behaviour of sensors and validation check of the structure;
- Deep pinhole simulation and consecutive analysis of the results.

4.2 Device structure and mesh

The first step is to reproduce in detail the device geometry [28]. To study the properties on both sides of the double sided strip sensors it has been decided to make two different 2-D simulations instead of a 3-D one, due to lack of computing power and time. Two sections of the sensor are considered, as shown schematically in figure 4.1 for the section used to reproduce the n-side. In this case, the structure contains, on one side, several n-strip head with the p-stop implant in between and, on the other side, one single p-strip. The p-side structure, in a similar way contains several p-strips head on one side and one single n-strip on the opposite side. Furthermore, for each simulation only a small part of the

[1] Sentaurus Device starts from an initial condition and gradually changes that condition until the specified voltage or current goal is reached.

whole sensor has been simulated. The central part of a sensor is removed (the structure includes only several strips) as well as the guard ring structures at the two edges, as shown in figures 4.4 and 4.6, so that the dimensions of the simulated device is reduced to 985 μm x 300 μm. Even if the simulation is 2-D, the depth can be reproduced using the Area Factor (AF) parameter, available in the simulation software (by default it is assumed 1 μm). This AF specifies also a multiplier for currents and charges.

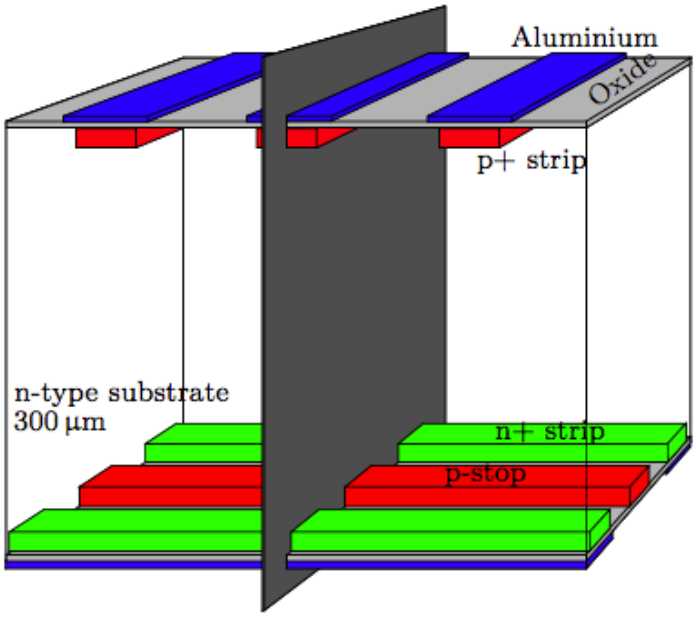

Figure 4.1: Representation of the section of a sensor; this division represents the n-side. The section created with an orthogonal plane represent the p-side.

The structure of the sensor is defined taking into account the dimensions, the positions, the contacts and the materials of all the components of the detector. The doping profiles and the relative refinements are described by Gaussian profiles with standard values for this kind of implants.

For both simulations, the bias resistance, that provide the bias voltage to the strips, is implemented using a "bias contact" placed on the strip implants (figures 4.3, 4.5) with a contact resistance of 10 $M\Omega$ (corresponding to R_{bias}).

The resistances are simulated as resistors in series to the metal contact (contact resistance) with an inner and an outer voltage as shown in figure 4.2.

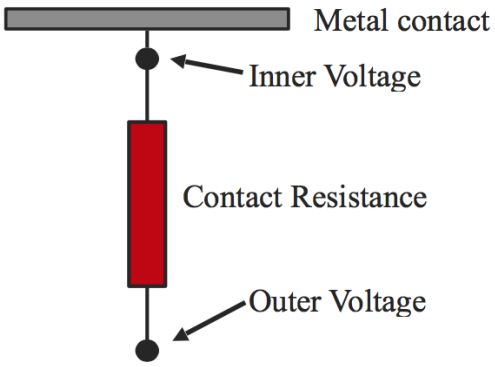

Figure 4.2: Contact resistance representation through the simulation software. For the "bias contact", the contact resistance is 10 MΩ.

A schematic representation of the structure implemented for the p-side is reported in figure 4.3. The simulated structure contains 35 p-strips with pitch 25 μm as shown in figure 4.4.

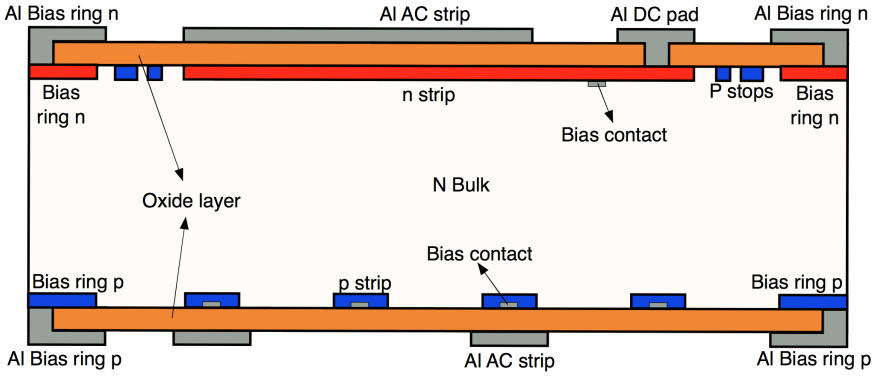

Figure 4.3: Schematic geometry of a section of the sensor. Here the p-side is represented.

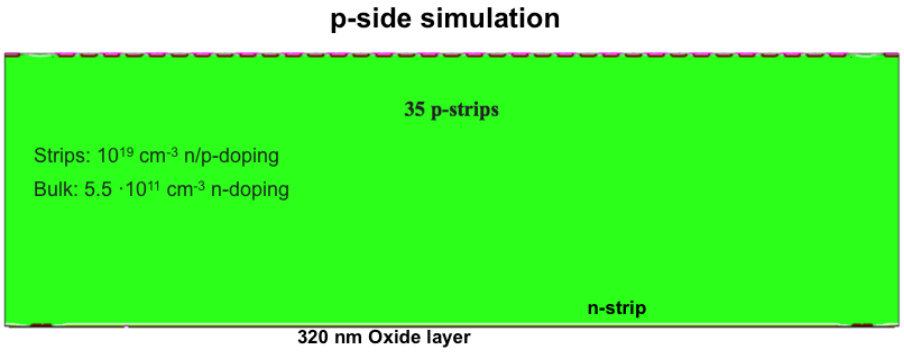

Figure 4.4: Simulation result of the p-side sensor structure.

A schematic representation of the structure for the n-side section of the sensor is reported in figure 4.5. The simulated structure contains 9 n-strips with pitch 120 μm as shown in figure 4.6.

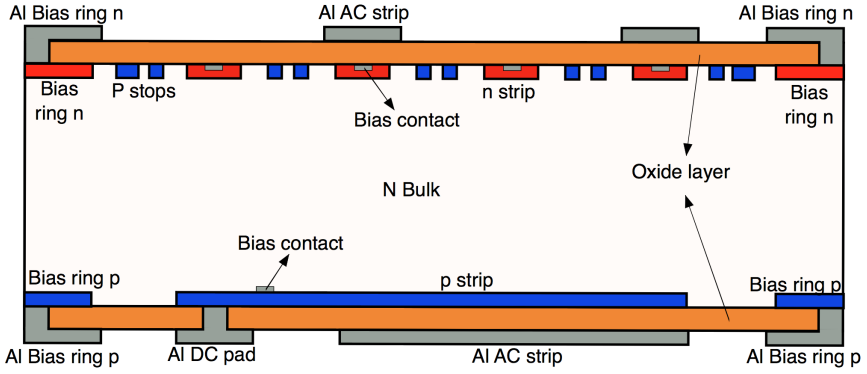

Figure 4.5: Schematic geometry of a section of the sensor. Here the n-side is represented.

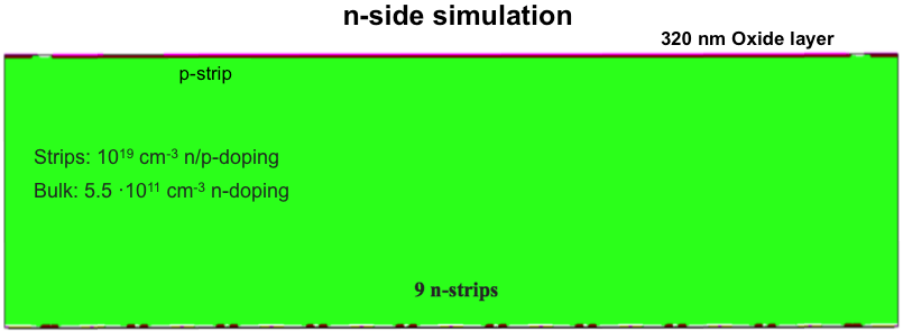

Figure 4.6: Simulation result of the n-side sensor structure.

The next step is to create a mesh, that means divide the geometrical regions into polygons (in this case triangles) which vertices are used in the calculation of the physics quantities. Therefore, if the mesh is large the results are less detailed but at the same time the computing time decreases. For this reason it's necessary to choose a compromise depending on the type of simulation. Moreover there are some regions of the sensor more important than others, thus it's necessary to have a better precision on the physical quantities in these regions. For example, the areas around separation surfaces between different materials, contacts and doping profiles need a smaller mesh, which implies to use more calculating points. The mesh structure is the same for both the simulations. An example of a mesh structure created with Sentaurus Software is displayed in figure 4.7.

The whole mesh structure is saved into a file together with the previous information re-

garding the geometry and the doping profiles. This file will be used later as input to the simulation scripts.

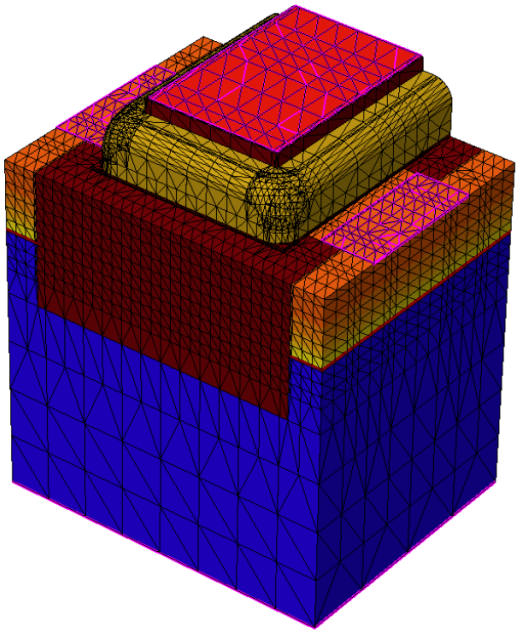

Figure 4.7: Example of the mesh provided by Sentaurus on a transistor device.

4.3 Validation of simulation process

The second step of the study is the validation of the simulation process on the implemented structures. This is done comparing the results of the simulation with the corresponding electrical measurements performed on real device. In particular, the simulation of the I-V curve and the punch-through effect on the n-side (see next section) is compared with the measurements performed by collaborators in Trieste during sensor characterization. These are both relevant aspects for the interpretation of the new defects discovered on the assembled modules. Some free parameters of the models used in the simulation, relevant for this study, (i.e. minority carrier lifetime, fixed oxide charge) have been tuned in this validation step in order to get a good agreement with the measurements.

The minority carrier lifetime τ, linked to the generation and recombination effects, is tuned to reproduce the low values of the strip leakage current measured in our sensors. The following equation [31] is used:

$$\tau = \frac{q \cdot N \cdot A \cdot d}{I_{leak}} \tag{4.1}$$

where τ is the generation and recombination time of e-h, q is the elementary electric charge, N= 1.45 $\cdot 10^{10}$ cm^{-3} is the intrinsic carrier concentration of our sensors, A=1.8 cm^{-2} is the area of a strip, d=300 μm is the thickness of the depleted region and $I_{leak} \simeq$ 1 nA is the typical leakage current (measured in our sensors).

Typical values of I_{leak}=1 nA translates to a carrier lifetime of about 1 ms, three order of magnitude higher w.r.t. the default τ values used for commercial devices. The leakage current collected by the n and the p-side strips, is extracted by applying a reverse bias voltage ranging from 0 V to 100 V for both the simulated structures. The results of this simulation (fig. 4.8) show a good agreement among the simulated strip current and a typical value of ∼1 nA/strip measured on the sensors.

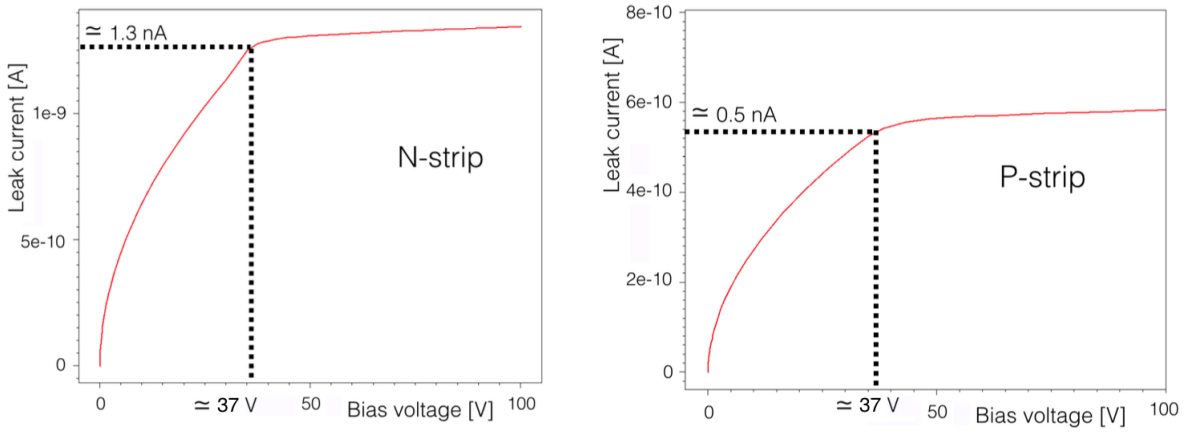

Figure 4.8: I-V curve of n-side (left) and p-side (right). From the plots, the leakage currents and the full depletion voltage values are pointed out.

Furthermore it is useful to compare the values of the full depletion voltage V_{FD}. This value corresponds to the bias voltage necessary to deplete the entire sensor (300 μm thick). The measured total depletion voltage V_{DF} in our sensors is about 35V and it can be also compared with the V_{FD} from the simulated I-V curve. In fact, in the simulated structure the leakage current is dominated by the generation in the bulk (i.e. current initially scaling linearly with depleted thickness d, then with $\sqrt{V_{bias}}$), and the maximum current is reached at the total depletion voltage. From figure 4.8 $V_{FD} \simeq$ 37 V is obtained for both p and n-side devices. The full depletion voltage can also be calculated [35], [31] with the following equation:

$$V_{FD} = \frac{d^2}{2 \cdot \varepsilon_0 \varepsilon_{Si} \cdot \mu_e \cdot \rho} \tag{4.2}$$

where ε_0 is the electric constant, ε_{Si} is the relative permittivity of silicon, μ_e is the electron mobility, d is the thickness of the sensor and $\rho = 1/(\mu_e \cdot q \cdot N)$ is the resistivity, expressed in term of N, the doping concentration of the n-bulk, and the elementary charge q. Using these values: $\varepsilon_{Si} = 11.7$, $\mu_e = 1335\ cm^2/V \cdot s$ and N = $5.5{\cdot}10^{11} cm^{-3}$ (resistivity $\rho = 8.5\ K\Omega \cdot cm$), the full depleted voltage is V_{FD}= 37.8 V.

4.3.1 Punch through effect

The Punch Through (PT) effect consists in a large current flux through a p-n-p sandwich structure (or n-p-n), when the voltage difference among the two external implants is above a certain threshold, called punch-through voltage (V_{PT}). Applying a voltage across the sandwich structure will cause one of the junctions to become reversed biased. As the voltage increases, the depletion layer of the reverse biased junction grows. The voltage at which the central implanted region is fully depleted, and the space charge regions of the p-doped areas touch, is the punch-through voltage V_{PT}. Once the punch-through voltage is reached, majority charge carriers from one p-doped area will be injected into the other p-region through drift and diffusion across the central n-region totally depleted. This will lead to an exponential rise in the current with respect to the applied voltage. The PT mechanism can occur also in silicon-strip sensors. For the Belle II strip detectors, on the p-side the punch through can occur between two adjacent p-strips and between a p-strip head and the p-side bias ring, where the n-bulk represents the n-doped region of the p-n-p sandwich structure (fig. 4.9).

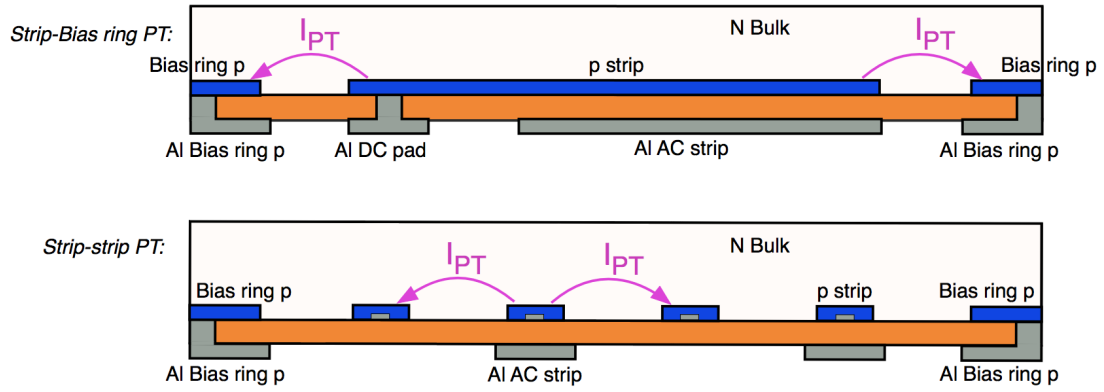

Figure 4.9: Schematic view of the p-side PT effect between a strip and the bias ring (top) and between two adjacent strips (bottom).

Also on the n-side the punch through can happen among two n adjacent strips, with the p-stop implants in between that creates the potential barrier among them, and it can also happen between the head of the n-strip and the n-bias ring, having again the p-stop implant between the two n-implants (figure 4.10).

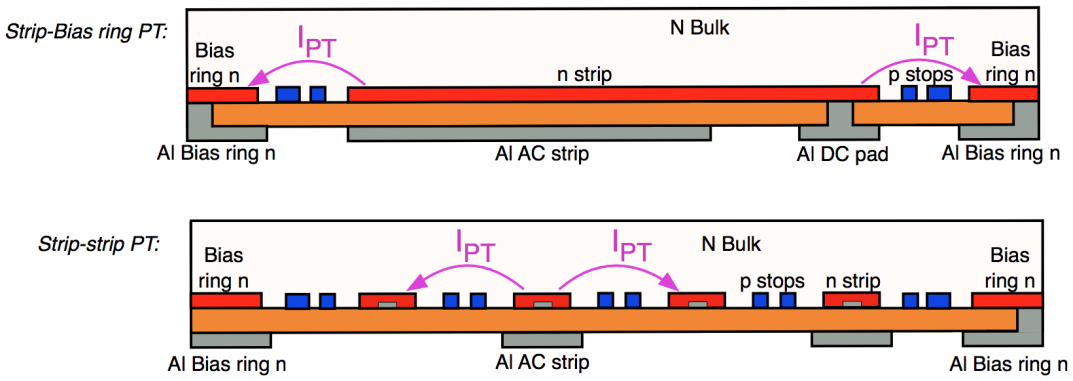

Figure 4.10: Schematic view of the n-side PT effect between a strip and the bias ring (top) and between two adjacent strips (bottom).

An example of the simulated punch through effects on the n-side is shown in figure 4.11.

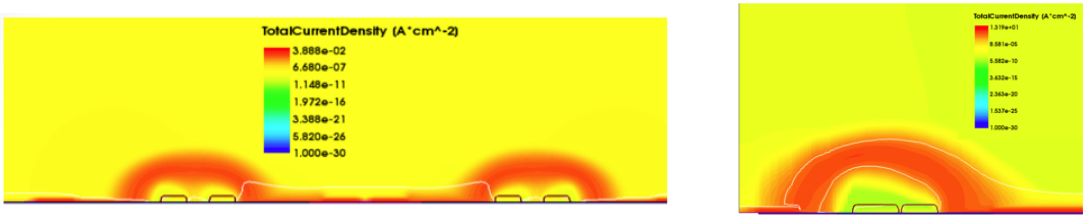

Figure 4.11: Simulated n-side PT effect between two adjacent strips (left) and between a strip and the bias ring (right). Simulation obtained with V_{bias}= 100 V and a voltage difference among adjacent n implants of 25 V.

For the mechanism explained above, on the p-side the punch through voltage V_{PT} increases with the distance between the two p-implants; it also depends on the n-bulk doping concentration and on the oxide charge concentration (Q_{ox}), since the latter modulates the surface electron accumulation layer in the bulk, also relevant to determine the extension of the charge space region between the two p-implants. On the n-side the presence of an electron accumulation layer, modulated by the positive charge trapped in the silicon oxide (Q_{ox}), extends the dimensions of the n-electrodes with respect to the geometrical dimension of the implanted strip. For this reason the effective distance among two n-implants, and consequently the punch through voltage among them, depends both on the geometry of the p-stop implants and on the oxide charge concentration.

The aim of the simulation is to reproduce the punch through effect on the n-side in order to compare the results with the ones measured on the Belle II sensors by the Trieste collaborators. The simulation of this effect is really useful because it is also used later to explain one aspect of the deep pinhole behaviour (see section 3.4). The Belle II group in Trieste performed the measurement as described below (fig. 4.12) and the results are shown in figure 4.13.

- The sensor was fully depleted ($V_{FD} \simeq$ 40 V) contacting the bias rings on the two sides with V_{bias}^{p-side}= -100 V and V_{bias}^{n-side}= 0 V;
- They contacted a DC strip on n-side varying its voltage with a sweep from 0 to -25 V;
- They measured the current on the contacted strip together with the voltage of the adjacent DC strips;

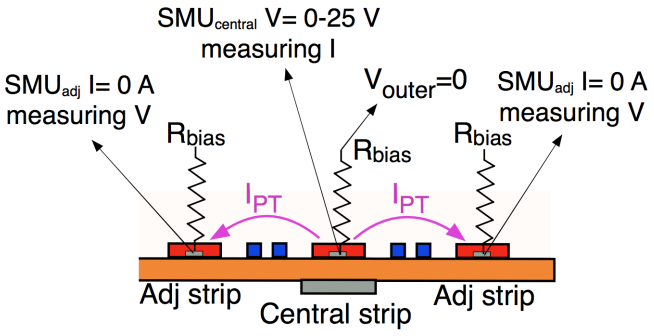

Figure 4.12: Schematic view of the setup used in Trieste for the punch through measurement on n-side. The sensor was fully depleted with 100 V bias applied through the bias rings of the n and p-side (not shown in the picture).

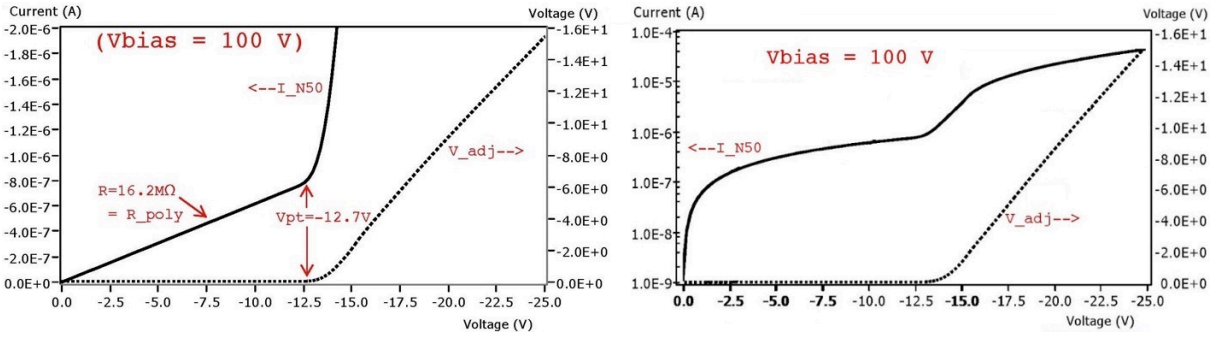

Figure 4.13: I-V punch through curve measured in Trieste, on a n-side strip. The left plot shows the current of the a n-strip (left axis) and the voltage of the adjacent strip (right axis) as a function of the voltage applied on the n-strip. Adjacent n-strips and bias ring-n were set to 0 V and the sensor was fully depleted (V_{bias}^{p-side} = -100 V). On the right, the same plot in log scale is reported, showing that the strip current after punch through activation is up to ~50 μA.

The measurement results include the contribution of both the strip-bias ring and the strip-strip PT but, with the 2D simulation implemented, it is not possible to have both effects present in the same structure (as explained above). For this reason the two PT effects are reproduced separately in the simulation. The values extracted from the simulation,

in order to make a comparison with the punch through measured curve, are V_{PT} and the dynamic resistance R_{PT}, which is the slope of the punch through I-V curve. From the measurements (fig. 4.13 as reference) V_{PT} $\simeq$13 V and R_{PT} $\simeq$200 KΩ where R_{PT} comes from the slope of the curve beyond the V_{PT} (at voltages >16 V). The shape of the measured punch through curve in 4.13 can be interpreted in the following way:

- the punch through voltage of the central strip is $V_{PT} \sim 13$ V (here the absolute value of the voltage is considered);
- before the punch though is reached ($V_{strip} < 13$ V) the current flows from the central strip to the bias ring-n through the bias resistor, as can be seen from the constant slope of the I-V measured curve, that matches the polysilcon bias resistance;
- above $V_{strip} > 13$ V the strip is in punch through with other n-implants and the dynamic resistance R_{PT}, slope of the I-V curve, is smaller of the bias resistance, ~ 2 $M\Omega$ at about 14 V and $\sim$200 KΩ at higher voltages, indicating that the current path is not only through the bias resistor and that the PT mechanism is in place. The strip is in PT with the adjacent strips, since their voltage (V_{adj}) also start to increase, being $V_{adj} = R_{bias} \cdot I_{PTadj}$. The current collected by the adjacent strip I_{PTadj} can be calculated from its measured voltage. For example at V_{strip}= 15 V the total PT current of the central strip is $I_{PT} \simeq 2$ μA and, from the measured voltage of $V_{adj} \simeq 2$ V the collected current on each adjacent strip is only I_{PTadj}= 0.125 μA. Then, either the punch through extends to about 50 adjacent strips (very unlikely case) or the rest of the PT current is flowing from the central strip to the bias ring via PT through the n-bulk, and not through the bias resistors. This measurement cannot distinguishes among these two contributions since, in any case, the current flowing via PT to the adjacent strips is finally collected via their bias resistors on the bias ring. Thus, the interpretation is that the strip is simultaneously in PT with the adjacent strips and the bias ring.

Strip-strip punch through

In order to simulate the PT effect between two adjacent n-strips, the structure in figure 4.5 is used as reference and, the same experimental setup used in the measurements done in Trieste is adopted (fig. 4.12). With the device fully depleted (V_{bias}^{p-side}= -100 V and V_{bias}^{n-side}= 0 V), the potential of the central strip has been varied from 0 V to -25 V, setting

to the desired values the inner voltage of the bias contact placed on the strip. Since the simulation is 2D, the length of the strips are reproduced by the area factor parameter, used in the simulation code to scale the resulting currents and charges. For this simulation the area factor adopted is the length of the real n-strip (∼6 cm). The results (fig. 4.14) show $V_{PT} \simeq 13V$, in agreement with the measurements if $Q_{ox} = 10^{12} cm^{-2}$ is considered.

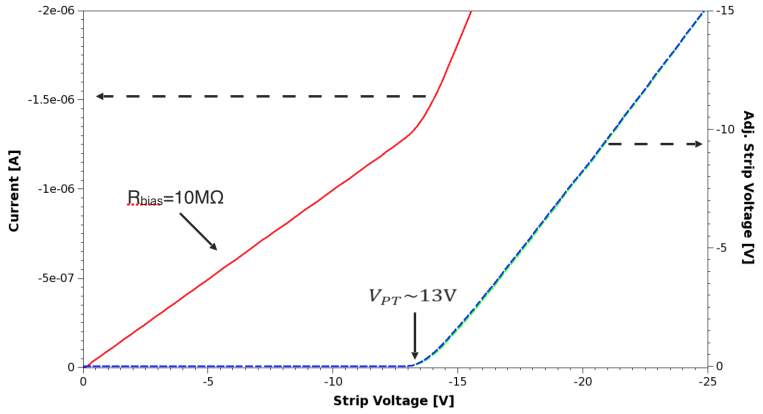

Figure 4.14: Result of the strip-strip PT simulation on n-side. On left y axis there is the current flowing in the contacted strip, on right y axis there is the voltage of the adjacent strips and on x axis there is the voltage of the contacted strip. In the simulation the bias resistor was set to the nominal value of 10 MΩ, while in the measured sensor the bias resistor had an higher value.

A large Q_{ox} cause a broadening of the built-in depleted region of the strips that allows the current to pass easier between adjacent strips (figure 4.15).

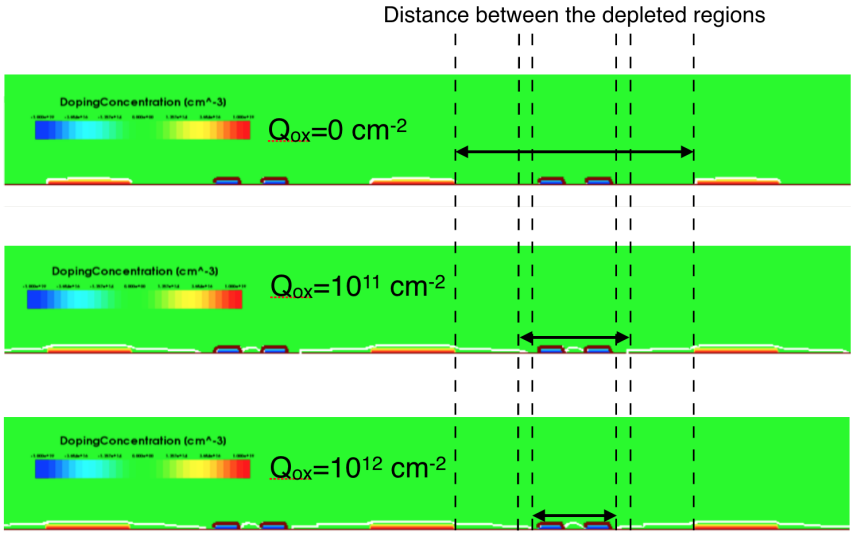

Figure 4.15: Oxide charge effect on the depletion regions, which are represented by the white lines. The arrows indicate the distances between the depleted regions of the strips. Simulation obtained with V_{bias}= 100 V.

Indeed the PT is very sensitive to the distance between the implants. This means that also the broadening of the implants themselves plays an important role. The simulation shows that, a difference of about 0.2 μm on the implants width causes a ΔV_{PT} $\simeq$0.5 V (fig. 4.16).

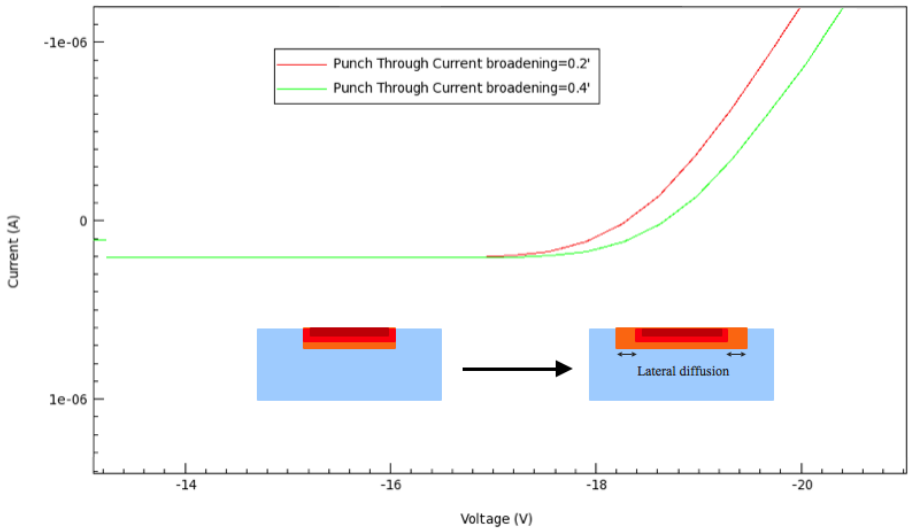

Figure 4.16: Effect of the broadening on V_{PT}. The red line correspond to a lateral diffusion of the implant of 0.2 μm, while the green one corresponds to a lateral diffusion of 0.4 μm.

Since the PT effect is very sensitive to various parameters (Q_{ox}, effective width of the implants) that are not completely known, in the following a value of Q_{ox} of 10^{12} cm^{-2} is used, which is higher than the real oxide charge in our sensors, but give us the better match with the measured V_{PT}.

Strip-bias ring punch through on n-side

In order to study the strip-bias ring PT effect, the structure in figure 4.3 is used as reference, where the head of the long n-strip is close to the n-side bias ring (30 μm apart), with the p-stops in between. For this simulation we kept $Q_{ox} = 10^{12}$ cm^{-2}, and the width of the strip (15 μm) is introduced setting the area factor at 15 μm. In order to simulate the strip-bias ring PT effect, same experimental setup as strip-strip PT is used (figure 4.17).

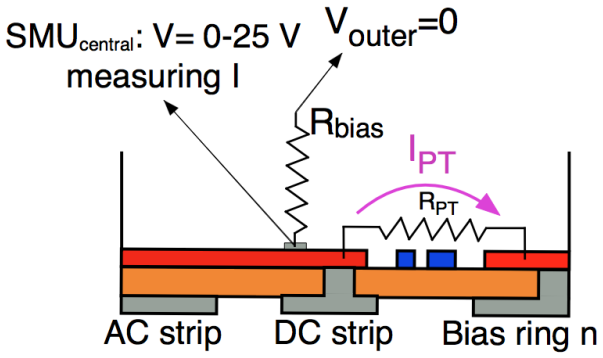

Figure 4.17: Schematic view of the setup used in Trieste for the PT measurement on n-side. The sensor was fully bias to 100 V through the bias rings of the n and p-side (not shown in the picture).

With the device fully depleted (V_{bias}^{p-side}= -100 V, V_{bias}^{n-side}= 0 V) the voltage on the n-strip implant (inner voltage of the bias contact placed on the strip) has been varied from 0 V to -35 V. The simulated I-V curve is reported in figure 4.18, where the various contribution to the total strip current (here called DC pad current) are separately shown.

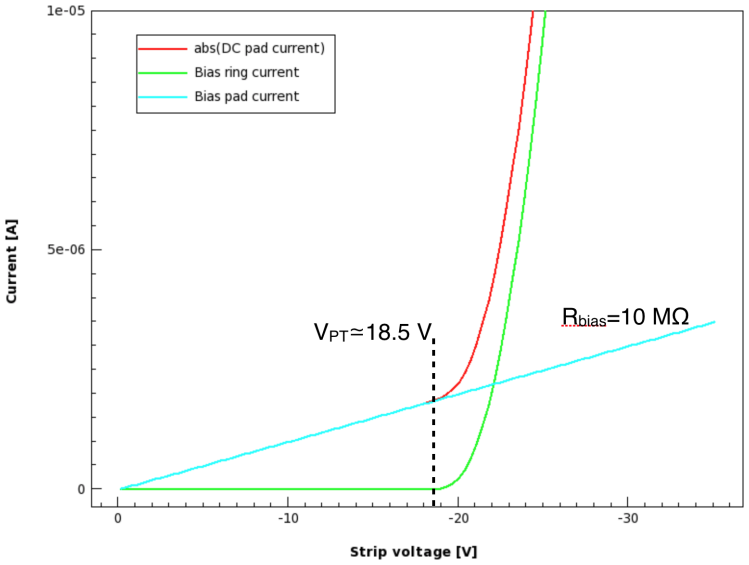

Figure 4.18: Strip-bias ring n PT simulation results. Currents flowing in the various nodes of the simulation, varying the voltage applied on the n strip: n strip (DC pad red), bias ring (green) and bias contact, used to simulate the polysilicon bias resistor (light blue).

The strip current initially flows to the bias contact through the bias resistance of 10 MΩ; in a real sensor this current finally goes to the bias ring, where the bias resistance are connected; in the simulation the bias contact is not connected to the bias ring, even if it is

set to the same voltage, so this current is not visible in the bias ring. After the activation of the punch through, an additional huge current starts to flow from the n-strip to the bias ring-n through the bulk (as shown in fig. 4.11 rigth). From this simulation, the PT voltage is 18.5 V, which is higher w.r.t the strip-strip PT voltage and also higher than the measured PT voltage in real sensors, where both strip-strip PT and strip-bias ring PT effects start at ∼13 V. One could expect that a better agreement with the measured PT could be achieved with a 3D simulation of the device, but this was beyond the goals of this thesis work. The main objective of this simulation is to qualitatively reproduce the punch through on the n-side in order to study the effects seen during the electrical tests, relatively to the deep pinhole connected to the APV25 input.

The simulation was also performed for different values of area factor and for each value, the punch through resistance is calculated. The R_{PT} consists in the slope of the curves after V_{PT} (fig. 4.19).

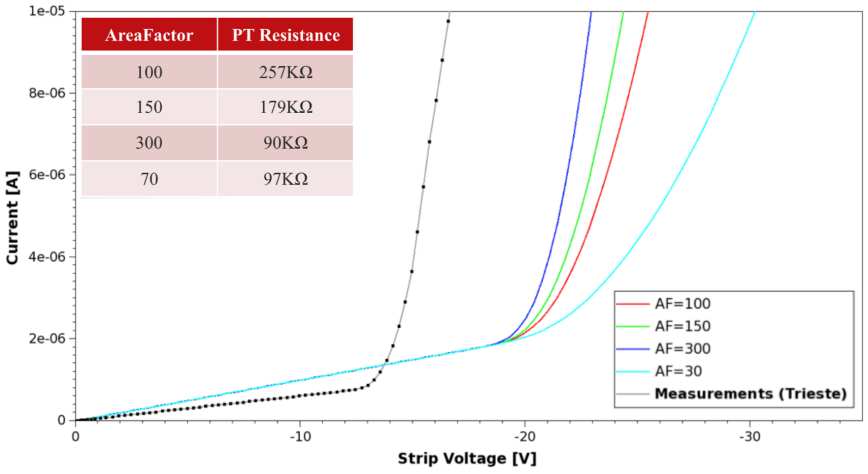

Figure 4.19: Simulation results of the current flowing via PT from the n strip to the bias ring n (equivalent width of the strip) for different values of AreaFactor. The grey line represents the measurements performed in Trieste, which slope, before the PT, is slightly different from the simulation curves because the real value of R_{poly} is not exactly the same of the nominal one.

The results show that R_{PT}=200 $K\Omega$ if the AF value is around 120 μm; for this reason, hereafter this value of area factor will be consider the correct one. This parameter has a reasonable value, considering that the pitch between the n-strips is about 120 μm and that the PT originated on the head of the strip is not confined to the 15 μm implant width.

4.4 Defect simulation and analysis of the results

The aim of this simulation is to study the behaviour of a deep pinhole defect, in order to understand if the effects observed in the pathological assembled modules can be explained with the presence of such defect in the silicon sensor. The deep pinhole (i.e. breaking of the oxide layer between the AC aluminium strip and the substrate) is simulated, on p-side, as a contact placed on the separation surface between the oxide layer and the bulk. At first, the potential of the n-bulk just below the oxide layer, in the region between two adjacent p-strips, has been evaluated from the simulation. This allows us to know the natural potential of the deep pinhole and its dependence with the position of the defect with respect to the edge of the closer p-strip (two different defect positions are considered later). The sensor is biased (0 V on p-side and 100 V on n-side) and the potential in the region between two adjacent p-strips is extracted. Figure 4.20 displays the potential, considering two different oxide charge concentration ($Q_{ox} = 10^{11}\ cm^{-2}$ and $Q_{ox} = 10^{12}\ cm^{-2}$), together with the space charge in the same area.

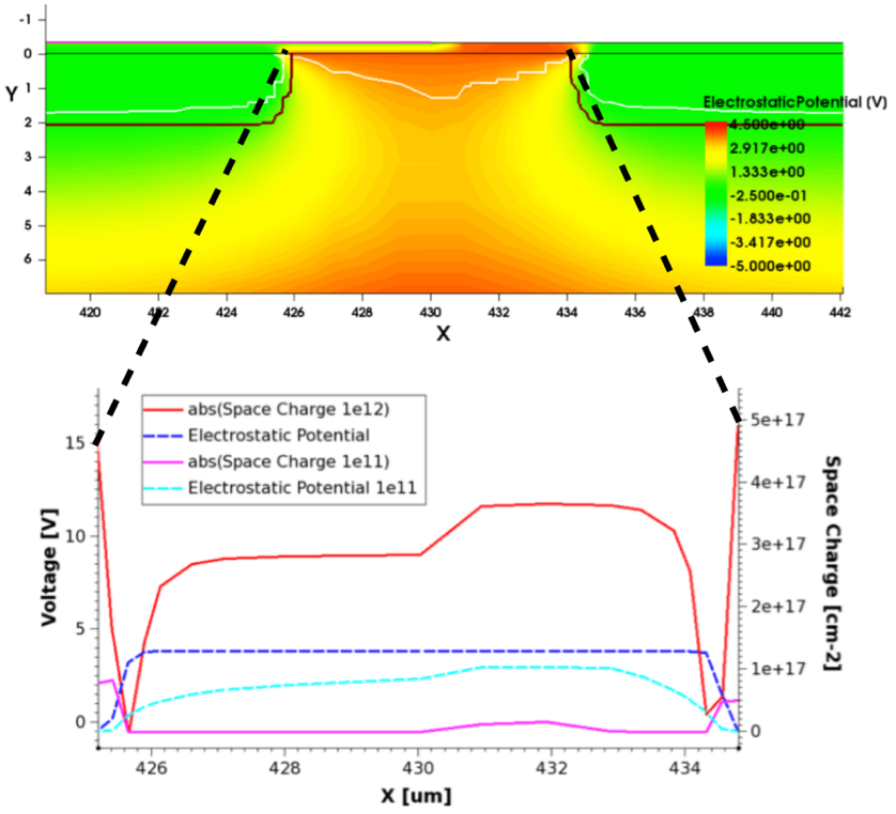

Figure 4.20: Behaviour of the potential surface between two adjacent p-strips. On the bottom, the potential together with the depletion width is reported for two different values of oxide charge, in order to verify the expected behaviour.

While on the p-strips the potential is 0 V, the result shows that the potential in that region of the bulk, just below the oxide, can be as high as $\sim +4V$ for $Q_{ox} = 10^{12} cm^{-2}$. This value depends on the distance from the p-strip edges and on the oxide charge concentration. The oxide charge induces an electron accumulation layer on the internal surface of the sensor so that the region can't be fully depleted; thus, increasing the oxide charge both the potential and the space charge increase.

Then, the effect of the V_{sep} voltage on the deep pinhole should be reproduced, in order to compare the results with the measurements performed in the Pisa laboratory (see section 3.4.4). The V_{sep} potential can be simulated applying a certain voltage to the contact that represents the deep pinhole. In fact, considering that the deep pinhole made a direct connection between the bulk and the AC pad, applying a voltage on the pinhole contact means applying a voltage on the AC pad; moreover the AC pad has the same potential of the APV25 input that correspond to V_{sep} + 0.75 V thus $V_{pinhole} = V_{sep}$+0.75 V. Then, the bias voltage of 100 V is applied and the pinhole voltage has been varied from -5 V to +5 V. The current flowing into the pinhole corresponds to the current flowing into the APV25. Thus, the dependence of the pinhole current with its potential can be directly compared with the measurements in 3.32 described in section 3.4.3. This study has been made for two different positions of the defect (fig. 4.21 right), which is called inner pinhole (0.2 μm from the closer p-strip) and outer pinhole (1.5 μm from the closer p-strip). The results are shown in figure 4.21 on the left.

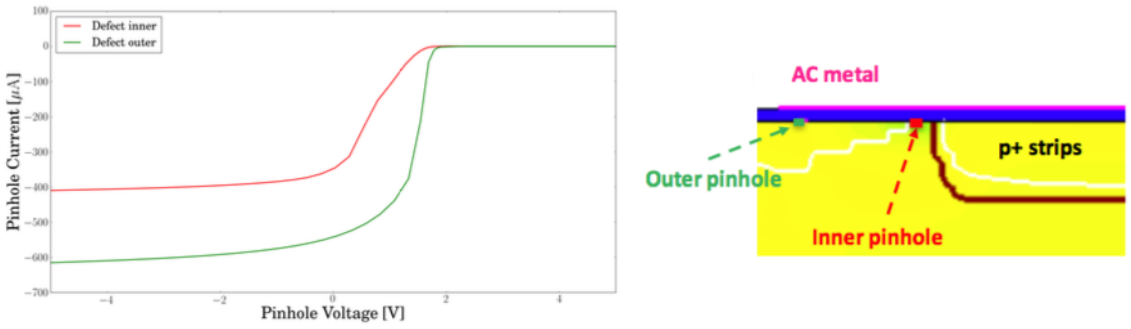

Figure 4.21: Right: display of the position of the inner and the outer deep pinhole with respect to the closer p-strip. Left: Simulation result of the deep pinhole current with respect to the pinhole voltage $V_{pinhole}$. Here, the red line corresponds to the inner pinhole while the green one corresponds to the outer pinhole. In the case of the outer pinhole, for $V_{pinhole} > +2$ V the current goes to 0, meaning that, in the real situation, no current is flowing towards the APV25 input. In the case of inner pinhole the same qualitative behaviour is shown for $V_{pinhole} > 1.6$ V.

- When the deep pinhole voltage is above its natural voltage, the pinhole current is negligible; thus no current is flowing in the APV25 input, the pre-amplifier channel works normally and the bias current of the sensor is small. This situation corresponds to $V_{sep} > +2$ V, for which the assembled modules with deep pinholes did not show any abnormal value of the bias current and they also had a normal gain;

- When the deep pinhole voltage is, instead, below its natural potential, an high current is generated. This current flows into the pinhole contact, implying an high current into the APV25 input (fig. 4.22).

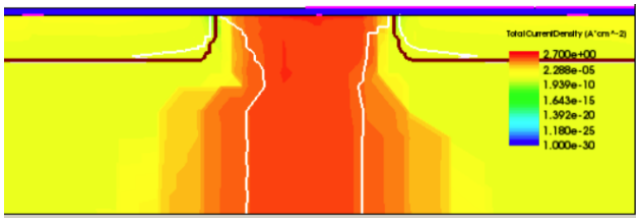

Figure 4.22: Simulation of the high current flowing through the deep pinhole when its voltage is below its natural potential.

In this condition the APV25 channel doesn't work and its gain goes to 0. Previous results (fig. 4.20)) show that the pinhole potential sits between 0 V and 4 V, that is compatible with the result shows in figure 4.21. The natural potentials of the inner and the outer pinholes are slightly different and this difference results in the behaviour shows in figure 4.21 (left), as expected. In this condition, the large current, due to the deep pinhole flows in the bulk, flowing also through the n-side strip in correspondence of the defect and consequently towards the bias ring via punch trough. This behaviour has been simulated in the previous section and can explain the noisy strips detected by the electrical tests, corresponding to strips with high leakage current and increased noise.

The results of the simulated deep pinhole current w.r.t. its voltage match well the shape of the measured current on the deep pinhole (fig. 3.32), as the shape of the APV25 gain w.r.t. V_{sep} for the deep pinhole (fig. 3.24 left).
This confirms that our interpretation of the behaviour of the observed new defect "deep pinhole", as a broken oxide to the n-bulk, is correct. The final comparison between the measurement results and the simulation outputs are displayed in figure 4.23.

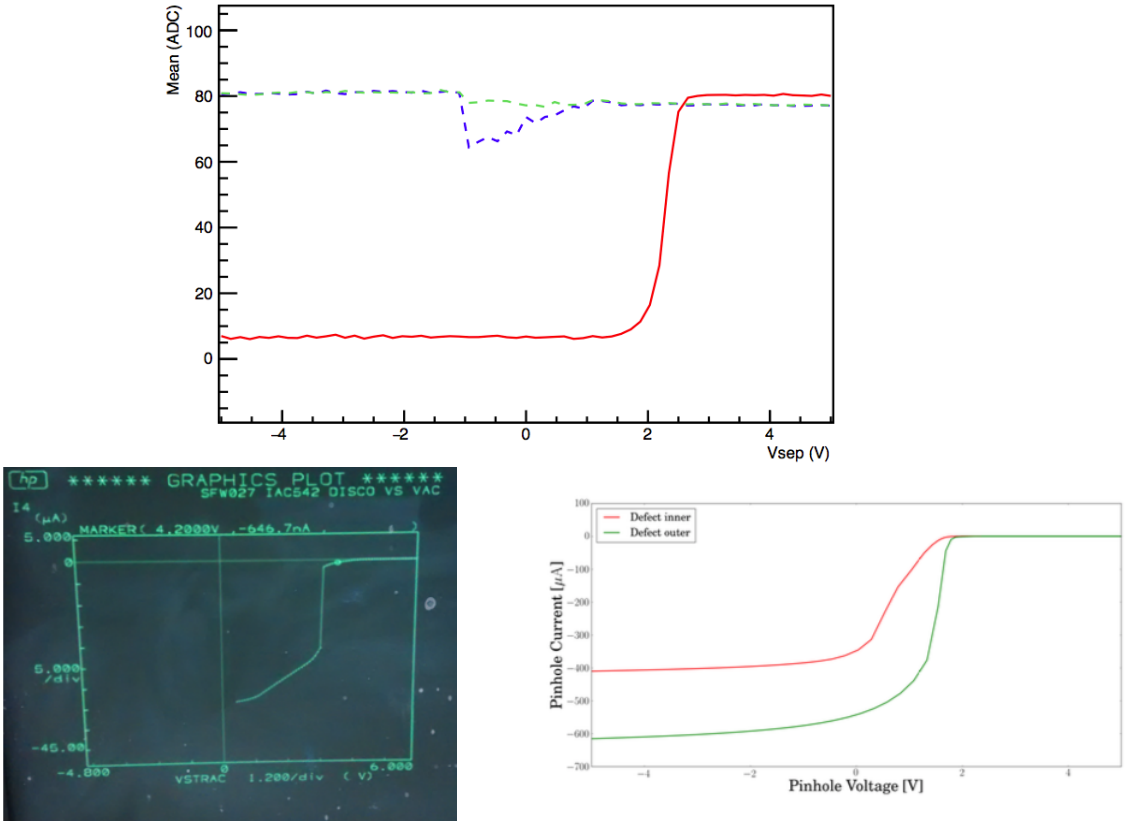

Figure 4.23: Comparison between the simulated (bottom right) and measured (bottom left) pinhole I-V. On top, the behaviour of the gain of the APV25 vs V_{sep} is shown. The same qualitative behaviour is reproduced by the simulation.

The simulation structure implemented can be helpful to understand other future electrical behaviour issues. For example, it can be used to study the behaviour of the double pinhole defect with respect to the V_{sep} voltage (fig. 3.26).

Chapter 5

Analysis of CP asymmetry for $B^0 \longrightarrow K^0_S \pi^0 \gamma$

As discussed in chapter 1, the analysis of CP asymmetries of the $B^0 \longrightarrow K^0_S \pi^0 \gamma$ decay can be sensitive to the helicity structure of NP particles in the loop diagrams. This effects can be detected measuring the coefficients in front of the sine and cosine terms in the pdf of the time-dependent CP asymmetry reported in equation 1.28. In this chapter, the resolution on the decay time difference (Δt) between B^0 and $\overline{B}^0$, is extracted from their reconstructed vertex positions. A data sample of 100000 events $\Upsilon(4S) \longrightarrow B^0\overline{B}^0$ with $B^0 \longrightarrow K^0_S \pi^0 \gamma$ and $\overline{B}^0 \longrightarrow \textit{Generic}$ is generated and reconstructed. In the following, the B^0 decaying into the chosen channel is called B^0_{sig} while the other one in the event is called B^0_{tag}. For the the B^0_{sig} vertex, the extrapolated K^0_S is the only usable track emerging from the vertex (these kaons are required to decay into $\pi^+\pi^-$) and in the fit procedure the additional constraint of the beam spot (called "iptube") must be used. Then the B^0_{tag} vertex is reconstructed using the information of the tracks belonging to the Rest Of Event (ROE), that is everything but the B^0_{sig} daughters. Using the vertex coordinates of the B^0_{sig} and the B^0_{tag}, one can obtain the z difference (Δz) and consequently the Δt through the relation: $\Delta z = \beta \cdot \gamma \cdot c \cdot \Delta t$ (fig. 5.1), where $\beta\gamma$ is the CM boost. The presence of leptons and kaons in the event is used to identify the flavour of the B^0_{tag} by the tagging algorithm. Finally, the Δt distribution of signal and background events is fitted with the predicted pdf, to extract the coefficients of the sine and cosine term. A Toy Monte Carlo method has been used to estimate the sensitivities with the predicted number of signal and background events.

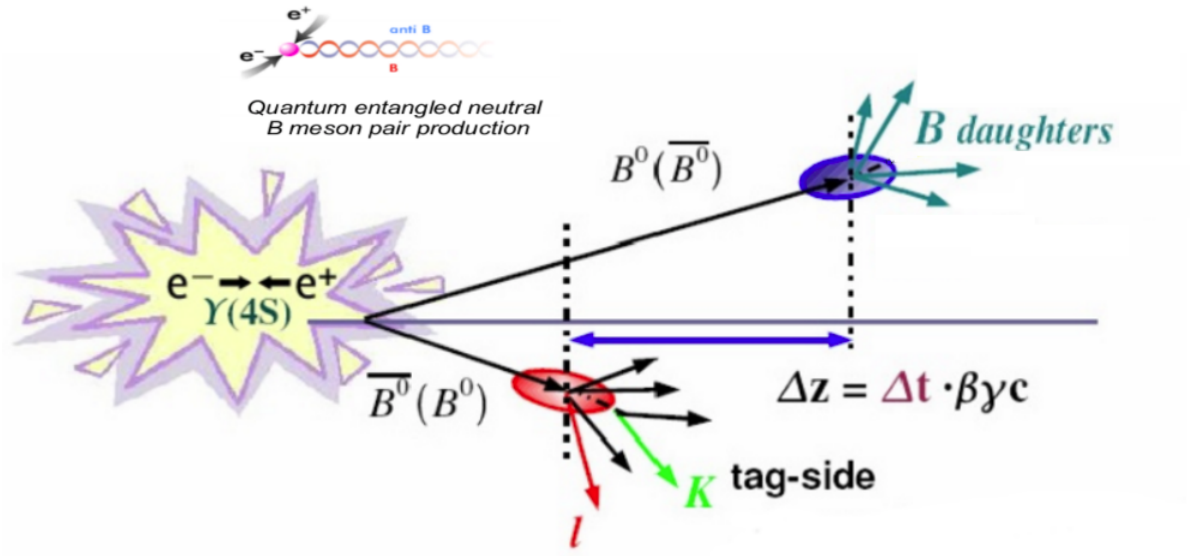

Figure 5.1: Schematic representation of the decay studied. Here the difference between the z coordinates of the neutral B vertices is displayed.

5.1 Software tools

This analysis is performed on monte carlo samples. Now the experiment is under construction and the start of data taking is expected in late 2018 with the fully equipped detector. Therefore, the Belle II software called BASF2 [36] (Belle Analysis Software Framework 2) is used in order to generate, reconstruct and analyse the events. BASF2 uses a modularized approach with a fixed set of virtual functions available to all modules. Several modules can be arbitrarily ordered and sequentially executed in order to form a path, which is configured over a so-called steering file. The latter is executed using a Python script language interpreter; it sets up the BASF2 parameters and it configures the system paths. A common data-store is used in order to allow the exchange of information between different modules and it can be accessed by every modules in the path. A standard example of a path is shown in figure 5.2.
Furthermore the BASF2 software imports some external libraries. The most important are listed below:

- EvtGen and PYTHIA [37], [38]: they are used for the event generation process;
- Geant4 [39]: it is used to simulate the interactions of the particles with the matter,

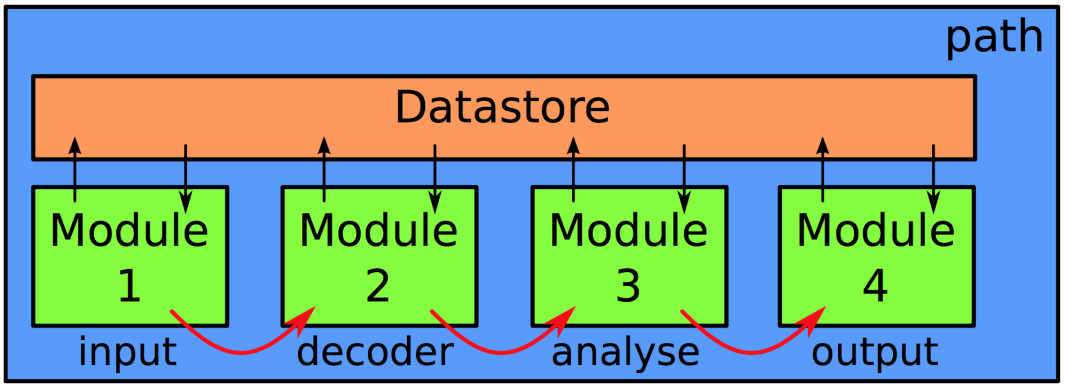

Figure 5.2: Example of a data processing chain. A path is displayed, containing 4 modules that exchange data with each other through the common data-store.

taking into account the final detector geometry;

- ROOT [40]: it is the framework used to analyse large amounts of data.

For what concern the vertex fit procedures, in this work two different tools are used: the kFit [41] and the RaveFit [42].

- kFit: it is the basic vertexing tool fit used originally by the Belle experiment. It is a kinematic fit that uses the method of the least square of χ^2. The χ^2 is calculated analytically by linearization of the constrained equations, by using the Lagrangian multipliers method. The kFit method is faster than RaveFit because it has less options available and it is not a geometric fit. It is used for both mass and vertex fits.

- RaveFit: it is a general vertex reconstruction algorithm that takes a set of reconstructed tracks as its input and produces reconstructed interaction vertices as output. It deals both with finding (pattern recognition) and with fitting (statistical estimate) the interaction vertices. The main features of the RAVE toolkit are: a robust reconstruction algorithms with estimators based on adaptive filters (Adaptive Vertex Fitter AVF), in order to down-weight the influence of outlier tracks (fig. 5.3), having a Application Programming Interface (API) which makes the program easy to use and adaptable to other software experiments.

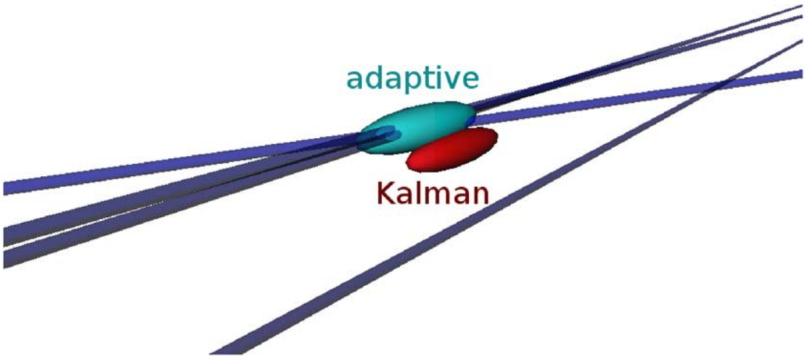

Figure 5.3: Vertex reconstruction example of the decay $J/\Psi \rightarrow K^+K^-\mu^+\mu^-$ where one of the tracks is mis-measured. Here the estimate of the adaptive method is less influenced by the mis-measured track with respect to the standard algorithm (Kalman).

5.2 Event generation and reconstruction process

At first, a data sample of 10000 events of $\Upsilon(4S) \longrightarrow B^0\overline{B}^0$ is generated, simulated and then reconstructed; one of the B^0 mesons (B^0_{sig}) is forced to decay into $K^0_S\pi^0\gamma$ and the other one decays generically, according to the PDG branching fractions. Furthermore the K^0_S is forced to decay into $\pi^+\pi^-$ and the π^0 into $\gamma\gamma$. For this particular analysis, in which the K^0_S reconstruction plays an important role, the decay $K^0_S \longrightarrow \pi^0\pi^0$ cannot be considered because it cannot provide a vertex of the K^0_S good enough for the extrapolation to the B^0_{sig} vertex. The data sample is generated and stored into a Mini Data Summary Tape (mdst) ntupla. Thus, the simulation of particles passing through the detector is implemented using Geant4 libraries. At the end of the simulation process, a mdst ntuple is created and it will be used as input for the reconstruction script. After that, the B^0_{sig} and all its daughters are reconstructed through a dedicated script, which performs the selection cuts on energy, momentum, timing and mass. Furthermore, the reconstruction script implements the fit methods used, the vertex reconstruction processes, the flavour tagging procedure and the rest of event reconstruction.

Once the reconstruction process is performed, the reconstruction efficiency is defined as:

$$\varepsilon^{reco} = \frac{\#\ of\ perfectly\ reconstructed\ particles}{\#\ of\ generated\ particles\ within\ the\ sensitive\ volume} \tag{5.1}$$

where a particle is perfectly reconstructed when the reconstruction process doesn't produce any kind of errors. All the kinds of error that can occur during the reconstruction process are shown in table 5.1.

Name	Code	Description of the error
Correct	0	The particle and all its daughters are perfectly reconstructed.
MissFSR	1	A Final State Radiation (FSR) photon is not reconstructed.
MissingResonance	2	The associated MC particle decay contains additional non-FS particles.
DecayInFlight	4	A particle is reconstructed from the secondary decay product of the actual particle. It means that a wrong hypothesis is used to reconstruct it (e.g. a $\pi^{\pm}$ hypothesis is used for a secondary $e^{\pm}$).
MissNeutrino	8	A neutrino is missing, meaning that it is not reconstructed.
MissGamma	16	A photon (not FSR) is missing, meaning that it is not reconstructed.
MissMassiveParticle	32	A generated massive FSP is missing, meaning that it is not reconstructed.
MissKlong	64	A K_L^0 is missing, meaning that it is not reconstructed.
MisID	128	One of the charged final state particles is mis-identified.
AddedWrongParticle	256	A non-FSP particle has wrong PDG code, meaning that one of the daughters comes from another particle.
InternalError	512	A not valid MC match occurs.

Table 5.1: Summarized description of the possible errors that can be produced by the reconstruction process. If one or more errors are detected, the relative code will be the sum of the code of the individual error.

Furthermore, it is useful to define the residual and pull quantities, which will be used later as a quality test for the reconstructed particles. These variables are defined as follow, considering the π^0 mass as an example:

$$Residuals = M_{\pi^0}^{reco} - M_{\pi^0}^{truth} \tag{5.2}$$

$$Pull = \frac{M_{\pi^0}^{reco} - M_{\pi^0}^{truth}}{M_{\pi^0}^{err}} = \frac{Residuals}{\sigma_{M_{\pi^0}}} \tag{5.3}$$

5.2.1 Photon reconstruction

Photons are defined through five different type of variables:

- E: energy of the photons;
- minC2HDist: minimum distance between the photons estimated position and the closest track described by an helix;
- E9/E25: ratio of energies in 3x3 and 5x5 calorimeter cells. It indicates the spread of the photons energy;

- clusterReg: detection region in the ECL. It is associated to three different values: 1 for the forward region, 2 for the barrel and 3 for the backward;
- cluster timing: timing of the detected particle in the calorimeter. Particles belonging to the beam background are not in time with the particles of interest.

Each variable is used to apply cuts (summerised in table 5.2) which provides us the definition of all the photons reconstructed in an event.

Detector region	forward	barrel	backward
Energy (MeV)	103	97	72
Cluster timing (ps)	-16 < time < 16	- 18 < time < 18	-32 < time < 32
E9/E25	0.80	0.78	0.71
minC2Hdist (cm)	55	36	49

Table 5.2: Cuts applied to define photons in the event. Those cuts are taken from optimized studies of other collaborators.

The energy residual and pull distributions of photons are shown in figure 5.4, respectively on the left and on the right. The reconstruction efficiency is about 43%. These results are obtained requiring the "MC matching", meaning that no errors occurred during the reconstruction process (error ID=0 as explained in table 5.1).

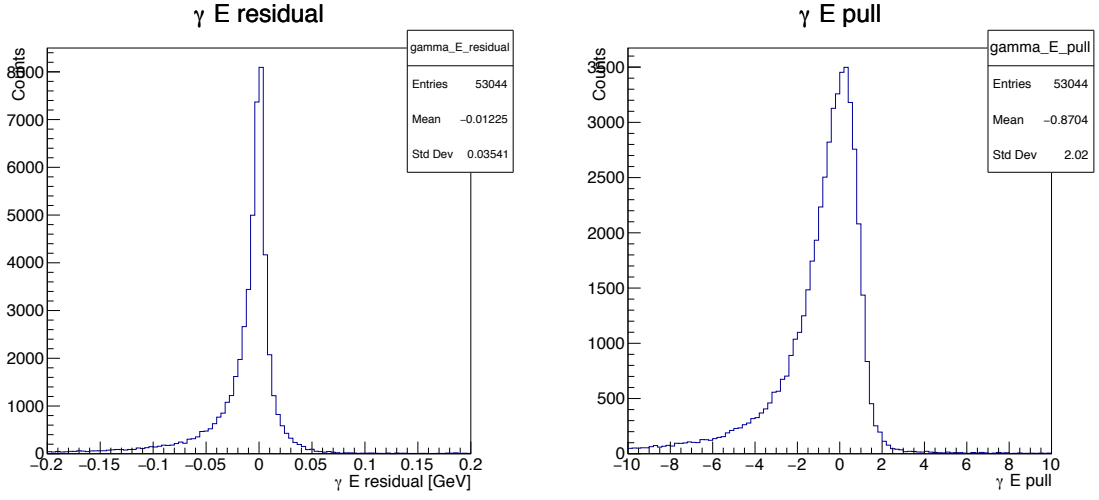

Figure 5.4: Left: energy residual distribution of all photons reconstructed in the events. Right: energy pull distribution of all photons reconstructed in the event; it has not been fitted with a Gaussian distribution because of the long negative tail. The efficiency extracted from these plots is referring to all the photons in the event (not only the photons coming from the B^0_{sig}).

The residual distribution has a long negative tail because the energy of the photons is always underestimated, due to calorimeter leakages and to interactions of photons with the material in front of the calorimeter. This effect is more pronounced for low energy photons, and it is visible also in the pull distribution.

5.2.2 π^0 reconstruction

Neutral pions are reconstructed through the decay $\pi^0 \longrightarrow \gamma\gamma$, where photons are defined as in table 5.2; an invariant mass is required between 110 MeV/c^2 and 150 MeV/c^2 and then the kinematic mass fit (Kfit type) is required to have a p-value $> 1‰$. In this decay, a vertex fit can't be used because no charged particles are available. In order to check if the reconstruction process doesn't produce wrong results, the mass residual (fig. 5.5 left) and pull (fig. 5.5 right) distributions are produced.

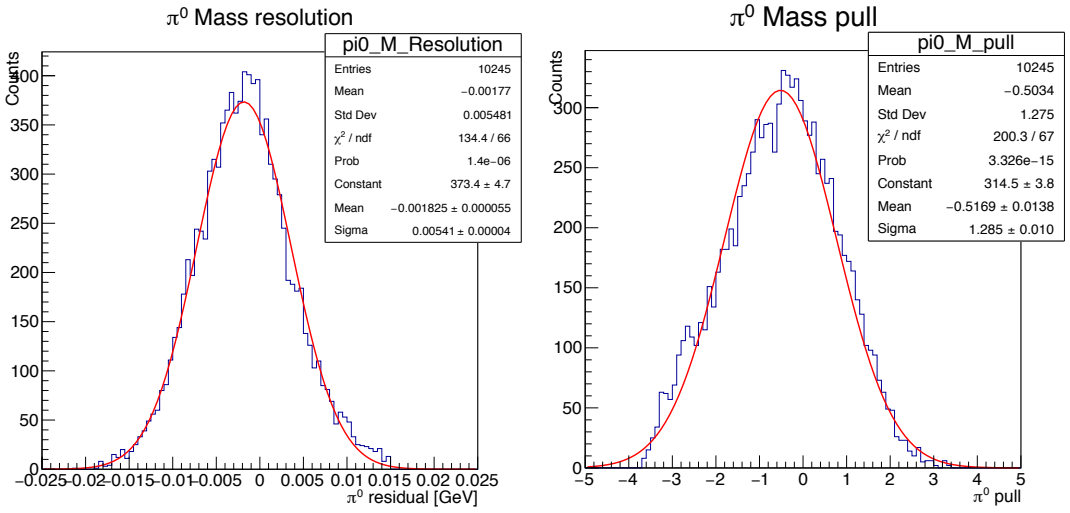

Figure 5.5: Left: mass residual distribution of all the π^0 in the event; it is fitted with a Gaussian function. Right: mass pull distribution of all the π^0 in the event; it is fitted with a Gaussian function.

Two important numbers are extracted from these distributions: the mass resolution, that corresponds to the σ of the Gaussian function used in the residual distribution, and the σ of the Gaussian function of the pull distribution. The latter must be unitary in case of correctly estimated errors. The results show that the pions reconstruction efficiency is around 27.5%. This value refers to all the π^0 reconstructed in the event, meaning that only a small fraction of them comes from the B^0_{sig} decays. Furthermore both the distributions have a bias towards negative values, due to the underestimation of the photon energy.

The π^0 mass resolution is 5.41 ± 0.04 MeV/c^2 and the Gaussian function of the pull has $\sigma = 1.285 \pm 0.010$. These values are not as good as expected and the reason lies again in the definition of the photons, that are not yet optimized in the Belle II software. At the moment, this is one of the most important issue of the reconstruction code in the experiment.

5.2.3 K^0_S reconstruction

The reconstruction of K^0_S is one of the crucial points of this analysis, because it is the only particle used to reconstruct the vertex position of the B^0_{sig}. The K^0_S is reconstructed only through the decay into charged pions $K^0_S \longrightarrow \pi^+\pi^-$, which provides us good vertex resolution, although it means losing ∼33% of statistic due to the branching fraction. All charged tracks in the event can be reconstructed as Final State (FS) particles; at the tracking level, the track helix is determined (using kalman algorithm) by 5 parameters defined at the Point Of Closest Approach (POCA) to the IP and then it is stored into a mdst ntuple. Let's consider a K^0_S decaying between the PXD and the SVD; the daughter tracks ($\pi^+\pi^-$) are extrapolated through the PXD layers and the beam pipe, while they actually didn't cross those layers. This leads to inaccuracies in the K^0_S reconstruction, due mainly to multiple scattering effects. In order to overcome this issue, the K^0_S is defined as a V^0 particle, which is a neutral object that appears as a vertex of two charged particles away from the interaction point. At the tracking level, V^0 candidates are defined as a pair of charged tracks extrapolated to the innermost hit position and selected through a fast vertex fit. The extrapolation to the innermost hit position of the track before the vertex fit allows to overcome the inaccuracy mentioned in the FS definition.
Kaons are reconstructed requiring a mass between 400 MeV/c^2 and 600 MeV/c^2 and performing a vertex fit (KFit type) with a p-value over than 1‰. The mass residual and pull distributions are shown respectively in figure 5.6 left and right.
The results show a reconstruction efficiency of 46.5%. The mass residual distribution is fitted with the sum of two Gaussians, meaning that there are two different sets of reconstructed K^0_S with different resolutions: $\sim$ 2 MeV/c^2 and $\sim$ 7 MeV/c^2. Expressing the resolution as the weighted average of the two σ values (the weights are relative to the number of events belonging to the corresponding Gaussian functions), we obtain ∼3 MeV/c^2. The pull distribution seems to have no major problems as $\sigma \simeq 1.1$. Anyway, a small negative bias affected both the distributions, indicating that the K^0_S reconstruction

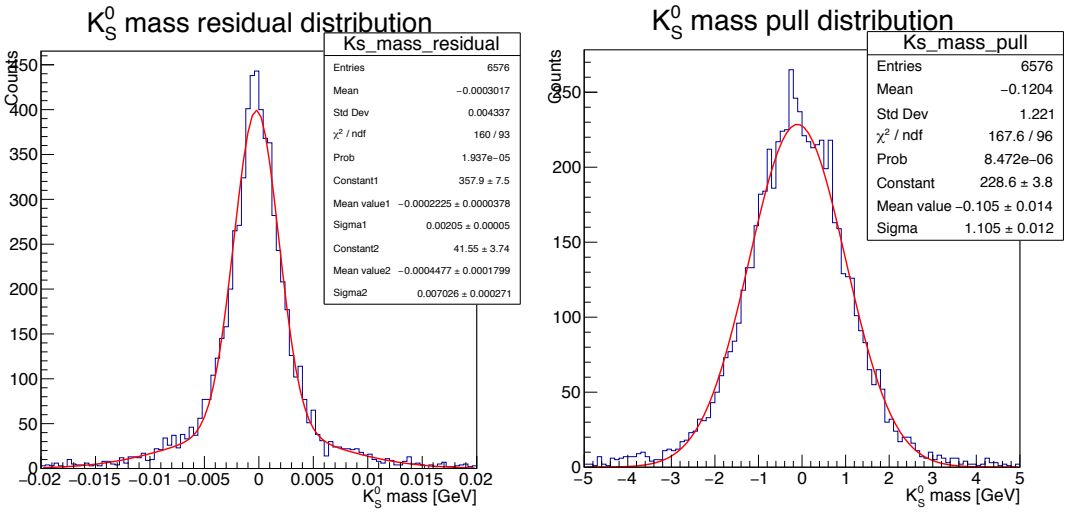

Figure 5.6: Left: mass residual distribution of all the K^0_S in the event; it is fitted with a sum of two different Gaussian functions. Right: mass pull distribution of all the K^0_S in the event; it is fitted with only one Gaussian function.

needs to be optimised.

5.3 Vertex fit and flavour tagging

In this section, the vertex fits of the B^0_{sig} and the B^0_{tag} are performed, in order to extract the time difference between the two mesons and consequently the resolution. Furthermore the flavour tagging procedure is applied to assign the flavour to the B^0_{tag}.

5.3.1 B^0_{sig} reconstruction

The B^0_{sig} is reconstructed by using the definition of its daughters given before, and requiring an invariant mass between 5.0 GeV/c^2 and 5.5 GeV/c^2. Then a vertex fit (RaveFit type) is performed requiring a p-value $> 1‰$. In order to reconstruct the B^0_{sig} vertex position it is necessary to use the K^0_S extrapolated track with an additional constraint called "iptube", defined as an ellipse placed around the boost direction with transversal dimensions equal to the beam spot (fig. 5.7): $\sigma_x^2 \simeq 6\ \mu m$, $\sigma_y^2 \simeq 42\ nm$ (see section 2.1.1). Although one doesn't want to set any constraint along z, because the real z position of the reconstructed vertices should not be modified, the iptube function need also a z dimension value as input; thus, this value is set equal to 2 cm, that is more than 100 times the medium flight length of the B meson, meaning no constraint. For the current status of the Belle II software, the RaveFit method is the only one that allows to use the iptube constraint.

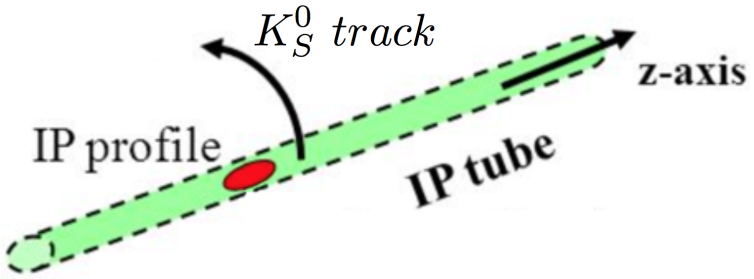

Figure 5.7: Graphical representation of the iptube constraint.

Furthermore, it is necessary to perform a cut on the invariant mass of the system $K^0_S\pi^0$ because the SM prediction of the S parameter is based on the SCET theory, that holds for soft and collinear K^0_S and π^0 (see section 2.3.1). This invariant mass is defined as $M_{K^0_S\pi^0} = \sqrt{M^2_{B^0} - 2(E_{B^0}P_\gamma - \vec{P}_{B^0}\cdot\vec{P}_\gamma)}$ where M_{B^0} and E_{B^0} are respectively the mass and the energy of the B^0_{sig} while P_γ is the momentum of the photons. The applied cut is $M_{K\pi}$ <1.8 GeV/c^2, the same used in BaBar [43] and Belle [44] analysis. This cut causes a severe rejection of signal events (a factor ∼6), thus I had to increase the number of generated events to 100000.

In order to check the B^0_{sig} reconstruction process, its mass distribution has been generated (5.8 left). The mass uncertainty depends on both the momentum and the mass hypothesis of the daughters. In order to eliminate the contribution of the mass hypothesis uncertainty, the M_{bc} ("beam constraint") variable [7] is considered. It is defined as $M_{bc} = \sqrt{E^{*2}_{beam} - p^{*2}_B}$ where p^*_B is the CM momentum of the B meson, derived from the momenta of its decay products, while the B meson energy is substituted with E^{*2}_{beam}. This variable is defined through the beam energies, which have a smaller uncertainty with respect to the B meson energy reconstructed from the decay, improving the mass resolution. The distribution of M_{bc} is reported in figure 5.8 (right) and it can be parametrized with the sum of two Gaussian functions. The resolution on M_{bc} results 3.35 MeV/c^2.

Another important physical quantity to look at is the ΔE [7], which is defined as below:

$$\Delta E = E^{CM}_{B^0} - \frac{\sqrt{s}}{2} \tag{5.4}$$

where $E^{CM}_{B^0}$ is the energy of the B^0 meson in the center of mass system (derived from the energy of its daughters), while $\frac{\sqrt{s}}{2}$ is the beam energy. It is used especially to disentangle background events involving misidentification from the signal events, as it depends strongly on the mass hypothesis of the particles. For example, if a kaon is misidentified

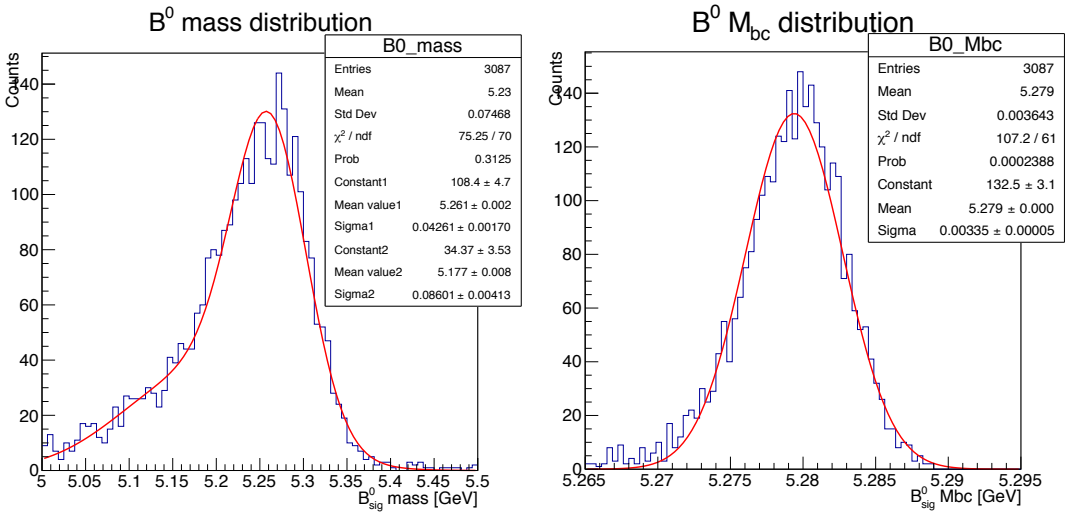

Figure 5.8: Mass (left) and M_{bc} (right) distribution of the B^0_{sig}.

as a pion, its energy will be smaller than its true value and consequently also the $E^{CM}_{B^0}$ of the B^0 candidate. This causes a shift on the ΔE towards negative values. In this analysis, the ΔE distribution is just used as check variable for the reconstruction process, resulting in the distribution reported in figure 5.9.

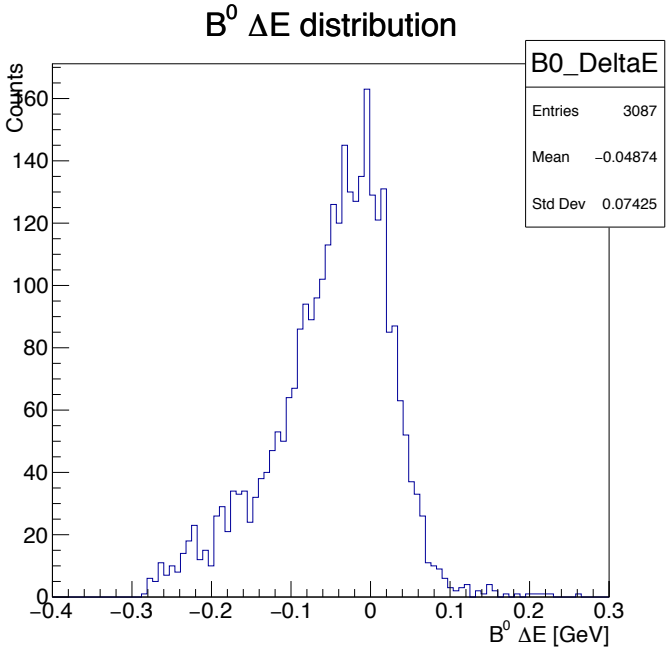

Figure 5.9: Distribution of ΔE. The negative tail is also due to the underestimated photons energy (see fig. 5.4).

Then, the B^0_{sig} vertex reconstruction is checked through the residual and the pull distributions of its Z coordinate. These distributions are shown in figure 5.10.

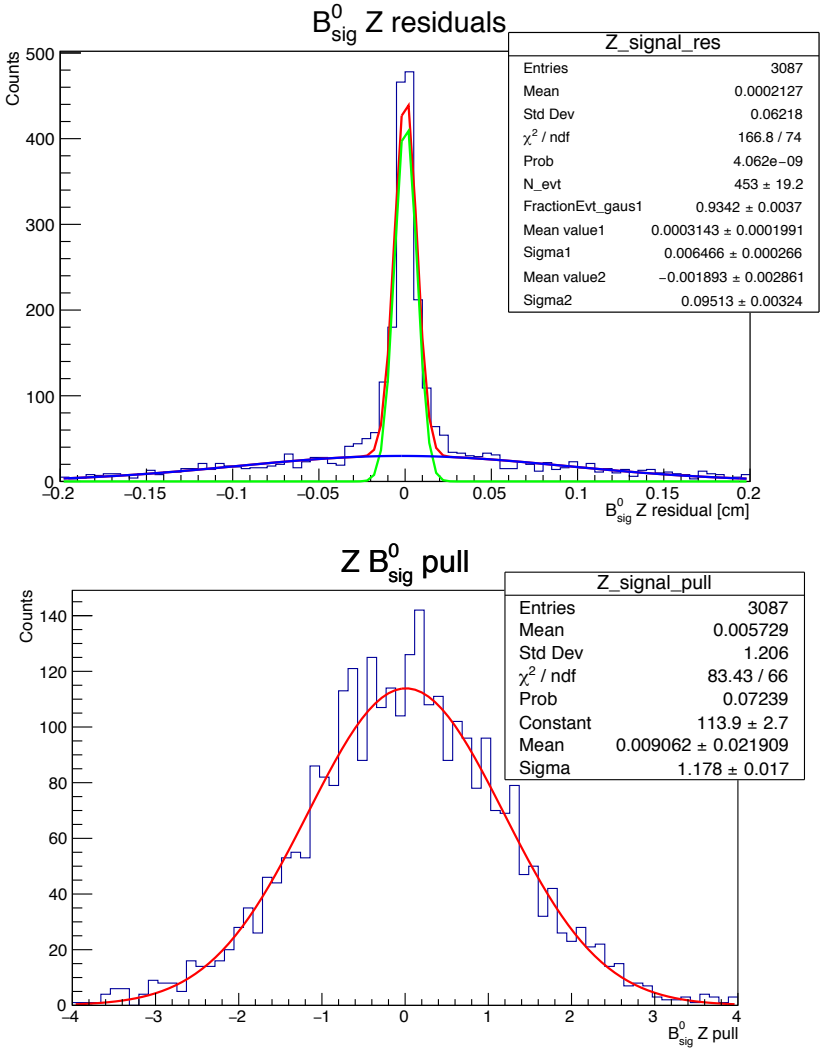

Figure 5.10: Residual (top) and pull (bottom) distributions of the z coordinate of B^0_{sig} vertex.The residual distribution is fitted with the sum of two different Gaussian functions, meaning that there are two sets of B^0 reconstructed with different precisions.

The pull distribution is not biased but its standard deviation is slightly higher than expected. The residual distribution is fitted with the sum of two different Gaussian functions, both centred around 0 and with quite different σ values: $\sigma_1 \simeq 65\mu m$ and $\sigma_2 \simeq 950\mu m$. The narrow Gaussian is called core-Gaussian ($\sim 93\%$ of the events) while the wide one is called tail-Gaussian. The σ values are dominated by the resolution of the reconstruction of the charged pions; in fact, the resolution value improves if the K^0_S decays before the first layer of SVD, meaning that the charged pions are reconstructed using the vertex detector

information. On the contrary, if the pions are reconstructed using only the CDC hits (the K_S^0 decay after the SVD layers) the resolution is heavily affected. The profile plot concerning the error on the z coordinate of the B_{sig}^0 vertex (coming from fit) as a function of the transverse flight distance of the K_S^0 is displayed in figure 5.11.

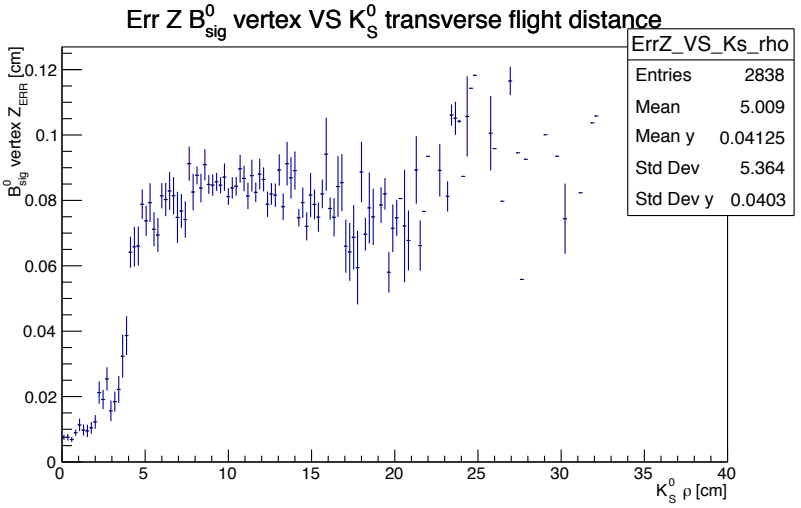

Figure 5.11: Profile plot of the error on the reconstruction of the z coordinate of the B_{sig}^0 vertex with respect to the transverse flight distance of the K_S^0. A clear step is present at ~ 3.8 cm, which corresponds to the radius of the first SVD layer.

Here, the expected step at around 3.8 cm (radius of the first SVD layer) is clearly visible, while the one at 16 cm, corresponding to the inner radius of the CDC, is missing. This is due to the details of the tracking algorithm, which is still under development. If a charged track is not detected in one SVD layer, the track is reconstructed only with the information coming from the CDC. It is expected that the final reconstruction software will be able to take advantage of all the SVD available hits.

5.3.2 B_{tag}^0 reconstruction

For the reconstruction of the B_{tag}^0 vertex, a complete exclusive reconstruction of the B_{tag}^0 is not performed, as it would imply an unacceptable statistic reduction. Thus, the B_{tag}^0 vertex reconstruction is performed through the function "tagV", which takes all the tracks in the rest of the event, excluding K_S^0 daughters, and performs an inclusive weighted geometric fit using the RAVE algorithm. Since the K_S^0 decays far from the IP, its decay information are not used in the fit, implying large errors on the vertex positions of the B^0; neutral kaons decays will be included with their relative weight in the final version of the

algorithm. Three categories can be distinguished: tracks originating from the B^0, tracks originating from D mesons and tracks originating from K^0_S decays. In order to reduce as much as possible the weight of the tracks originating from D mesons, an additional constraint defined by an ellipsoid around the boost direction is used, where the B^0 gains an higher probability to decay than D meson. This constrain acts as a weight in the final χ^2 of the fit. Moreover, the fit is performed requiring a $p - value > 1‰$ and one hit in the PXD detector for each particle included in the fit (this fitting option is called "standard_pxd"). This vertex fit procedure provides the vertex position of the B^0_{tag} with a resolution of around 42 μm as shown by the residual distribution in figure 5.12.

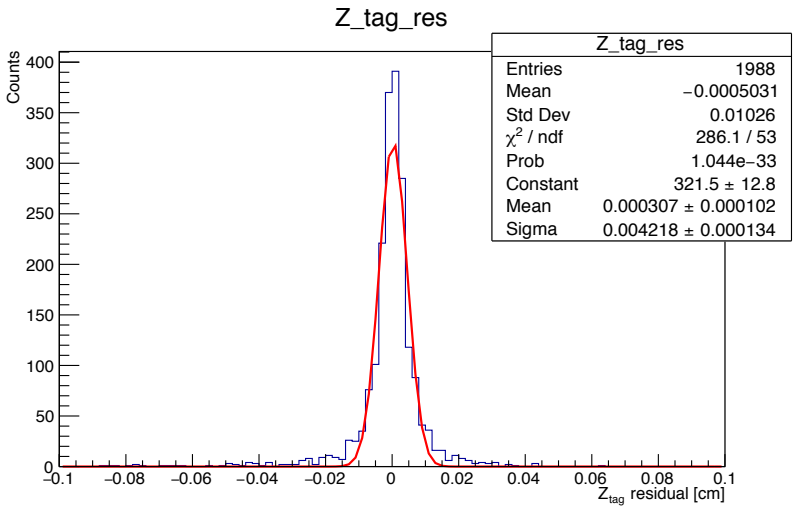

Figure 5.12: Residual distribution of the z coordinate of the B^0_{tag} vertex. The resolution value (σ_{Gauss}) is about 42 μm. Notice the presence of not-Gaussian tails that spread the RMS of the distribution up to ~ 100 μm.

In the channel $B^0 \longrightarrow K^0_S\pi^0\gamma$, the resolution on the difference between the z coordinates of the two B^0 decay vertices is dominated by the uncertainty on the B^0_{sig} vertex.

5.3.3 Flavour tagging

The flavour tagging algorithm allows to distinguish if the reconstructed B^0_{tag} meson is a B^0 or an $\overline{B}^0$. This information assigns the flavour of the B^0_{sig} at the decay time to the B^0_{tag}, being the two B^0s in orthogonal flavour states ("entanglement").
In order to tag the B^0_{tag}, different signatures of flavour specific decay channels can be grouped into (up tu now) 13 categories as shown in figure 5.13.

Categories	Targets
Electron	e^-
Intermediate Electron	e^+
Muon	μ^-
Intermediate Muon	μ^+
KinLepton	ℓ^-
Intermediate KinLepton	ℓ^+
Kaon	K^-
KaonPion	K^-, π^+
SlowPion	π^+
FastPion	π^-
MaximumP	ℓ^-, π^-
FSC	ℓ^-, π^+
Lambda	Λ
Total= 13	

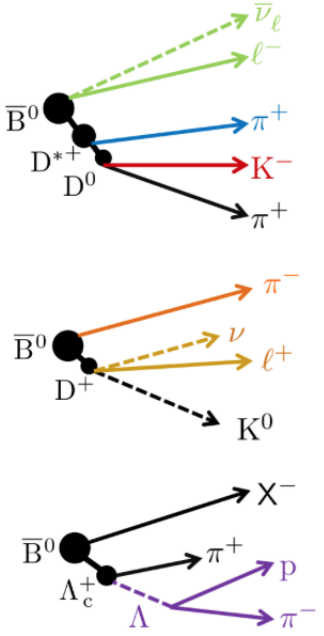

Figure 5.13: List of the 13 categories used to tag the B mesons.

Each category uses simple information like charge (mostly) and momentum in order to tag the B^0 mesons. The flavour tagging algorithm, inspired by the Belle and the BaBar ones, is described by three major steps (fig. 5.14) based on trained multivariate methods:

- At track level: a dedicated particle list is created for each category and it is filled with dummy particles corresponding to the ROE tracks. For example, all the tracks fitted with the mass hypothesis of K^+ are included in a certain particle list, corresponding to the kaon category. Then a multivariate analysis is performed for each category, using several kinematic tagging variables as input. It provides the probability of a track to be the RightTrack, i.e. the searched signature for the corresponding category.

- At event level: for each dummy particle, it performs a multivariate analysis using the flavour tagging variables introduced in the track level as input. This method provides the probability of being the RightCategory, that corresponds to the probability of a RightTrack to belong to the right category.

- At combiner level: it selects the tracks with the highest RightTrack probability and it uses the quantity $q \cdot p$ (the charge and the RightCategory probability respectively) as input to a multivariate method. The multivariate method of the combiner provides,

for each event, the product $q \cdot r$, where q is the flavour and r is the dilution factor: $r = 1 - 2\omega$. Here ω corresponds to the mistag probability, i.e. the probability to assign the wrong flavour to the B^0_{tag}.

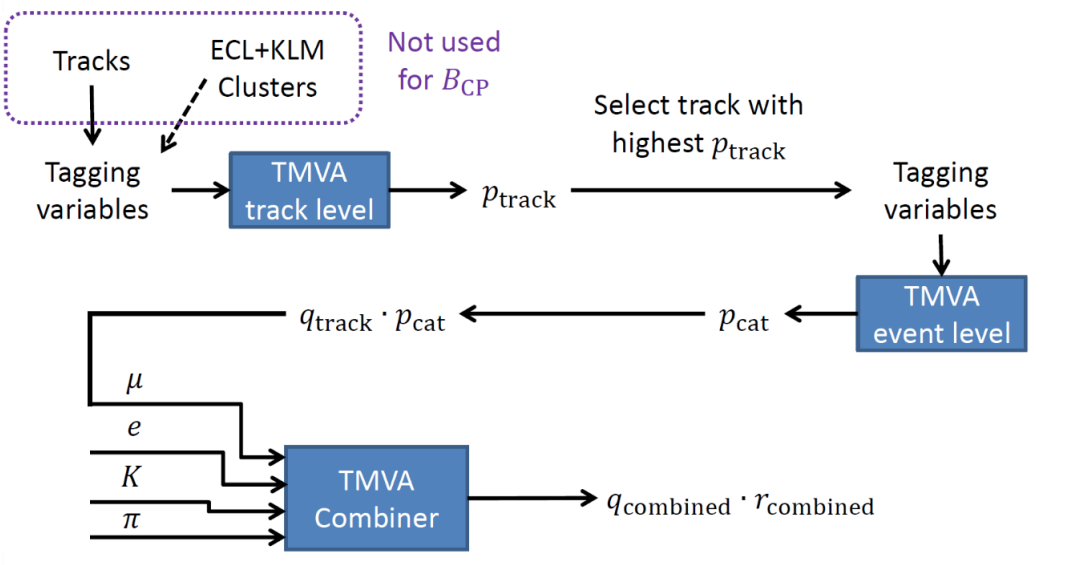

Figure 5.14: Scheme of the flavour tagging process. It uses information of the reconstructed tracks and ECL+KLM clusters in order to provide us the flavour of the B^0_{sig}.

As an additional output, the flavour tagging process provides the probability to correctly tag a B^0 or a $\overline{B}^0$. If this probability is over 0.5, than the B^0 is considered tagged. Requiring this condition, one can extract the tagging efficiency through the ratio of the number of B^0 tagged over the total number of B^0 reconstructed. The tagging efficiency results ~45%.

Some other important quantities, which will be used in the final fit of Δt (see section 5.5.2), are extracted from the output of the tagging procedure: μ= tagging efficiency difference between B^0 and $\overline{B}^0$, ω= mis-tag probability and $\Delta\omega$= mis-tag probability difference between B^0 and $\overline{B}^0$. The results are summarized in table 5.3.

μ	ω	$\Delta\omega$
0.0213	0.2512	0.0104

Table 5.3: Table of results of three important quantity extracted from the tagging procedure: the tagging efficiency difference μ, the mis-tag probability ω and the mis-tag probability difference $\Delta\omega$.

5.4 Efficiency studies

An important study consists in the estimate of efficiencies regarding the particles involved in the decay of the B^0_{sig}. In order to study these efficiencies, a clean data sample is generated, forcing the B^0_{sig} to decay into $K^0_S\pi^0\gamma$ and the B^0_{tag} to decay into a couple of $\nu\overline{\nu}$, so that it cannot introduce cross-feed reconstructed tracks from the B^0_{tag}. This data sample allows to estimate the ultimate reconstruction efficiency achievable with the Belle II detector and the event reconstruction software. The signal decays are simulated and the same cuts used in the previous sections are applied to these special events. This sample of data has been used only for this efficiency study, in order to obtain an upper limit to the reconstruction efficiency provided by the Belle II detector for the decay $B^0_{sig} \longrightarrow K^0_S\pi^0\gamma$. The distributions of the errors occurred during the reconstruction processes for π^0, K^0_S and B^0_{sig} are shown in figure 5.15.

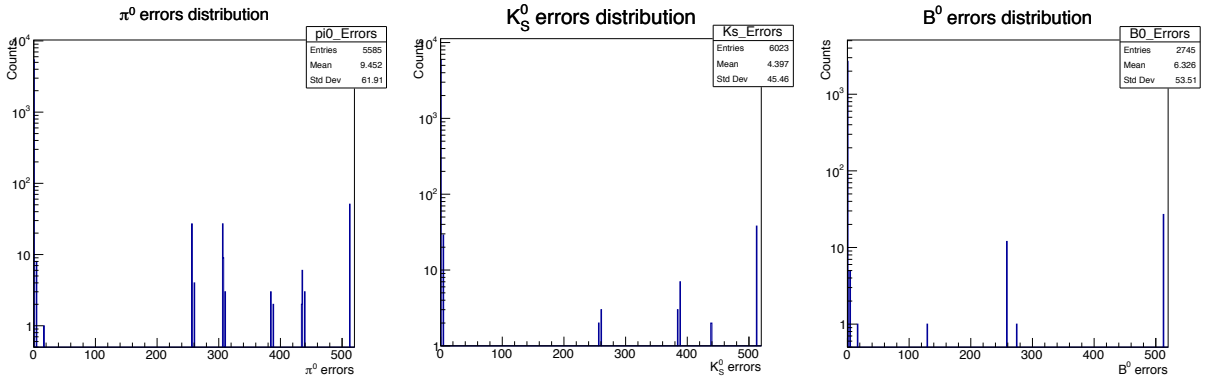

Figure 5.15: Distribution of the ID errors that occurs during the reconstruction process for neutral pions (left), neutral kaons (center) and neutral B mesons (right). See table 5.1 as reference.

From these plots, one can extract the efficiency values through the formula 5.1. The number of tracks perfectly reconstructed corresponds to the entries of the bin in 0. The efficiency for photons coming from the B^0 is obtained through the monte carlo matching information, thus the error distribution is not displayed. In the following table 5.4 the efficiency results are summarized:

	K^0_S	π^0	γ	B^0
ε^{reco}	58.6 %	53.7 %	83.4 %	26.2 %

Table 5.4: Reconstruction efficiencies of the particles involved in the decay. These values represent the maximum estimated efficiencies reachable with the current version of the reconstruction software.

5.5 Final results

In this section, the Δt resolution is estimated; it is an input needed to fit the Δt distribution, which follows the pdf reported in (1.28). Thus, the final estimates of the statistical uncertainties on the S and C parameters (introduced in 1.3.1) are extracted, proving the sensitivity of the Belle II experiment to unveil new physics effects in the asymmetry of $B^0 \longrightarrow K^0_S\pi^0\gamma$ channel.

5.5.1 Δt resolution

The evaluation of the Δt between the B^0_{sig} and B^0_{tag} is calculated from the difference in the z coordinate of the vertex position of the two B^0 mesons using the formula: $\Delta z = \beta\gamma \cdot c \cdot \Delta t$, where $\beta\gamma$ is the CM boost (see section 2.1). The resolution value is extracted from the residual distribution, which is derived as usual using the time value available in MC events: $\Delta t_{residual} = \Delta t_{reco} - \Delta t_{truth}$. The result is displayed in figure 5.16.

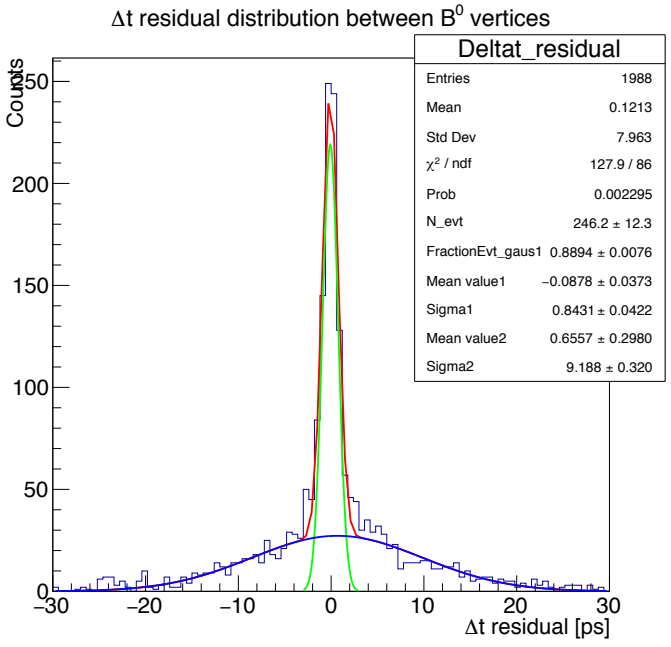

Figure 5.16: Δt residual distribution.

The residual distribution is fitted with the sum of two Gaussian functions. The narrow Gaussian ("core Gaussian") has a $\sigma \simeq 0.84$ ps and it contains a fraction of $\sim 89\%$ of the events, while the wide one shows a $\sigma \simeq 9.8$ ps. The same behaviour is displayed by the residual distribution of the B^0_{sig} vertex position (fig. 5.12), meaning that the long tails are due to issues on the reconstruction of the signal side. Thus, only the events included in the

core Gaussian should be considered. It is possible to select most of the events belonging to the core Gaussian imposing that both the pions coming from the K^0_S are reconstructed using the SVD hit information. The new Δt residual distribution is shown in figure 5.17.

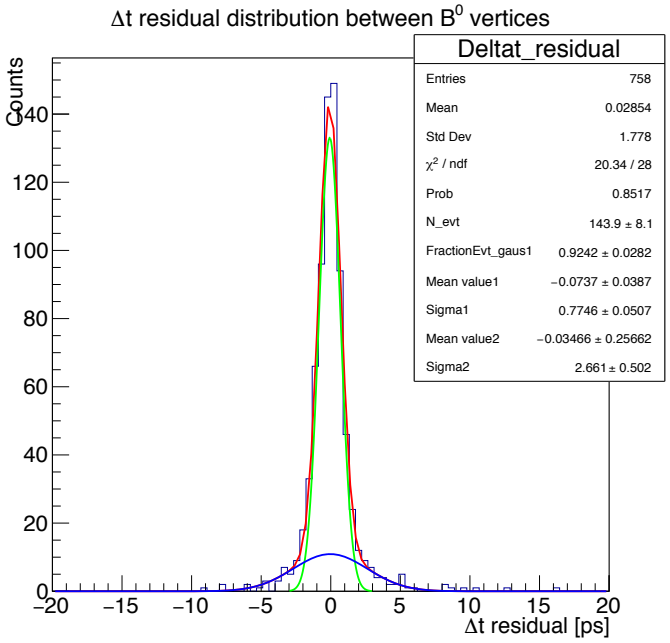

Figure 5.17: $B^0\Delta t$ residual distribution considering, at least, one hit in the SVD detector by both the pions from K^0_S.

The requirement just imposed reduces by a factor ~ 0.35 the statistic but the σ of the core Gaussian becomes $\sim$0.77 ps, while the σ of the tail Gaussian becomes $\sim$2.66 ps. Expressing the resolution as the weighted average of the two σ values we obtain a resolution of 0.93 ps.

5.5.2 Sensitivity estimate

In the final analysis, the S and C parameters will be extracted through an unbinned maximum likelihood fit to the Δt distribution, including the background. A preliminary sensitivity estimate on the parameters S and C is obtained with Toy Monte Carlo (MC) studies. In these studies, multiple experimental distributions with given values of S and C are generated according to the pdf's, once the numbers of signal and background events are assigned. The generated distributions are then fit and the parameters extracted. To do so, the RooFit framework [45] is used in order to perform unbinned maximum likelihood fits, generate Toy MC samples and produce plots, since it can model probability distributions in a compact way. It is able to extract the mean, the uncertainty values and the pull

distribution for each parameter included in the pdf function. The aim of the Toy MC studies is to perform a fit to the Δt pdf, from which the sensitivity on the parameters S and C must be extracted. In order to take into account the mis-tag probability the Δt pdf becomes ([7] pages 123-124):

$$P^{sig}_{\pm}(\Delta t) = (1 \mp \Delta\omega \pm \mu(2\omega))\frac{e^{-|\Delta t|/\tau_{B^0}}}{4\tau_{B^0}}\Big\{1 \pm S[\pm(1-2\omega) + \mu(1 \mp \Delta\omega)]\sin(\Delta m \Delta t) \mp C[\pm(1-2\omega) + \mu(1 \mp \Delta\omega)]\cos(\Delta m \Delta t)\Big\} \tag{5.5}$$

where the tagging parameters μ, ω and $\Delta\omega$ have been defined in section 5.3.3 (table 5.3). In addition, it has to be smeared by the resolution function R_{sig}, which is the sum of the two Gaussian functions obtained in the previous section (fig. 5.17 as reference). Furthermore, the background contribution must also be considered. For the moment, the machine background, introducing extra hits in the event, is not included. The background contribution consists in continuum ($e^+e^- \to u\overline{u}$, $d\overline{d}$, $s\overline{s}$ or $c\overline{c}$), charged (B^+B^-) and mixed ($B^0\overline{B}^0$) events that are erroneously reconstructed as signal. For the background from continuum, the pdf is assumed a delta function convoluted with the resolution function R_{bkg}. The latter can be fitted with a sum of two Gaussian functions, and the extracted weighted average σ is ~0.62 ps (fig. 5.18). To obtain this value, the official Belle II Monte Carlo sample ($\sim 10^7$ events) is used.

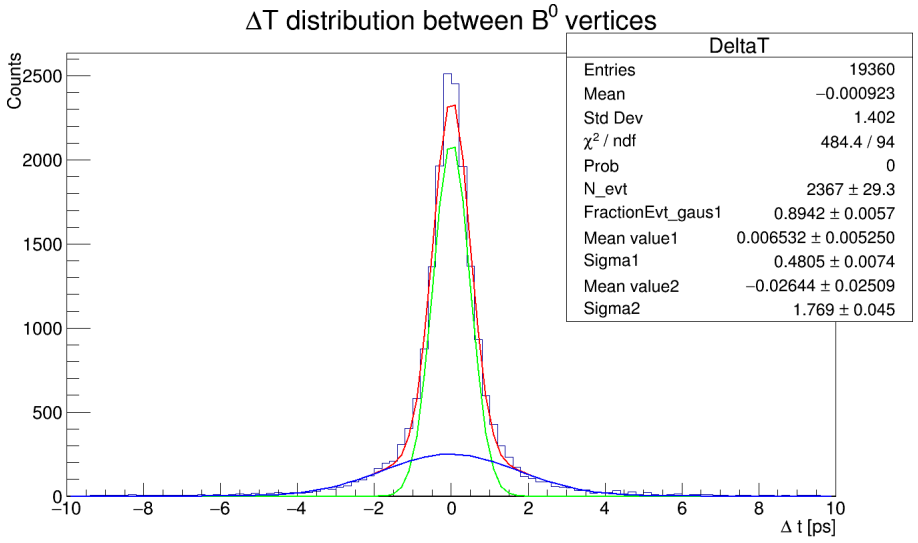

Figure 5.18: Δt distribution of $\sim 10^7$ background continuum events. The same cuts required to obtain the Δt signal distribution, are required.

For the background coming from $B\overline{B}$ events, the corresponding pdf functions should be further characterized through additional studies, that are not performed in this thesis. The number of $B\overline{B}$ background events that passes my cuts is low (∼100 over a total of $\sim 10^7$ events), preventing the possibility to perform a dedicated study. From previous BaBar and Belle measurements, we know that the dominant background contribution is from continuum (∼170 from $B\overline{B}$ and ∼6000 from continuum events). The final pdf that I generated is the sum of the continuum background resolution function (properly weighted) and the pdf reported in 5.5 smeared with the signal resolution function.

$$pdf(\Delta t) = f_{sig}(P_{\pm}^{sig} \otimes R_{sig}) + (1 - f_{sig})R_{bkg} \tag{5.6}$$

where R_{sig} and R_{bkg} are obtained previously, while f_{sig} is the fraction of signal events. Due to the fact that a complete event selection study is not yet implemented, I took the numbers of final signal events and f_{sig} from the previous analysis made by the BaBar experiment [43]. Considering only the direct decay of the $B^0 \longrightarrow K_S^0\pi^0\gamma$, they collected 133 signal events with $f_{sig} \simeq 0.02$. The BaBar experiment reached a final integrated luminosity of $\sim 0.46\ ab^{-1}$, that is ∼100 times less than the final expected statistic for Belle II. Thus, using the number of final signal events from BaBar, it is possible to make previsions of the sensitivity on S and C for the maximum integrated luminosity of Belle II ($\mathcal{L} = 50ab^{-1}$ that corresponds to ∼14000 signal events).

During the fit procedure, the parameters S and C are initialized at 0, in order to verify that the Toy MC can reproduce the same values used to generate the pdf, and thus validate the fit. I repeat the study for 3 different combinations of C and S, in order to check if the Toy MC machinery provides the same sensitivity; thus, the combinations C=0 and S=0, C=0 and S=0.1 (SM maximum prediction for S), C=-0.3 and S=-0.3 (large asymmetry) are reproduced. The corresponding mean, uncertainty and pull are reported in figures 5.19, 5.20 and 5.21. Here we can see that the mean values of the parameters coming from the fit are compatible with the generated ones and the pull distributions are fitted with a Gaussian function with standard deviation compatible with 1 (at 2σ level), meaning that the method is correctly verified by Toy MC. At the maximum integrated luminosity of 50 ab^{-1}, the uncertainty on S and C results around 0.026 and 0.021 respectively; for the S parameter, which is the most interesting one, the uncertainty is a factor ∼20 better than in BaBar. Part of this improvement is due to the larger statistic considered; in fact,

using a luminosity ∼100 times larger than in BaBar, the uncertainty on S and C should decrease as $\frac{1}{\sqrt{100}}$=0.1. With this sensitivity, the measurement in Belle II is expected to be no longer dominated by the statistical uncertainty as in BaBar and Belle. This statistical uncertainty allows to measure the expected SM value of 0.1 or, hopefully, NP deviations from it. It should be noted that the $B\overline{B}$ background pdf is not yet included and, since it has the same lifetime structure of the signal, could lead to a reduction in sensitivity.

The study reported in this chapter consists in the description of the time-dependent CP asymmetry analysis for the decay channel $B^0 \longrightarrow K^0_S\pi^0\gamma$. The final results of this study concern the resolution of the time difference between the two B^0 mesons, which is ∼0.93 ps; a preliminary estimate of the sensitivity on the violation parameter S, using the Toy MC method with the Belle II detector and using the final data sample (50 ab^{-1}), results a factor ∼20 better with respect to the previous BaBar result.

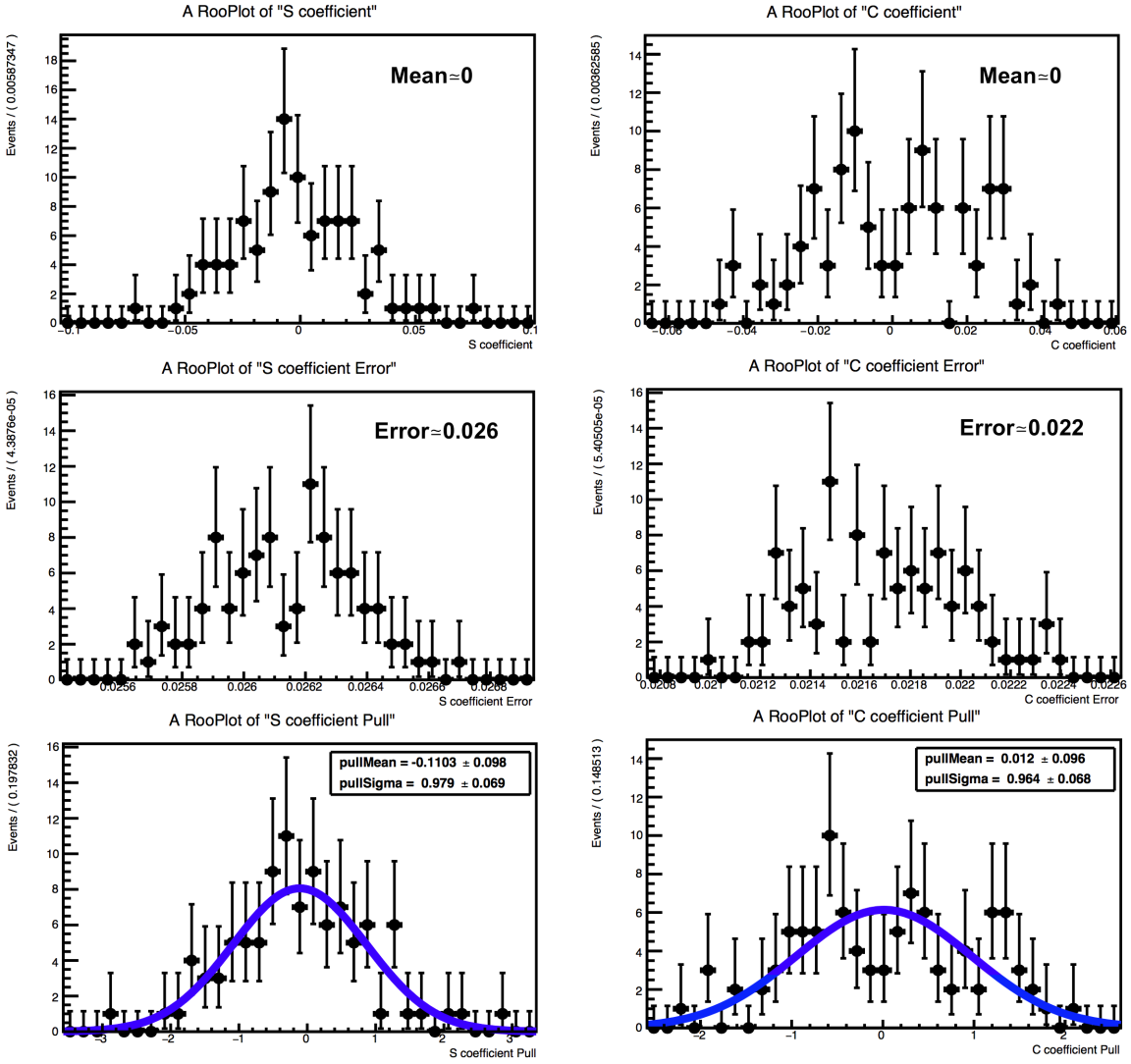

Figure 5.19: Mean (top), uncertainty (center) and pull (bottom) for the parameters C (left column) and S (right column). Here $\mathcal{L} = 50\ ab^{-1}$ and the parameters C and S are generated equal to 0.

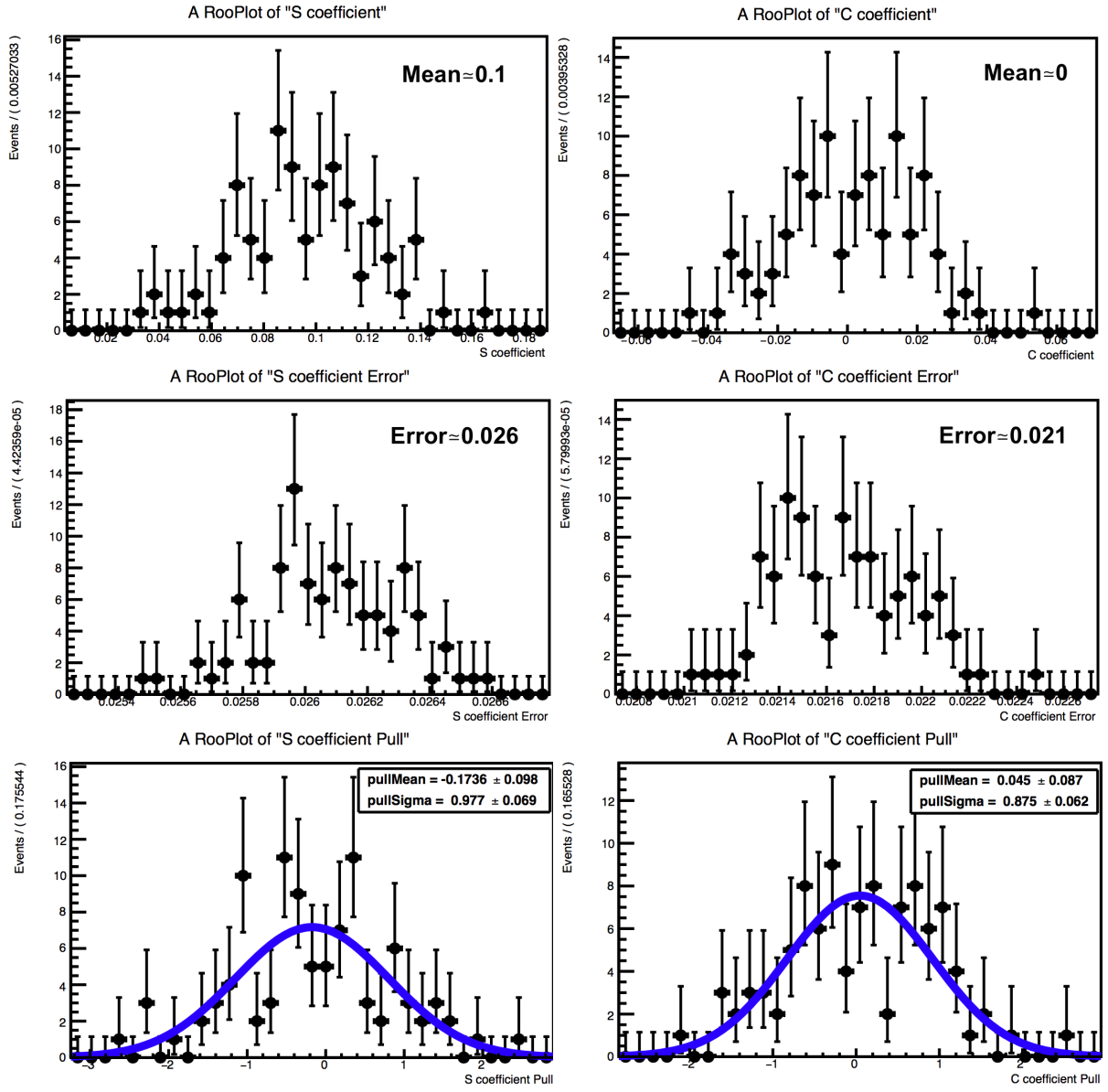

Figure 5.20: Mean (top), uncertainty (center) and pull (bottom) for the parameters C (left column) and S (right column). Here $\mathcal{L} = 50\ ab^{-1}$ and the parameters C and S are generated equal to 0 and 0.1 respectively.

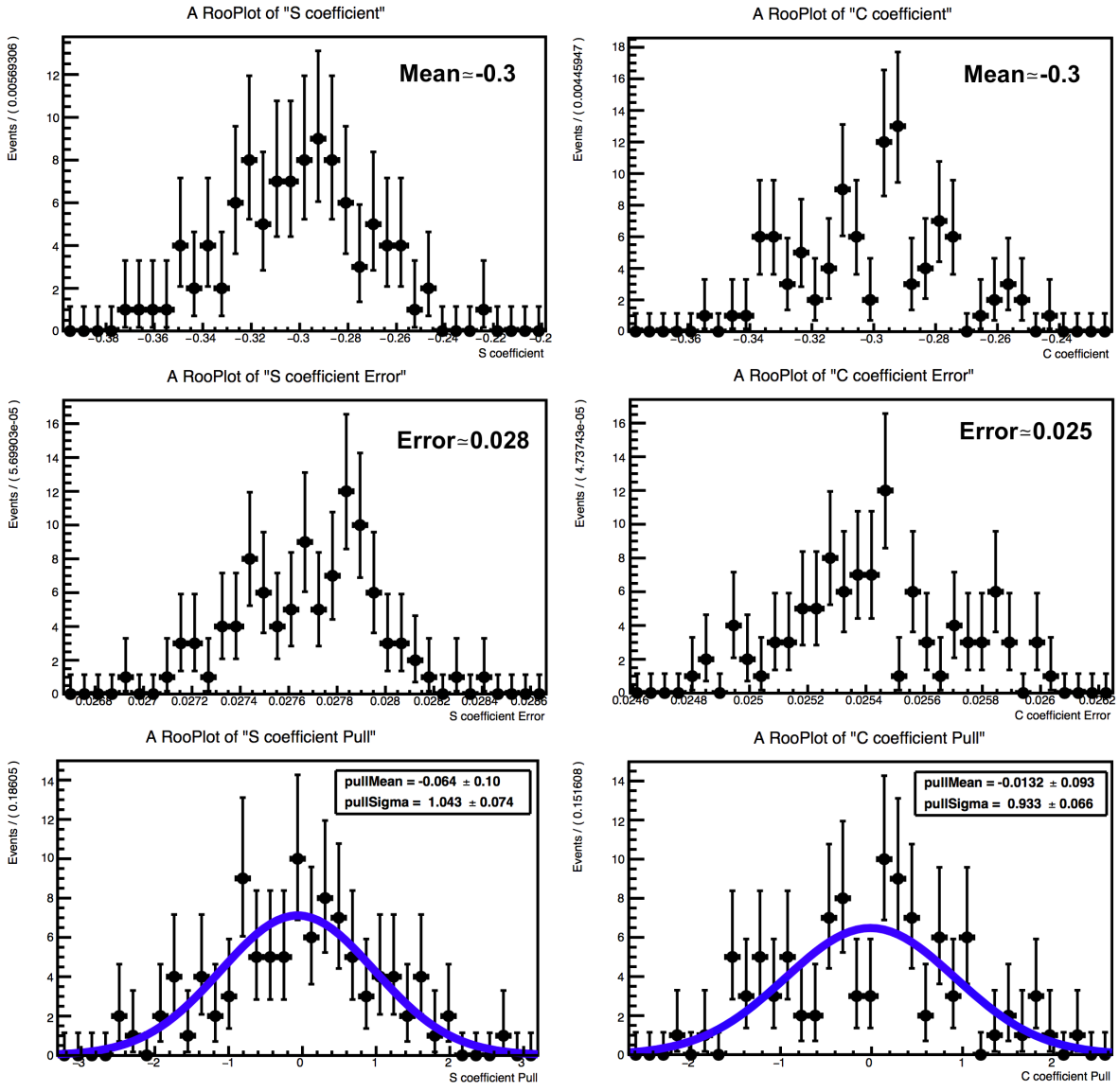

Figure 5.21: Mean (top), uncertainty (center) and pull (bottom) for the parameters C (left column) and S (right column). Here $\mathcal{L} = 50\ ab^{-1}$ and the parameters C and S are generated equal to -0.3.

Conclusions

In this thesis, a time dependent asymmetry study in the decay $B^0 \longrightarrow K^0_S\pi^0\gamma$ has been performed with the Belle II experiment. I provided an estimation of the resolution of the decay time difference (Δt) between the B^0 and the $\overline{B}^0$, through the reconstruction of the vertex positions of the neutral mesons. Taking advantage of the new improved vertex detector (VXD) and exploiting the new idea of the nano-beams scheme, I obtain a good vertex resolution of B^0_{sig} even if no charged tracks are emerging from the vertex position. Combining this information with the B^0_{tag} vertex position, the time difference Δt has been obtained through the formula: $\Delta z = \beta \cdot \gamma \cdot c \cdot \Delta t$. The Δt resolution is extracted from the residual distribution (requiring that the kaons are reconstructed by the SVD), which has been fitted with the sum of two Gaussian functions, one with $\sigma \simeq 0.77$ ps ($\sim$92% of events) while the other with $\sigma \simeq 2.66$ ps, corresponding to a final weighted resolution value of 0.93 ps. For this analysis the performance of the SVD and of the whole tracking systems is crucial.

Some studies based on Toy Monte Carlo technique have been performed in order to extract the statistical uncertainties on the parameters S and C by fitting the Δt distribution, and combining all the information coming from the flavour tagging, the signal Δt resolution and the continuum background Δt resolution. Due to the fact that a complete event selection study is not yet implemented, I took the number of final signal events and of the fraction of signal events from the latest analysis made by the BaBar experiment. The $B\overline{B}$ background source has not yet been considered as it requires additional studies and a larger monte carlo statistic. The uncertainties have been extrapolated to 50 ab^{-1} of integrated luminosity ($\sim$100 times $\mathcal{L}^{BaBar}_{int}$), for different generated values of C and S; from these studies, the statistical uncertainty on S and C results $\sim$0.025 and $\sim$0.021 respectively, which is a factor $\sim$20 better than the BaBar sensitivities.

As next step of this analysis, the machine background has to be included in the generated

sample and the background from $B\overline{B}$ events should be characterised and considered in the final pdf function. Furthermore, an optimized event selection has to be implemented; one can disentangle signal from background through applying selection criteria such as kinematic and event shape variables. Moreover, the estimation of the parameters S and C would be more precise if a multiple fit, of the event selection variables together with the Δt, is performed.

Another topic presented in this thesis concerns my work on the SVD hardware in the INFN-Pisa Laboratory of High Technology, consisting on the assembly of the backward and forward double-sided silicon strip detector modules. Following some unexpected behaviour observed during electrical tests, I performed computer simulations (using Sentaurus software) of a Belle II SVD detector in order to understand the effects of sensor defects, such as the breaking of the capacitive coupling layer between the read out strips and the substrate of the silicon sensor. The simulation is able to reproduce the electrical effects of the defect and have been extremely valuable to improve the quality and robustness of the constructed modules. The simulation structure implemented, can be helpful to understand other future electrical behaviour issues.

Bibliography

[1] Georges Aad et al. Observation of a new particle in the search for the Standard Model Higgs boson with the ATLAS detector at the LHC. *Phys. Lett.*, B716:1–29, 2012.

[2] Serguei Chatrchyan et al. Observation of a new boson at a mass of 125 GeV with the CMS experiment at the LHC. *Phys. Lett.*, B716:30–61, 2012.

[3] Makoto Kobayashi and Toshihide Maskawa. CP-Violation in the Renormalizable Theory of Weak Interaction. *Prog. Theor. Phys.*, 49(2):652–657, 1973.

[4] Keith A. Olive and al. Review of particle physics. *Chin. Phys. C*, 38(9):1–1676, 2014.

[5] Nicola Cabibbo. Unitary Symmetry and Leptonic Decays. *Phys. Rev. Lett.*, 10:531–533, 1963.

[6] Andrei D Sakharov. Violation of cp invariance, c asymmetry, and baryon asymmetry of the universe. *Soviet Physics Uspekhi*, 34(5):392, 1991.

[7] A. J. Bevan and al. The physics of the b factories. *The European Physical Journal C*, 74(11):3026, 2014.

[8] S. L. Glashow, J. Iliopoulos, and L. Maiani. Weak interactions with lepton-hadron symmetry. *Phys. Rev. D*, 2:1285–1292, Oct 1970.

[9] J. H. Christenson, J. W. Cronin, V. L. Fitch, and R. Turlay. Regeneration of k_1^0 mesons and the $k_1^0 - k_2^0$ mass difference. *Phys. Rev.*, 140, Oct 1965.

[10] Observation of direct cp violation in $k_{S,L} \to \pi\pi$ decays. *Phys. Rev. Lett.*, 83:22–27, Jul 1999.

[11] V. Fanti et al. A New measurement of direct CP violation in two pion decays of the neutral kaon. *Phys. Lett.*, B465:335–348, 1999.

[12] Y. Amhis et al. Averages of b-hadron, c-hadron, and τ-lepton properties as of summer 2016. 2016.

[13] Y. Chao et al. Improved measurements of partial rate asymmetry in B $\to$ h h decays. *Phys. Rev.*, D71:031502, 2005.

[14] Y. Amhis and al. Averages of b-hadron, c-hadron, and tau-lepton properties as of summer 2014. 2014. Online update at `http://www.slac.stanford.edu/xorg/hfag`.

[15] Jure Zupan. Penguin pollution estimates relevant for phi(2)/alpha extraction. *Nucl. Phys. Proc. Suppl.*, 170:33–38, 2007.

[16] J. Charles and al. CP Violation and the CKM Matrix: Assessing the Impact of the Asymmetric B Factories. *Eur. Phys. J. C*, 41:1–131, 2005. Updated results and plots available at: `http://ckmfitter.in2p3.fr`.

[17] M. Röhrken. Time-dependent cp violation measurements in neutral b meson to double-charm decays at the japanese belle experiment. 2012.

[18] Tobias Hurth and Farvah Mahmoudi. Colloquium: New physics search with flavor in the LHC era. *Rev. Mod. Phys.*, 85:795, 2013.

[19] David M. Straub. New physics correlations in rare decays. In *CKM unitarity triangle. Proceedings, 6th International Workshop, CKM 2010, Warwick, UK, September 6-10, 2010*, 2010.

[20] Thomas Becher, Alessandro Broggio, and Andrea Ferroglia. Introduction to Soft-Collinear Effective Theory. *Lect. Notes Phys.*, 896:pp.1–206, 2015.

[21] Peter L. Cho. Heavy hadron chiral perturbation theory. *Nucl. Phys.*, B396:183–204, 1993. [Erratum: Nucl. Phys.B421,683(1994)].

[22] Benjamin Grinstein and Dan Pirjol. The CP asymmetry in B0(t) $\longrightarrow$ K(S) pi0 gamma in the standard model. *Phys. Rev.*, D73:014013, 2006.

[23] Roel Aaij et al. Measurement of $\not{C}P$ asymmetries in the decays $B^0 \to K^{*0}\mu^+\mu^-$ and $B^+ \to K^+\mu^+\mu^-$. *JHEP*, 09:177, 2014.

[24] Pantaleo Raimondi. Status on SuperB effort. 2006. Talk given at the 2nd SuperB Workshop at Frascati (Italy), available at: `http://www.lnf.infn.it/conference/superb06/talks/raimondi1.ppt`.

[25] T. Abe and al. Belle ii Technical Design Report. *KEK Report 2010-1*, 2010.

[26] S. Chatrchyan et al. The CMS Experiment at the CERN LHC. *JINST*, 3:S08004, 2008.

[27] Thomas Luck et al. Performance studies of the belle ii silicon vertex detector with data taken at the desy test beam in april 2016. To be published in the proceedings of the 25^{th} International Workshop on Vertex Detectors, Proceedings Of Sience.

[28] Manfred Valentan. The silicon vertex detector for b-tagging at belle ii. September 2013. TPhd thesis.

[29] Hamamatsu Photonics (Giappone), `http://www.hamamatsu.com/us/en/index.html`.

[30] Micron Semiconductor (Gran Bretagna), `http://www.micronsemiconductor.co.uk`.

[31] Muller Kamins. Device electronics for integrated circuits. *Technology & Engineering*, 2002.

[32] M. J. French et al. Design and results from the APV25, a deep sub-micron CMOS front-end chip for the CMS tracker. *Nucl. Instrum. Meth.*, A466:359–365, 2001.

[33] C. Irmler et al. Construction and test of the first belle ii svd ladder implementing the origami chip-on-sensor design. *Journal of Instrumentation*, 11(01):C01087, 2016.

[34] Synopsys. Inc. sentaurus device user guide. September 2014.

[35] Helmuth Spieler. Semiconductor detector systems. *Oxford University Press*, 2005, 2nd printing 2006.

[36] Andreas Moll. The software framework of the belle ii experiment. *Journal of Physics: Conference Series*, 331(3):032024, 2011.

[37] David J. Lange. The evtgen particle decay simulation package. *Nucl. Instrum. Meth. A*, 462(1-2):152–155, 2001.

[38] Torbjorn Sjostrand, Stefan Ask, Jesper R. Christiansen, Richard Corke, Nishita Desai, Philip Ilten, Stephen Mrenna, Stefan Prestel, Christine O. Rasmussen, and Peter Z. Skands. An introduction to pythia 8.2. *Comput. Phys. Commun.*, 191:159–177, 2015.

[39] S. Agostinelli and al. Geant4: A simulation toolkit. *Nucl. Instrum. Meth. A*, 506(3):250–303, 2003.

[40] Rene Brun and Fons Rademakers. Root - an object oriented data analysis framework. *Nucl. Instrum. Meth. A*, 389:81–86, 1997. See also `http://root.cern.ch`.

[41] J. Tanaka. Kinematic fitting. *Belle Note # 194*.

[42] Wolfgang Waltenberger. Rave – a detector-independent toolkit to reconstruct vertices. *IEEE Transactions on Nuclear Science*, 58:434–444, 17 March 2011.

[43] Bernard Aubert et al. Measurement of Time-Dependent CP Asymmetry in $B^0 \to K^0_S\pi^0\gamma$ Decays. *Phys. Rev.*, D78:071102, 2008.

[44] Y. Ushiroda et al. Time-Dependent CP Asymmetries in $B^0 \to K^0_S\pi^0\gamma$ transitions. *Phys. Rev.*, D74:111104, 2006.

[45] D. Kirkby W. Verkerke. RooFit Users Manual. v2.91, 2008.